

Aeroelastic Tailoring of Strut-Braced Wings

MSc Thesis

J. Ran



Aeroelastic Tailoring of Strut-Braced Wings

MSc Thesis

by

Juliette Ran

to obtain the degree of Master of Science in Aerospace Engineering
at the Delft University of Technology,
to be defended publicly on Monday May 29, 2017 at 1:30 P.M.

Student number: 4086260
Thesis committee: Dr. ir. R. De Breuker, TU Delft, supervisor
Dr. S. R. Turteltaub, TU Delft
Dr. ir. M. Voskuyl, TU Delft
Dr. J. Sodja, TU Delft, supervisor

Front page cover art obtained at
https://www.nasa.gov/sites/default/files/boeing_sugar_original_full.jpg.

An electronic version of this thesis is available at <http://repository.tudelft.nl/>.



DELFT UNIVERSITY OF TECHNOLOGY
DEPARTMENT OF AEROSPACE STRUCTURES AND MATERIALS

The undersigned hereby certify that they have read and recommend to the Faculty of Aerospace Engineering
for acceptance a thesis entitled:

Aeroelastic tailoring of strut-braced wings

by
Juliette Ran

in partial fulfillment of the requirements for the degree of Master of Science

GRADUATION COMMITTEE

Committee chairman:

Dr. ir. R. De Breuker

Committee member:

Dr. ir. M. Voskuijl

Signature

Signature

Committee member:

Dr. S. R. Turteltaub

Committee member:

Dr. J. Sodja

Signature

Signature

Date

Acknowledgments

In 2010 I accepted the challenge of becoming an aerospace engineer. After almost seven years of studying I have finally arrived at the point of presenting my master thesis. Upon my first arrival at the Faculty of Aerospace Engineering I could never have guessed the extent of what I was about to learn. There were lots of lectures, group projects, homework assignments, presentations and exams that together taught me how to be an engineer. The experiences I had outside of the faculty were however at least as important to me. I got to meet lots of interesting people, make amazing friends and I got to share a ton of great times with them. Time flew by and I accepted all the challenges that came my way. The sum of these valuable experiences, both in university and outside, made me who I am today and I am very grateful for each and everyone of them.

This thesis contains the final chapter of my life as a student. Over the course of a full year I worked on an extremely interesting topic and I learned a lot. As much as I enjoyed working on the challenges that are inherent to the complexity of aeroelasticity and to doing research, it was not always easy and I could not have done it without the support from my daily supervisors. I want to thank Mario, Jurij and Roeland for their endless support, their motivating words and for the effort they put into guiding me up to this point.

In addition I would like to thank Dr. S.R. Turteltaub, MSc. and Dr. ir. M. Voskuyl for completing my graduation committee.

I also want to thank my parents and my brothers for their unconditional love and support, my roommates for encouraging me and helping me unwind when needed, and finally, I am sending out a big thanks to all my friends, for being there when I needed them.

Finishing my thesis work and my studies feels like the ending of an era. I can look back on a great period of my life, but at the same time I am looking forward to all that the future holds for me.

*J. Ran
Delft, May 2017*

Summary

Strut-braced wing aircraft are believed to have great potential for the future of large passenger air transport with regard to fuel burn reductions due to the combination of high structural and aerodynamic efficiency. Strut-braced wings deviate from conventional wings in the fact that they employ additional bracing at certain span location away from fuselage to relieve the bending moment at the root of the wing. The large aspect ratio wings that are thereby enabled, experience less induced drag, and reductions in wave drag and parasitic drag compared to conventional wings. The downside of a high degree of wing slenderness is the inherent wing flexibility which in turn makes strut-braced wings very prone to aeroelastic (flutter) instabilities.

In the last few years a lot of work has been done to get a better understanding of aeroelasticity of strut-braced wing and truss-braced wing aircraft in light of the Boeing Subsonic Ultra Green Aircraft Research (SUGAR) (Bradley et al., 2015). Nonetheless, flutter constraints still cause a significant weight penalty for these configurations. At the same time, passive load alleviation by the application of aeroelastic tailoring for the purpose resolving these flutter instabilities has not been exploited fully yet.

To investigate whether aeroelastic tailoring can indeed resolve aeroelastic instabilities in — and increase the potential of strut-braced wings, the existing Proteus framework was modified and verified to enable design of these configurations. Fourteen strut-braced wing models with varying strut configurations and a reference model of a clean wing, all with an aspect ratio of 19.4, have been optimized for a minimum weight objective and the corresponding results have been analyzed.

It was found that configuration parameters such as the axial stiffness of the strut, and the spanwise and chordwise location of the strut-wing connection had a significant influence on the aeroelastic vertical wing deflections and wing twist, respectively. Results of aeroelastic tailoring clearly showed that the spars were tailored for the inboard normal force caused by the strut. Stiffness results also implied that the wings were optimized for a wash-out effect at the root and a wash-in effect at the tip. As this result is essentially the exact opposite of what would be seen for conventional wing design, static aeroelastic deformations, active design constraints and critical aeroelastic eigenmodes of the strut-braced wings were further investigated.

The stiffness distribution throughout the wing had a smaller influence on the wing deformations than the configuration parameters, and mainly affected the rate of wing twist along the span of the wing. The wash-out effect at the root indeed resulted in an increase in wing twist over the first section of the wing, but the supposed wash-in effect only decreased this twist angle slightly, resulting in a small decrease in wash-out instead of actual wash-in.

Nevertheless, the wash-in effect could be explained by the flutter instabilities that were found to be the key design driver for tailoring of all strut-braced wing designs. Moreover, because of the extreme susceptibility of strut-braced wings to flutter, the bands of aeroelastic stability showed to be very narrow. As a consequence, laminate design was driven towards the boundaries posed by laminate feasibility constraints. The deformations corresponding to the most critical eigenmodes showed direct links to the tailored stiffness distribution.

The set of aeroelastically tailored strut-braced wing designs shows that the isolated wing mass decreases for increasing values of axial stiffness of the strut. At the same time the stiffest struts make a larger contribution to the total mass of the strut-braced wing. The configuration with the strut at 60% of the span, 30% of the chord length and with the second lowest axial stiffness was the most optimum design, resulting in a mass decrease of 20.9% with respect to the optimized clean wing.

From the presented results it can be concluded that aeroelastic tailoring is very well capable of avoiding flutter without the addition of any weight penalties. Aside from modifications aimed at increasing the accuracy of the current work, it is recommended that this research is continued on a full scale Boeing SUGAR strut-braced wing. In case aeroelastic tailoring on such a full scale model indeed resembles the promising results that were found here, the future of aviation will finally be associated with more disruptive developments and larger steps in fuel burn reductions alike.

J. Ran
Delft, May 2017

Contents

Acknowledgments	v
Summary	vii
Nomenclature	xi
1 Introduction	1
2 Literature Review	3
2.1 History of strut-braced wing research	3
2.2 Aeroelasticity of strut-braced wings	5
2.3 Aeroelastic tailoring of strut-braced wings	6
2.4 Synthesis	7
3 Thesis plan	9
3.1 Methodology	9
3.2 Assumptions and limitations	9
4 Modifications in Proteus for strut-braced wing analysis and design	11
4.1 Proteus framework	11
4.1.1 Structural model	12
4.1.2 Aerodynamic model	12
4.1.3 Aeroelastic coupling	13
4.1.4 Optimizer	13
4.2 Implementation strategy	13
4.3 Static solution	14
4.3.1 Addition of strut member	14
4.3.2 Degrees of freedom	15
4.3.3 Beam element orientation	16
4.3.4 Global stiffness formulation	16
4.3.5 Static aeroelastic solution	18
4.4 Dynamic solution	18
4.4.1 Structural dynamics	18
4.4.2 Dynamic aeroelastic coupling	18
4.5 Sensitivities and optimization	19
5 Verification	23
5.1 Verification model	23
5.2 Static solution	23
5.3 Dynamic solution	24
5.4 Aeroelastic loads	26
5.5 Flutter solution	26
5.6 Sensitivity calculation	27
6 Optimization settings	31
6.1 Test case objectives	31
6.2 Geometry and material	31
6.2.1 Material	31
6.2.2 Planform	32
6.2.3 Airfoil	32

6.3 Modelling parameters	33
6.3.1 Convergence study for number of structural elements	33
6.3.2 Convergence study for number of aerodynamic panels	33
6.3.3 Discretization of aerodynamic wake	35
6.3.4 Number of design regions	35
6.4 Design constraints	35
6.5 Load cases	36
6.6 Configuration parameter studies	38
6.6.1 Influence on aeroelastic behavior	38
6.6.2 Determination of design parameters	40
6.6.3 Design parameter synthesis	42
6.7 Initial guess	42
6.8 Advanced sensitivity studies	43
6.8.1 Static aeroelastic deflection	43
6.8.2 Lift distribution	44
6.8.3 Shear force distribution and root bending moment	45
6.8.4 Synthesis	47
7 Aeroelastic tailoring results	49
7.1 Clean wing reference optimization	49
7.1.1 Tailored clean wing design	49
7.1.2 Static aeroelastic deformation	51
7.1.3 Active design constraints	52
7.2 SBW optimization results	54
7.2.1 Thickness and directional stiffness results	54
7.2.2 Static aeroelastic deflection of tailored SBWs	59
7.2.3 Active design constraints	62
7.3 Tailored SBW mass	65
7.3.1 Convergence history	65
7.3.2 Optimized SBW mass	65
8 Conclusions and recommendations	67
8.1 Conclusion	67
8.2 Recommendations	68
Bibliography	69
A Summary of optimization settings	75
A.1 Fixed model parameters	75
A.2 Modelling parameters	75
A.3 Proteus inputs	76
A.4 Load case data	76
B Additional results of configuration parameter study	77
C Additional results of advanced sensitivity study	81
D Aeroelastic tailoring results	83
E Static aeroelastic deflections of tailored SBWs	87
E.1 Wing deformation comparisons	87
E.2 Deflection and wing twist plots per configuration subset	87
F Isolated aeroelastic deflection and wing twist plots	93
F.1 Subset A: Fixed y_{strut} and $x_{strut} = 30\%c$, and varying EA_{strut}	93
F.2 Subset B: Fixed EA_{strut} and y_{strut} , with varying x_{strut}	94
G Most critical aeroelastic eigenmodes	99

Nomenclature

Abbreviations

AR	Aspect ratio
DOF	Degree of freedom
EAS	Equivalent airspeed
FE	Finite element
GCMMA	Globally convergent method of moving asymptotes
HALE	High-altitude long-endurance
LCO	Limit cycle oscillation
MDO	Multidisciplinary design optimization
MTOW	Maximum take-off weight
NLF	Natural laminar flow
QI	Quasi-isotropic
SBW	Strut-braced wing
SUGAR	Subsonic Ultra Green Aircraft Research
TAS	True airspeed
TBW	Truss-braced wing
VLM	Vortex-lattice method

Greek symbols

α	Angle of attack
δ_i	Displacement along i-axis
ϵ	Strain
Γ	Dihedral angle
γ	Shear strain
Λ	Sweep angle
λ	Taper ratio
ν	Poisson ratio
ρ	Density
ρ_0	Air density at sea level
θ_i	Rotation about i-axis
ξ	Lamination parameter

Latin symbols

A	Area
a	Speed of sound
a_{ij}	Component of inverted in-plane stiffness matrix
b	Half wing span
c	Chord length
E	Elastic modulus
EA_{strut}	Strut axial stiffness term
f	Frequency
G	Shear modulus
g	Gravitational acceleration
h	Altitude
I	Area moment of inertia
J	Torsional rigidity
L	Lift
M	Mach number
m	mass
S	Wing area
t	Thickness
V	Velocity
V_f	Flutter speed
V_{div}	Divergence speed
W	Weight
x_{strut}	Chordwise location of strut-wing connection
y_{strut}	Spanwise location of strut-wing connection
z_{strut}	Vertical location of strut-fuselage connection

Vectors and matrices

\mathbf{A}	In-plane stiffness matrix
\mathbf{B}	Local-global transformation matrix
\mathbf{D}	Out-of-plane stiffness matrix
\mathbf{e}_i^0	Unit vector defining direction of local element frame axis
\mathbf{F}_a	Aerodynamic load vector
\mathbf{f}_l	Internal force vector
\mathbf{F}_{ext}	External force vector

\mathbf{F}_{strut}	Force induced by strut
\mathbf{K}^g	Global stiffness matrix
\mathbf{k}_l	Local stiffness matrix
\mathbf{M}	Mass matrix
\mathbf{p}	Vector of structural degrees of freedom
\mathbf{q}^0	Auxiliary vector for definition of local element frame
\mathbf{x}	Design variable vector

Introduction

Large aspect ratio wing aircraft got an increased amount of research attention in the last decades, as their aerodynamic efficiency has great potential for reducing fossil fuel burn and emissions. With diminishing supply of natural resources and the serious share of commercial aviation to global CO_2 production, these reductions are urgent topics in aviation. Although aerodynamic efficiency increases with aspect ratio because of the inherent reduction in induced drag, structural efficiency decreases rapidly as wings become longer and more slim. As a result wing weight increases, which in turn requires increased fuel burns.

It was thought that a summit was reached with respect to the combined structural and aerodynamic efficiency of high aspect ratio aircraft, but a surprisingly old concept found its way back into current aviation research: the strut-braced wing (SBW). SBW aircraft deviate from conventional tube-wing configurations in the sense that they exploit additional bracing at a certain span location away from fuselage to relieve the bending moment at the root of the wing. To accommodate the additional bracing structure, SBW aircraft typically display a high wing configuration. Figure 1.1 shows an example of a truss-braced wing (TBW) configuration, where the bracing consists of multiple members, being a strut and a jury.

The strut or truss structure enables larger aspect ratios for the same wing span. This does not only mean that the wings will experience less induced drag during flight, but the more slender wings also employ smaller thickness-to-chord ratios. A decrease in wing thickness induces a reduction in wave drag, while a smaller chord determines a smaller Reynolds number, reducing parasitic drag and allowing for natural laminar flow (NLF) (Cavallaro and Demasi, 2016).

The increased load bearing potential of SBW and TBW configurations and the multiple load paths from the strut or truss structure allow the inboard wing box to be lighter and thinner, and thus more flexible. The downside is that the combination of a complex load path and a flexible inboard wing can have significant impact on the aeroelastic behavior of the vehicle, such as causing excessive gust loading, unacceptable flutter margins, and destabilizing aero-servo-elastic coupling.

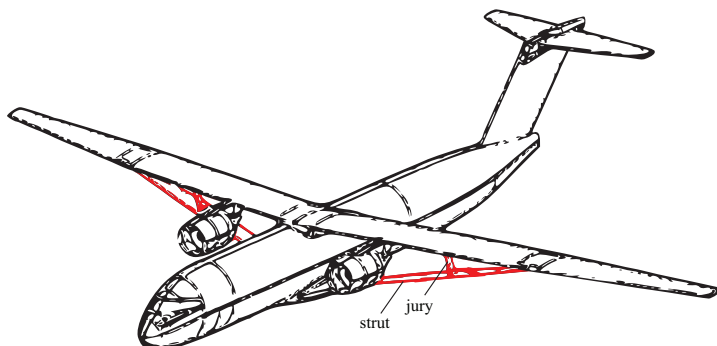


Figure 1.1: Representation of typical truss-braced wing

Recently, a lot of work has been done to get a better understanding of aeroelasticity of SBW and TBW aircraft in light of the Boeing Subsonic Ultra Green Aircraft Research (SUGAR) (Bradley et al., 2015). Although a lot of knowledge was gained on the aeroelastic behavior of these configurations, the weight penalties caused by flutter constraints and active load alleviation systems that were investigated for avoiding aeroelastic instabilities in SBW aircraft are still critical. It was found that the aeroelastic behavior of SBW has not yet been employed to the fullest, as could be done by applying aeroelastic tailoring techniques. Aeroelastic tailoring is "*the embodiment of directional stiffness into an aircraft structural design to control aeroelastic deformation, static or dynamic, in such a fashion as to affect the aerodynamic and structural performance of that aircraft in a beneficial way.*" (Shirk et al., 1986). The increased use of composite materials in modern aircraft structures allows for application of this technique and for exploring the full potential of anisotropy of composite materials. Consequently, aeroelastic tailoring has become an important topic in aircraft structural design research and within TU Delft this resulted in the development of an in-house aeroelastic analysis and design framework by De Breuker (2011).

It is believed that the application of the aeroelastic tailoring principle in SBW design reduces the required flutter weight penalties and the need for active load alleviation systems, eventually resulting in higher fuel burn reductions. Existing research efforts either investigated passive load alleviation induced by the relative orientation of the wing and strut (Gern et al., 2000a; Gur et al., 2010), or aeroelastic tailoring of TBWs with a limited amount of design variables (Wang et al., 2015). The aim of this master thesis will therefore be to combine these two principles in the scheme of the following research objective:

The research objective is to design an aeroelastically tailored strut-braced wing model based on the state-of-the-art Boeing SUGAR TBW planform, by adjusting the existing TU Delft aeroelastic tailoring framework Proteus for strut-braced wings, investigating the effect of different strut configurations on aeroelastic tailoring, and finally assess the aeroelastic behavior of the most optimal design.

This thesis report is structured as follows. In chapter 2 the existing literature on the topics of SBW aircraft, aeroelastic analysis and aeroelastic tailoring is reviewed. Chapter 3 sets out a plan for achieving the research objective. Chapter 4 discusses the modifications applied to include SBW configurations in Proteus, which are then verified in chapter 5. Design of the optimization settings is explained in chapter 6 and the results of the optimizations performed on with these settings are analyzed in chapter 7. Finally, chapter 8 concludes this thesis and provides recommendations for future work on this topic.

2

Literature Review

The present work is intended to be an addition to the body of knowledge that currently exists on the topic of aeroelastic tailoring of SBWs. Recently, many research efforts have been conducted on aeroelastic research of SBWs. This chapter discusses these efforts to provide the required background information and to draw up a scientific framework for current thesis research.

2.1. History of strut-braced wing research

The SBW is a relatively old concept that originates from the very beginning of aviation history, and is mainly known from small general aviation aircraft. Aiming for high aspect ratios Hurel (1952) employed SBW on the Hurel-Dubois HD-31 already in 1953, as shown in figure 2.1. Nonetheless, because of implicit drag penalties caused by the strut structure it was found that cantilever wings were aerodynamically more efficient, and the SBW concept disappeared to the background. It was Werner Pfenninger from Northrop who kept the SBW concept alive by publishing numerous studies until the late 1980s advocating for exploiting laminar flow (Pfenninger, 1977) and for reductions of induced drag with high-aspect ratio wings (Pfenninger and Vemuru, 1988).



Figure 2.1: Photograph of HD-31 (Visschedijk, 2008)

Over the years multiple parties picked up the idea to further investigate SBW aircraft configurations to achieve structurally efficient high-aspect-ratio wings for reducing induced drag resulting in fuel burn reduction, weight savings (Kulfan and Vachal, 1978; Turriziani et al., 1980), and cruise range improvements (Smith et al., 1981).

Despite the fact that these studies all showed the potential of SBW aircraft configurations, the work was not expanded until 1996 when the National Aeronautics and Space Administration (NASA) challenged the Virginia Polytechnic Institute and State University (hereinafter referred to as Virginia Tech) to further explore

the possibilities of SBW and TBW concepts for transonic transport aircraft (Grasmeyer, 1998). It was clear that strong coupling between aerodynamics and structures due to high flexibility of the slender wings and the influence of intermediate span supports increased the complexity of SBW and TBW design and required an interdisciplinary approach for design optimization (Gern et al., 2001).

To this end the Multidisciplinary Analysis and Design Center at Virginia Tech, the University of Florida and Lockheed Martin Aeronautical Systems carried out various multidisciplinary design optimization (MDO) studies on SBW aircraft, from which the results all proved the SBW aircraft to be a feasible concept for future aviation and more specifically, typical long-range missions (Gern et al., 2005).

Although it was recognized that aeroelastic effects should be considered in early structural design stages (Gern et al., 1999, 2001; Naghshineh-pour, 1998), these studies only considered static aeroelasticity. Sulaeman et al. (2002) were the first ones to consider dynamic aeroelasticity for SBW aircraft design. They performed parametric studies on the position of the strut-wing junction for load alleviation and investigated the geometric stiffness effect from the presence of a compressive axial force in the inner wing due to the tensile strut force for positive g maneuvers (Sulaeman et al., 2002). It was shown that a linear elastically formulated compressive force decreases the inner wing buckling capacity and flutter speed significantly when the wing-strut junction is placed near the wing tip, and that it has no significant influence when the junction is near to the root (Sulaeman et al., 2003).

Their parametric studies also showed that the flutter speed decreases for outboard wing-strut junctions ($y_{strut} > 80\%$ of semi-span), for aft movement of the wing-strut junction with respect to the front spar, and for longer offset beams connecting wing and strut. Multiple parametric studies on SBW configurations concluded that a twist moment generated by placing the strut-wing connection at the front spar leads to increased structural weight savings, and that there is large potential for passive load alleviation in these configurations (Gern et al., 2000b).

Bhatia et al. (2009) established that the higher achievable wing span reduces the natural frequencies of the wing structure and thus has a significant impact on its dynamic behavior. They also concluded that these natural frequencies come very close to the rigid-body flight dynamics modes, such that coupling between the two might occur. The geometric stiffness effect investigated by Sulaeman et al. (2002) would lower the structural natural frequencies even further, increasing the risk for this coupling (Bhatia et al., 2009).

In (Bhatia et al., 2010, 2012; Meadows et al., 2012) advances towards the incorporation of flutter constraints into their MDO framework were made by applying linear approximations to calculate flutter boundaries. Aeroelastic coupling was however neglected. Bhatia et al. (2012) identified that a spanwise strut location of $0.55b < y_{strut} < 0.70b$ yields the highest flutter speeds. Furthermore, it was shown that the best flutter performance for SBWs is achieved if wing and strut have the same sweep angle. Mallik et al. (2013) concluded that flutter constraints result in a significant weight penalty for TBW configurations as compared to the cantilever concepts. A more accurate aeroelastic analysis still showed that flutter constraints result in a significant weight penalty for TBW configurations, but only compared to TBW configurations for which no flutter constraints were included (Mallik et al., 2015). They concluded that the designs would become feasible when active or passive flutter-suppression mechanisms were to be applied (Mallik et al., 2013, 2015). With that they confirmed the need for passive or active load alleviation systems that was also identified by (Meadows et al., 2012).

Alongside the Virginia Tech SBW investigations, Boeing started focusing on the SBW/TBW configuration for B737-sized transport as the winning concept of their SUGAR project funded by NASA (Bradley and Droney, 2011). An MDO study from Virginia Tech and Georgia Institute of Technology (Georgia Tech) identified the one-jury TBW configuration with a wingspan of 52 m and NLF on the upper wing surface as the optimal configuration for the objective mission in terms of fuel burn (Nam et al., 2014; Chakraborty et al., 2015). This advantage of TBW over SBW configurations confirmed the results of earlier Virginia Tech studies (Bhatia et al., 2009; Gur et al., 2010; Seber et al., 2011). Adding a second jury member only resulted in marginal improvements, so it was decided to stick to the simple one-jury TBW configuration (Nam et al., 2014; Chakraborty et al., 2015).

Aside from clamped joints, also pin and ball joints were considered for the strut connections. Because of fabrication and assembly reasons it was finally decided that all subsequent MDO analyses would be done



Figure 2.2: Boeing SUGAR TBW design (Scott et al., 2015)

Table 2.1: Characteristic data SUGAR TBW (Bradley et al., 2015)

Property	Magnitude
MTOW [kg]	68039
S [m^2]	137.23
AR [-]	19.55
λ [-]	0.35
$\Lambda_{25\%c}$ [$^\circ$]	12.52
Γ [$^\circ$]	-1.5
t/c [-]	0.080/0.106/0.095
x_{strut} [%c]	14.29
y_{strut} [%b]	57.6
z_{strut} [m]	-3.96

with ball-jointed boundary conditions for the strut and clamped boundary conditions for the jury member. The resulting one-jury TBW configuration shown in figure 2.2 was set as the basis for sequential work in the interest of SUGAR TBW research (Nam et al., 2014; Chakraborty et al., 2015) and as starting point for this thesis work. The characteristics of the SUGAR TBW design are listed in Table 2.1. It is important to note that this configuration resulted from an MDO process that did not include any flutter analysis. Also, the influence of dynamic gusts was only included by a linear scaling factor (Chakraborty et al., 2015).

2.2. Aeroelasticity of strut-braced wings

Because of high flexibility, reduced torsional stiffness of slender wings and the change in lift distribution caused by the strut or truss, aeroelasticity plays a major role in SBW aircraft design. Previous flutter studies that were included in MDO frameworks for TBW aircraft design, were based on linear approximations and were neglecting aeroelastic coupling. The importance of inclusion of geometric structural nonlinearities in aeroelastic analysis for unconventional airplane configurations such as joined-wing aircraft (Livne, 2001; Livne and Weisshaar, 2003), and high-altitude long-endurance (HALE) aircraft (Patil et al., 2000, 2001; Patil and Hodges, 2004) has been investigated extensively. To account for the geometric nonlinearity caused by potential large deformations expected for high aspect ratio wings and because of their structurally constrained nature, it was understood that SBW and TBW configurations also require geometric nonlinearities in the aeroelastic analyses (Chen and Sulaeman, 2003; Demasi and Livne, 2009).

A nonlinear aeroelastic analysis of the SUGAR single-jury TBW aircraft was done by Coggin et al. (2014) with a nonlinear elastic large displacement formulation for computation of the structural pre-stress (that is, the presence of in-plane load on the inner wing). The analysis showed that indeed the calculated flutter speed

increases for increasing angles of attack, and is very sensitive to changes in ballast mass. For validation of the aeroelastic analysis of the SUGAR TBW aircraft, aeroelastic wind tunnel tests were conducted (Allen et al., 2015; Bradley et al., 2014). A closed-loop flutter suppression mechanism was found to be successful, and also successfully alleviated some gust load (Scott et al., 2015).

Based on wind tunnel test results the analysis framework was updated and the high sensitivity of the limit cycle oscillation (LCO) or flutter onset to the mass distribution of the wing (Bartels et al., 2015; Zhao et al., 2015; Coggin et al., 2014) was confirmed. The dependence of LCO amplitude and frequency on angle of attack and the sensitivity of flutter speed to the angle of attack were also confirmed (Zhao et al., 2015; Bartels et al., 2015).

Investigation of the physical mechanisms behind the flutter behavior showed that inclusion of pre-stress in the nonlinear analysis changes both natural frequencies and mode shapes, and thus increases the flutter boundary. The third mode was found to be critical, followed by the fourth mode in a lesser extent (Zhao et al., 2015), confirming the results of (Coggin et al., 2014; Bartels et al., 2015).

To satisfy the high multidisciplinary nature of SBW and TBW aircraft performance, efforts are made to include the discussed state-of-the-art aeroelastic analysis into MDO frameworks. However, due to the inherent computational costs, very sophisticated nonlinear pre-stressed flutter analyses cannot be incorporated in MDO frameworks (Mallik et al., 2015).

Concluding the recent boost of research into aeroelasticity of SBW and TBW aircraft, it can be said that flutter behavior of SBWs in subsonic conditions is well understood and simulated by now. The in-plane loads in strut and inner wing and geometric nonlinearities associated with large deflections of flexible wings make nonlinear aeroelastic analysis necessary for SBW aircraft. The second bending mode (mode 3) and the first torsion mode (mode 4) were found to be the critical modes for the SUGAR wind tunnel model. Gust response behavior of TBWs has been investigated to a small extent only, and with a scope that was limited to active control loops.

2.3. Aeroelastic tailoring of strut-braced wings

In order to achieve light weight high-aspect ratio wing aircraft designs, and in particular TBW aircraft design, the inherent aeroelastic instability challenges need to be overcome. Luckily, "*aeroelasticity has progressed from a problem area to become one of the first areas to use integrated technologies to turn problems into opportunities and harness aeroelastic interactions to improve airplane performance*" (Livne and Weisshaar, 2003).

Mallik et al. (2015) stated that for true feasibility of TBW aircraft active or passive flutter suppression mechanisms need to be employed (Mallik et al., 2015). Passive load alleviation techniques for SBW or TBW configurations were already investigated by structural tailoring of the location of the strut-wing connection (in both chord-wise and span-wise direction) and the location of the strut-fuselage connection, as was mentioned in section 2.1.

A traditional method for obtaining flutter onset delay is ballast mass placement, but the high sensitivity of the flutter speed for TBWs (Coggin et al., 2014; Zhao et al., 2015) adding mass may be undesirable. A more sophisticated method of passive load alleviation is to use the anisotropic stiffness and strength properties of fiber composite laminates to obtain favorable structural coupling and with this tailor TBW aircraft structural design for optimal aeroelastic behavior. The last decades the science of aeroelastic tailoring has been subjected to a research boost as composites are increasingly considered as material for aircraft structures. By employing this principle, aeroelastic tailoring can result in aircraft weight reduction, but can also improve aeroelastic characteristics, like gust load alleviation and increase of the flutter speed (Hertz et al., 1981; Eastep et al., 1999). Within TU Delft aeroelastic tailoring of composite wing aircraft has been addressed in research efforts that lead to the aeroelastic tailoring framework Proteus that was developed by De Breuker (2011), and has been further expanded and improved over the years (Werter, 2012; Werter and De Breuker, 2015).

Weisshaar and Lee (2002); Blair, Canfield, and Roberts (2005) performed aeroelastic tailoring of joined-wings, which have the same constrained nature as TBW configurations. Later, Cavallaro et al. (2014) investigated the effect of anisotropic materials on the nonlinear response and snap-buckling instability of these configurations.

Within the framework of the Onera ALBRATROS SBW project, Carrier et al. (2012) were the first who considered composite material in their parametric studies for SBW configurations, but only did a linear aeroelastic analysis at the end of the design process as oppose to full aeroelastic tailoring. DLR (Chiozzotto, 2015)

presented a preliminary wing weight estimation of a composite SBW aircraft. Different composite layups were analyzed and aeroelastic effects were accounted for in the sizing, but a flutter analysis and also the axial loads on the inner wing were left out.

As the analysis level of these examples indicates, aeroelastic tailoring of composite SBW configurations is still in its infancy. The only actual attempt of aeroelastic tailoring of a composite TBW configuration that has been published so far, has been done by Wang et al. (2015). The design variables they took into account for weight optimization were limited to thickness of each composite layer and the thickness of the aluminum spars and ribs (Wang et al., 2015). As opposed to the typical aeroelastic tailoring procedure in the TU Delft Proteus framework, lamination parameters or stiffness directions were not taken into account as variables.

2.4. Synthesis

From the literature discussed in sections 2.1 to 2.3 an important gap in the current state of aeroelastic research on SBW aircraft appeared. State-of-the-art SBW and TBW configurations are a product of MDO processes that did not all include a flutter analysis and only a linear scaling factor to include the influence of dynamic gust within the quasi-steady load definition (Chakraborty et al., 2015). The high flexibility of SBWs makes these configurations however very prone to critical aeroelastic behavior, resulting in unacceptable flutter margins or excessive gust loading. Mallik et al. (2015) showed that to decrease or avoid the required flutter weight penalty for SBW configurations and thus to show their actual efficiency potential, a passive or active flutter suppression method should be implemented. Active aeroelastic load alleviation system research has been part of the Boeing SUGAR project and was investigated on a preliminary level (Scott et al., 2015). Although passive load alleviation for SBW configurations certainly has potential as well, only few elementary investigations on this topic have been done so far, as was discussed in section 2.3.

It is therefore intended that this MSc thesis research will expand the current knowledge on aeroelastic tailoring of SBW configurations and on their aeroelastic behavior. As was clear from the reviewed literature, the different parameters that define a SBW configuration have a significant influence on its aeroelastic behavior. Therefore, examination of the influence of these parameters on aeroelastic tailoring results will be part of this research as well.

3

Thesis plan

In this chapter the plan for conducting this thesis work will be set out. The plan contains the activities that will facilitate the completion of the thesis objective as stated in chapter 1. The assumptions that are involved with the project plan and any consequential limitations on the results are discussed as well.

3.1. Methodology

Chapter 2 identified that the high flexibility of SBW aircraft calls for aeroelastic load alleviation, and that SBW configurations certainly hold potential for exploiting both active and passive alleviation systems. In reality, most of the MDO processes that lead to current state-of-the-art TBW aircraft designs did not even include a dedicated flutter or dynamic gust analysis. Furthermore, only active load alleviation systems were investigated. It is expected that aeroelastic tailoring can reduce the need for active load alleviation techniques and flutter weight penalties, and in turn reduce structural wing weight and further increase the potential of SBW aircraft over conventional aircraft designs, regarding fuel efficiency.

The main research question that is distilled from these observations and that will be answered in this thesis work is defined as: *To what extent can a SBW design based on the Boeing SUGAR planform be optimized by aeroelastic tailoring, and what is the influence of the optimization on the aeroelastic behavior of the SBW design?* To the end of answering the research question and achieving the objective, the existing TU Delft aeroelastic tailoring framework Proteus will be modified to enable analysis and optimization of SBW configurations. Subsequently, a verification case is carried out to check whether the modified framework produces structurally and aeroelastically correct results.

After Proteus including the SBW option is verified, it will be used to design the experiments for investigation of the extent to which SBW designs can be optimized by aeroelastic tailoring. As configuration parameters such as the location of the strut-wing junction have a significant influence on the aeroelastic behavior of the SBW, these will also be taken into account.

Figure 3.1 schematically presents the approach that will be followed to achieve the research objective. The boundary conditions that are applied for implementation of the strut member are based on the Boeing SUGAR concept (Bradley et al., 2015). Verification is done by comparing the structural and aeroelastic responses of a SBW configuration based on the Goland wing in Proteus with those computed in MSC Nastran. With the verified framework an analysis will be done on different parameters that define the relative orientation of wing and strut, for their influence on the aeroelastic behavior of the wing. Based on this parameter study and the constraints that are posed by manufacturing and testing facilities that are intended to be used in future research efforts, the numerical optimization experiments will be defined. Finally, the optimally tailored SBW will be subjected to an aeroelastic analysis in order to conclude on the achieved optimization and the corresponding aeroelastic behavior.

3.2. Assumptions and limitations

For implementation of the strut in Proteus a number of assumptions is made based on knowledge from literature on SBW aircraft. In light of the Boeing SUGAR Virginia Tech studies, Chakraborty et al. (2015) investigated the benefits of either having fixed, hinged or ball joints at the end of the truss members. Considerations on

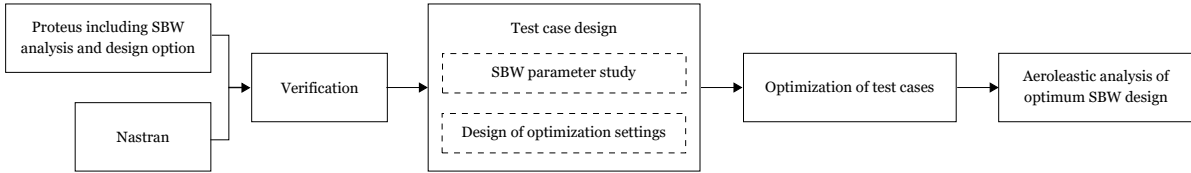


Figure 3.1: Thesis work breakdown structure

ease of manufacturing, assembly and maintenance of the structure lead to the use of ball-joints for all following TBW research. Since manufacturing and assembly will be of high importance in case of future physical experiments, it was decided to also apply hinge and ball-type joints in this research. To save weight in the strut-wing connection assembly, this joint will be a simple hinge joint, leaving the strut free to rotate only around the x-axis at this end. The fuselage-strut connection is not weight critical, and will be free to rotate around all three axes. This assumption will affect the calculation of the buckling properties of the strut by making it more conservative. Out of similar considerations for ease of future assembly it was decided to limit current thesis work to a single strut support structure, and thus focus on a SBW configuration instead of a TBW.

Additionally, Proteus itself is also build on assumptions and limitations. The aerodynamic solution in the Proteus framework and based on potential flow theory using a vortex lattice method (VLM), assuming a thin wing and inviscid and irrotational flow (Werter and De Breuker, 2015). The Prandtl-Glauert correction is employed to account for compressibility effects at higher Mach numbers. Since this correction is known to only be applicable for Mach numbers up to 0.7, the analysis of SBWs with Proteus is limited to subsonic velocities.

Since the simplicity of the VLM model that is currently generating the aerodynamic forces in Proteus cannot capture the aerodynamic interference at the junction of the strut and wing, the strut is assumed to not generate any lift. Modifications to the aerodynamic model are outside the scope of this thesis work. Since the reference Boeing SUGAR project was based on non-lifting struts as well, this assumption is however legitimate (White, 2015). As the strut is assumed to not generate any lift, any drag induced by the strut is assumed to be equal to zero as well. Since earlier publications on high-aspect ratio wings have shown that drag has a negligible effect on dynamic aeroelasticity compared to the predominant effect of lift (Patil et al., 1999), assuming zero strut drag is a valid assumption for the purpose of investigating the aeroelastic behavior of SBWs with respect to weight objectives. It needs to be noted that in case of optimizations with maximum range objectives the strut drag cannot be neglected.

One final limit that is put on this research, concerns the optimization of the strut itself. Because the main objective of this thesis is to investigate the effect of certain strut configurations on aeroelastic tailoring results in the wing, tailoring of the strut itself will be limited by setting tight boundaries on its thickness and by using an isotropic strut material. In this way the mechanical properties of the strut can be controlled, while the effect of the strut on the aeroelastic behavior of the wing and the aeroelastic tailoring results is still fully taken into account, as will be explained in chapter 4.

4

Modifications in Proteus for strut-braced wing analysis and design

Before any analysis or optimization can be done on SBWs, the Proteus framework needs to be modified for these wing configurations. This chapter discusses the modifications that are required for implementation of the SBW in Proteus.

4.1. Proteus framework

Proteus is a preliminary aeroelastic design tool for composite aircraft wings that has been developed in-house at TU Delft by Werter and De Breuker (2015). For a given aircraft wing static and dynamic aeroelastic analyses can be carried out and optimization of the composite laminate thickness and orientation with respect to directional stiffness can be performed. Werter and De Breuker (2015) give a complete explanation on Proteus, so this thesis will only elaborate on the main features that are relevant for this thesis research.

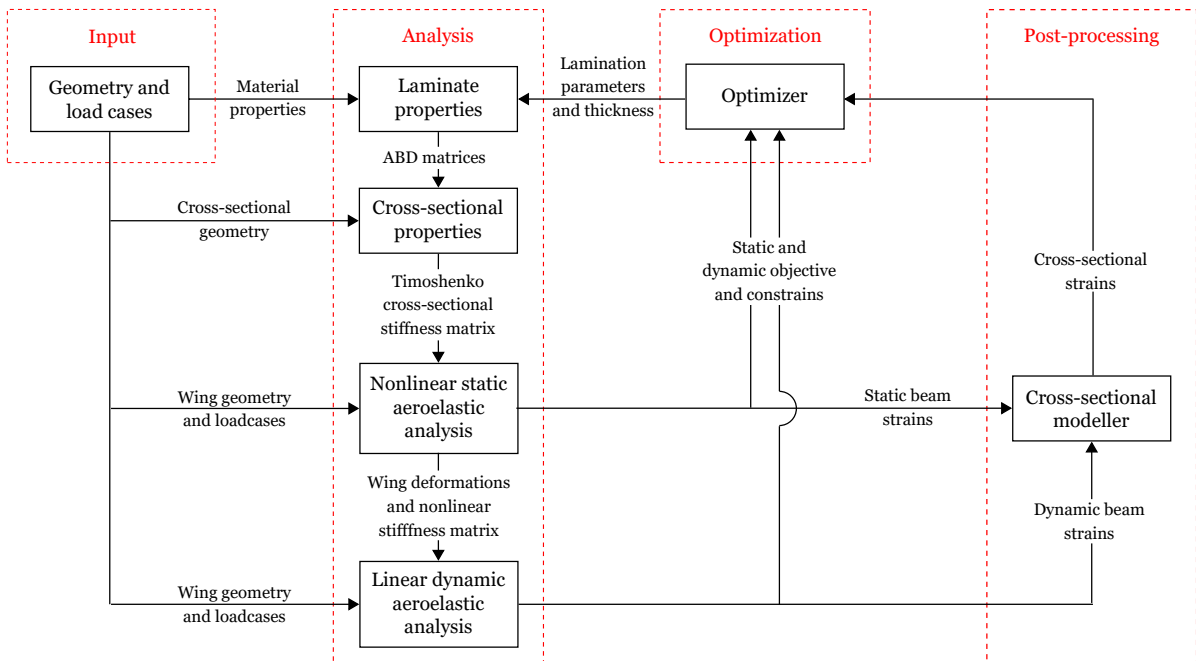


Figure 4.1: Schematic representation of original aeroelastic and optimization loop Proteus (Werter and De Breuker, 2015)

Figure 4.1 schematically presents the Proteus analysis and optimization loop. As can be seen, the input consists of wing geometry and load cases. The analysis is then performed based on these parameters, and includes the translation from the three-dimensional wing geometry to a beam model, a nonlinear static

aeroelastic analysis based on the work of De Breuker (2011) and a linear dynamic aeroelastic analysis based on the work of Werter (2012). After the analysis the cross-sectional modeller converts the strains and curvatures of the beam back to a three-dimensional wing. If the objective constraints are not met, the optimizer adjusts the lamination parameters and the thickness distribution as new input for the analysis loop. This analysis and optimization loop is run until all constraints are satisfied.

4.1.1. Structural model

The structural beam model that is used in the analysis is a geometrically nonlinear Timoshenko beam based on the co-rotational formulation of Battini and Pacoste (2002). The use of a Timoshenko beam allows for defining a reference axis in the wing around which the aerodynamic moment and cross-sectional stiffness can be calculated, and eliminates the need for computation of the location of the shear center for every design update (De Breuker, 2011).

The main idea of the co-rotational structural formulation that is applied in Proteus, is to decompose the motion of any element into a rigid body displacements and a pure deformational part by means of a local coordinate system that rigidly translates and rotates with the beam element (Battini and Pacoste, 2002). The elastic beam deformation is solved in the local element coordinate system, while geometric nonlinearities caused by large deformations are incorporated by the rigid displacements of the element frame (De Breuker, 2011).

For solving the elastic beam deformations a local element coordinate system needs to be defined, that moves rigidly with the deformations of the beam. The element formulation is based on a shear flexible element with 20 degrees-of-freedom (DOF) to support the use of anisotropic materials. The local element DOFs are depicted in figure 4.2. The variables on local level are related to those on a global level by transformation matrices. On this global level, each element connects two nodes and consequently has 12 DOFs, as depicted in figure 4.3. These global DOFs can either be set free or fixed, depending on the boundary conditions that are posed on a specific element. While forces and moments on a beam element are only associated with its end nodes, these global DOFs are key for implementation of the strut into Proteus.

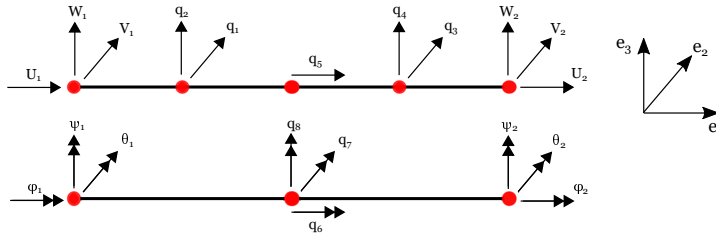


Figure 4.2: Local element degree-of-freedom definition

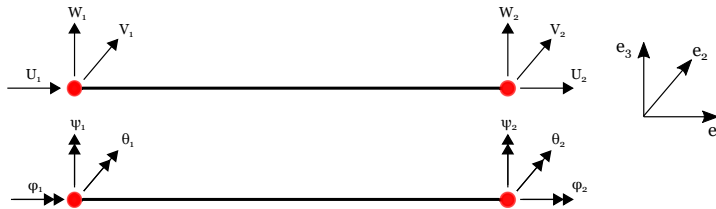


Figure 4.3: Global element degree-of-freedom definition

Gravity effects of structural and non-structural masses, and engine thrust effects are accounted for by eccentric follower and non-follower forces (Werter and De Breuker, 2015). For predicting the dynamic response mass properties of the wing cross-sections are resolved, after which the dynamic response is obtained by a linear dynamic analysis around the nonlinear static equilibrium solution (Werter and De Breuker, 2015).

4.1.2. Aerodynamic model

It was already pointed out in section 3.2 that the aerodynamic model is based on VLM with thin wing assumptions and unsteady VLM for dynamic aeroelastic analysis. Vortex ring elements are used for chordwise

and spanwise discretization of the camber surface and a spanwise distribution of rigid airfoils make up the aerodynamic mesh. The application of the Prandtl-Glauert correction to account for compressible flow yields the aeroelastic analyses are only to be valid for subsonic speeds.

4.1.3. Aeroelastic coupling

To obtain the aeroelastic model, the structural and aerodynamic models are coupled via state-space formulations. Flutter speeds are gathered by finding the eigenvalues that result in an unstable system. The geometrically nonlinear solution is obtained by the use of Newton-Raphson root finding methods in addition to load control (Werter and De Breuker, 2015).

4.1.4. Optimizer

The optimizer uses the gradient-based globally convergent method of moving asymptotes (GCMMA) optimization technique, and requires computation of the sensitivities of the objective function and constraints with respect to the design variables (De Breuker, 2011). Constraints can be posed on the lamination parameters, laminate strain, buckling and aeroelastic stability. The objective of the optimization can be set to either minimum weight or maximum range.

4.2. Implementation strategy

The strategy for implementation of the strut in Proteus is schematically shown in figure 4.4. Since a comparison of the aeroelastic behavior of an SBW configuration against a clean wing will provide valuable insight in the differences and benefits of one configuration over the other, Proteus should still be able to process clean wings. Therefore, a simple flag called `TRUSS` is introduced and marks whether a truss structure is included in the analysis or not. As was pointed out by section 3.2, this thesis research is focused on SBW configurations with a single strut member with hinged and ball-joint type connections to the wing and fuselage, respectively. The `TRUSS` flag only indicates the presence of the strut member. A second flag is added for including the hinging properties of strut-wing connection. When this `TRUSSHinge` flag is on, the strut can hinge with respect to the wing around the x-axis. If it is off, the strut-wing connection is fixed.

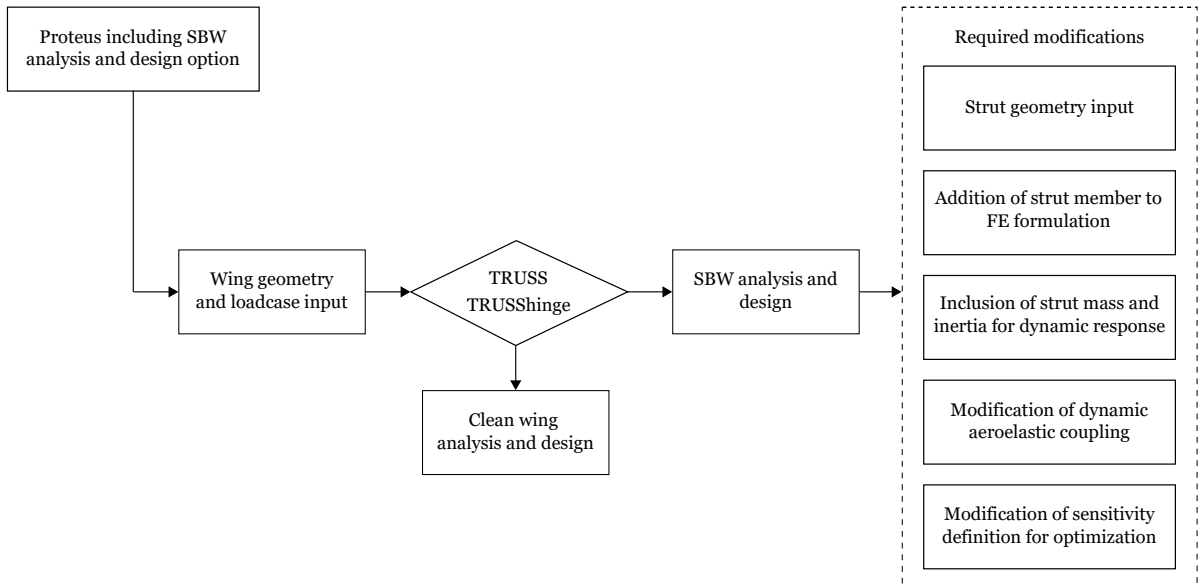


Figure 4.4: Strut implementation work breakdown structure

The first modification for the SBW analysis and design loop entails the addition of input files dedicated to the geometric and material properties of the strut member. Figure 4.5 shows the three geometric parameters that control the SBW configuration design. These parameters are the vertical location of the strut root with respect to the wing root, z_{strut} , the spanwise location of the strut-wing connection, y_{strut} , and the third parameter is the chordwise location of this connection, x_{strut} . These configuration parameters should be part of the input that is provided at the start of the Proteus analysis loop that was illustrated in figure 4.1. On

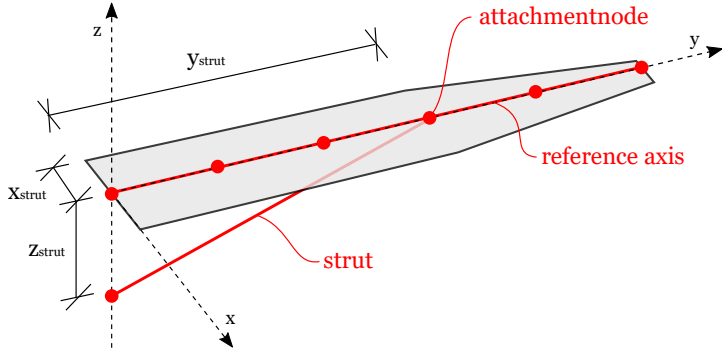


Figure 4.5: Geometric strut-braced wing configuration parameters

that account, the following input files are set up for the strut:

- Truss_Input
- DefineMaterialProp_Truss
- GenerateLaminateIniGuess_Truss

As the strut is assumed to not provide any lift, the aerodynamic model is not affected by the presence of the strut. The static and dynamic structural models, the aeroelastic coupling model and the sensitivity definitions remain for modification. Adjustments to the structural model mainly consist of the addition of the degrees of freedom (DOF) of the strut to the element freedom table of the full wing assembly. The dynamic model requires the addition of the strut mass and inertia. The coupling includes an update of the selection of the correct DOFs for assembling the state-space system. Finally, for the optimizer the sensitivity matrices need to include entries corresponding to the strut. Sections 4.3 until 4.5 will elaborate on how these inclusions are achieved.

4.3. Static solution

It was mentioned before that Proteus is based on nonlinear Timoshenko beam elements. For any wing that is being input the cross-sectional properties are projected onto a simple beam model. Figure 4.6a illustrates how such a model represents a clean wing. The wing is divided in a number of structural elements, in this case four. On the global level that was presented in figure 4.3, each element of the beam model connects two nodes and contains twelve DOFs in total. The first six DOFs of the first structural element are fixed ensure clamped boundary conditions at the wing root.

4.3.1. Addition of strut member

For the SBW configuration shown in figure 4.6b the clamped boundary conditions at the wing root are supplemented by a ball-joint type connection of the strut to the fuselage and a hinged connection of the strut to the wing. The representation in figure 4.6b is the basis for the implementation of the strut in the finite element (FE) solution.

The node that embodies the strut-wing connection is called `attachmentnode` and its y_{strut} -coordinate is defined in the input file, similar to the location of the strut-fuselage connection, z_{strut} . Since the wing is represented by a single beam model containing cross-sectional properties around a reference axis that is specified a priori, the strut connection needs to coincide with this reference axis, as is shown in figure 4.5. In that way it is ensured that the attachment node is coinciding both the wing and the strut at the same physical location, instead of creating an offset between the first node of the strut and the attachment location in the wing. Depending on the chordwise location x_{strut} of the strut-wing connection, the location of the reference axis of the wing is defined. Since the Timoshenko beam model allows the calculation of all beam properties around any arbitrary reference axis, shifting the axis does not have any implications on the structural or cross-sectional properties of the wing. Figure 4.7 demonstrates how the reference axis shifts with x_{strut} .

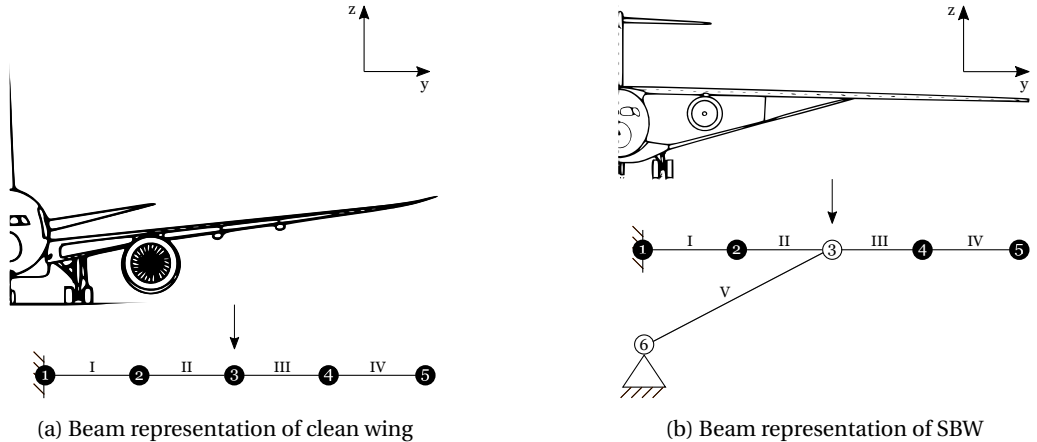
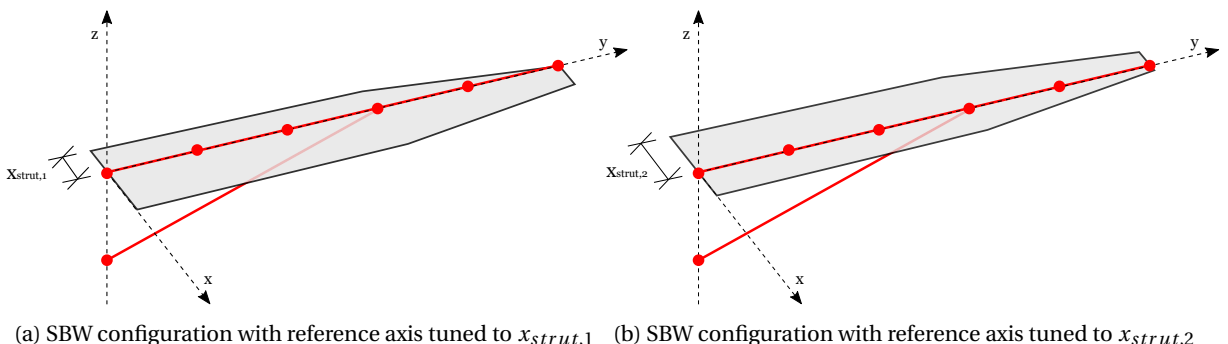


Figure 4.6: Beam representations of three-dimensional wing in Proteus

Figure 4.7: Demonstration of reference axis dependence on x_{strut}

4.3.2. Degrees of freedom

In figure 4.6b the hinging connections are indicated with white nodes. The SBW model in this figure consists of four wing elements and a single strut element. New DOFs need to be defined in the FE formulation to account for this strut member. Subsequently, the corresponding boundary conditions need to be applied to these new DOFs.

Figure 4.8 shows the DOFs per node for the same SBW model. The boxed DOFs are fixed, while the other DOFs are free. To ensure the hinging function around the x-axis at the strut-wing connection, a new independent DOF number 31 is added to node 3. Next to DOF 31, element V shares its other five DOFs at node 3 with element II and III, and thus stays dependent on all displacements of node 3 and on the rotation around its y-axis and z-axis.

Node 6 has six new DOFs that are totally independent of the DOFs of the wing. The ball joint is ensured by fixing the translational DOFs 32, 33, 34, while letting the rotational DOFs free. Table 4.1 represents the element freedom table that can be derived from figure 4.8. Together with table 4.2 that lists the free and fixed DOFs of this specific model, this is key input for the FE formulation of the full SBW assembly.

Table 4.1: Element freedom table

Element	First node	Second node	DOFs first node	DOFs second node
I	1	2	1, 2, 3, 4, 5, 6	7, 8, 9, 10, 11, 12
II	2	3	7, 8, 9, 10, 11, 12	13, 14, 15, 16, 17, 18
III	3	4	13, 14, 15, 16, 17, 18	19, 20, 21, 22, 23, 24
IV	4	5	19, 20, 21, 22, 23, 24	25, 26, 27, 28, 29, 30
V	3	6	13, 14, 15, 31 , 17, 18	32, 33, 34, 35, 36, 37

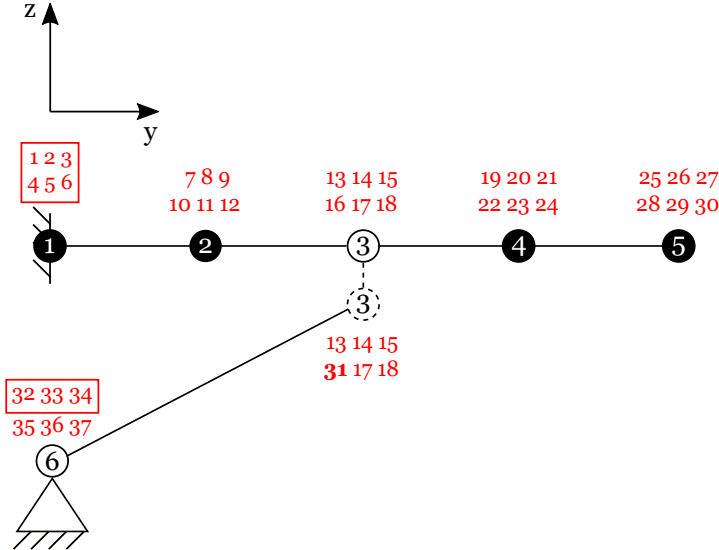


Figure 4.8: Degrees of freedom per node of SBW model

Table 4.2: Fixed and free degrees of freedom

Fixed DOFs	1, 2, 3, 4, 5, 6, 32, 33, 34
Free DOFs	7, 8, 9, 10, 11, 12, 13, 14, 15, 16, 17, 18, 19, 20, 21, 22, 23, 24, 25, 26, 27, 28, 29, 30, 31, 35, 36, 37

4.3.3. Beam element orientation

Section 4.1.1 pointed out how the co-rotational framework that defines the nonlinear structural model in Proteus is depending on the formulation of local element frames. The formulation of these local elements on the wing does not require any modification when the strut is implemented. However, for the strut member itself a new local element frame needs to be defined. This initial orientation frame \mathbf{T}_0 consists of vectors \mathbf{e}_1^0 , \mathbf{e}_2^0 , and \mathbf{e}_3^0 (De Breuker, 2011). \mathbf{e}_1^0 is oriented along the beam axis and is defined according to equation 4.1. $\mathbf{x}_{n,1}$ and $\mathbf{x}_{n,2}$ are the coordinates of the two end nodes of the beam. \mathbf{e}_2^0 and \mathbf{e}_3^0 are defined by equations 4.2 and 4.3, respectively. \mathbf{q}^0 is an auxiliary vector indicating the \mathbf{e}_3^0 -direction of the beam in global coordinates (De Breuker, 2011).

$$\mathbf{e}_1^0 = \mathbf{x}_{n,2} - \mathbf{x}_{n,1} \quad (4.1)$$

$$\mathbf{e}_2^0 = \frac{\mathbf{q}^0 \times \mathbf{e}_1^0}{\|\mathbf{q}^0 \times \mathbf{e}_1^0\|} \quad (4.2)$$

$$\mathbf{e}_3^0 = \mathbf{e}_1^0 \times \mathbf{e}_2^0 \quad (4.3)$$

The typical undeformed orientation systems for the wing beam elements are visualized in figure 4.9a. The undeformed strut element frame is depicted in 4.9b. It is important to note that the orientation of the strut member is defined from the attachment node at y_{strut} towards the fuselage connection at z_{strut} , and that this convention needs to be taken into account when submitting the strut geometry input to Proteus.

Having the initial orientation frame of the strut member defined, the rotated local element frame \mathbf{T}_r can be defined according to the explanation of De Breuker (2011).

4.3.4. Global stiffness formulation

The co-rotational FE framework in Proteus can be described by equation 4.4 (Battini and Pacoste, 2002). Here, \mathbf{K}^g is the global stiffness matrix, \mathbf{k}_l the tangent stiffness matrix in local coordinates, \mathbf{f}_l is the internal force vector, and \mathbf{B} and $\frac{\partial \mathbf{B}}{\partial \mathbf{p}^g}$ are transformation matrices between the local and global formulations. The second term on the right-hand side represents the geometric stiffness following from the co-rotational formulation (De Breuker, 2011).

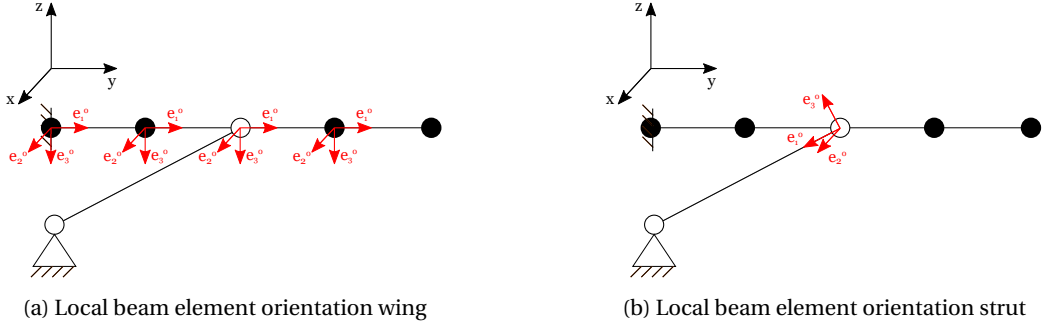


Figure 4.9: Local beam element orientation for SBW configuration

$$\mathbf{K}^g = \mathbf{B}^T \mathbf{k}_l \mathbf{B} + \frac{\partial \mathbf{B}}{\partial \mathbf{p}^g} : \mathbf{f}_l \quad (4.4)$$

For the addition of an extra member to the structural formulation, the global stiffness matrix \mathbf{K}^g needs to include the strut element in addition to the wing elements. This is done by repeating the computation of equation 4.4 for the strut element and its corresponding DOFs, and adding the stiffness matrix that follows to that of the wing elements. The final assembly of all stiffness matrices is typically defined by equation 4.5 (Cook et al., 2002). For the SBW configuration this expression can be written as is done in equation 4.6.

$$\mathbf{K} = \sum_{i=1}^{N_{el}} \mathbf{K}_i^g \quad (4.5)$$

$$\mathbf{K}_{full} = \sum_{i=1}^{N_{elwing}} \mathbf{K}_i^g + \sum_{j=1}^{N_{elstrut}} \mathbf{K}_j^g \quad (4.6)$$

The assembled stiffness matrix of the simple SBW configuration depicted in figure 4.8, is schematically presented in figure 4.10, where the blue dots represent the stiffness terms corresponding to the wing DOFs and the red dots represent those corresponding to the strut. The DOF numbers correspond to those listed in tables 4.1 and 4.2. The stiffness matrix in the figure shows that the strut indeed adds stiffness terms at the strut DOFs as expected, and thus suggests correct implementation of the strut into Proteus up to this point.

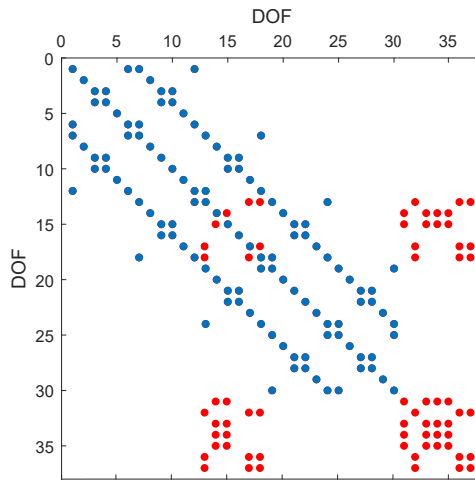


Figure 4.10: Assembled stiffness matrix including strut DOFs

4.3.5. Static aeroelastic solution

The static aeroelastic solution is finally defined in equation 4.7, which couples the assembled stiffness matrix \mathbf{K} to aerodynamic loads \mathbf{F}_a generated with VLM, and external loads \mathbf{F}_{ext} , by means of displacement vector δ .

$$\mathbf{K}\delta = \mathbf{F}_a + \mathbf{F}_{ext} \quad (4.7)$$

For the SBW assembly this equation can be written according to equation 4.8. Since the strut does not generate any lift, the aerodynamic load vector on the right-hand side of equation 4.7 only needs to be supplemented with zero-entries for the added SBW DOFs. For simplicity it is also assumed that no external forces work on the simplified strut in figure 4.8. Therefore, the external load vector \mathbf{F}_{ext} is also supplemented with zero-entries for the strut.

The strut in the verification model shown in figure 4.8 adds seven independent DOFs, thus the load vectors in 4.9 and 4.10 need to include seven zero-entries.

$$\mathbf{K}_{full}\delta = \mathbf{F}_{a_{full}} + \mathbf{F}_{ext_{full}} \quad (4.8)$$

$$\mathbf{F}_{a_{full}} = [\mathbf{F}_{a_{wing}} \quad 0 \quad 0 \quad 0 \quad 0 \quad 0 \quad 0]^T \quad (4.9)$$

$$\mathbf{F}_{ext_{full}} = [\mathbf{F}_{ext_{wing}} \quad 0 \quad 0 \quad 0 \quad 0 \quad 0 \quad 0]^T \quad (4.10)$$

From substitution of stiffness matrix \mathbf{K}_{full} , static aeroelastic load expression $\mathbf{F}_{a_{full}}$ and external force expression $\mathbf{F}_{ext_{full}}$ into equation 4.8, the static aeroelastic deformations can be calculated by standard FE practice.

4.4. Dynamic solution

The formulation of the dynamic response of a SBW configuration calls for incorporation of mass and inertia of the strut member into the mass and inertia definition of the full assembly.

4.4.1. Structural dynamics

The mass and inertia properties of the strut are calculated in the same way they are calculated for the wing elements, as explained in (Werter, 2012).

The global mass matrix is assembled from the local element matrices in a standard FE fashion (Werter and De Breuker, 2015). The mass of the strut can thus be included in the global mass matrix by a procedure similar to the one that was described earlier for assembly of the stiffness matrix, and can be specified by equation 4.11.

$$\mathbf{M}_{full} = \sum_{i=1}^{N_{el_{wing}}} \mathbf{M}_i + \sum_{j=1}^{N_{el_{strut}}} \mathbf{M}_j \quad (4.11)$$

The linear dynamic structural model is then given by equation 4.12, where \mathbf{M}_{full} is the mass matrix of the full assembly, \mathbf{K}_{full} is the stiffness matrix, \mathbf{F} is the force vector, and \mathbf{p} contains the structural degrees of freedom.

$$\mathbf{M}_{full}\ddot{\mathbf{p}}_{full} + \mathbf{K}_{full}\mathbf{p}_{full} = \mathbf{F}_{full} \quad (4.12)$$

The eigenvalues of the updated system in equation 4.12 are the natural eigenvalues of the SBW configuration, and the corresponding eigenvectors are the natural modes of the configuration.

4.4.2. Dynamic aeroelastic coupling

The final next modification for implementation of the SBW design option in Proteus, is subjected to the coupling of the dynamic aerodynamic and dynamic structural model. This coupling is done with a the single state-space system that is thoroughly explained by Werter and De Breuker (2015), and is for a large part based on the selection of the proper DOFs for assembly of the state matrices.

For implementation of the strut into the state-space system, the independent DOFs of the strut are to be taken into account. Building forth on the model presented in section 4.3, this entails that the independent DOFs of element V listed in table 4.1 are added to the space-state system.

4.5. Sensitivities and optimization

Section 3.2 pointed out that the strut itself, or its geometric parameters are not the main subject of tailoring during optimization of the SBW configuration. This does however not mean that the strut can be excluded from the optimization procedure altogether. To further explain this, the optimization formulation in equation 4.13 is reviewed. Here, $f(\mathbf{x})$ is the objective function that is subjected to constraints g_i with respect to design variables \mathbf{x} (De Breuker, 2011). These design variables are the lamination parameters that describe the laminates in the wing and strut cross-sections.

$$\min f(\mathbf{x}) \quad (4.13a)$$

$$\text{subject to } g_i(\mathbf{x}) \quad (4.13b)$$

Equation 4.14 shows that the objective function within a certain design iteration is essentially constructed by multiplying the sensitivity of the objective function with respect to the design variables, with the actual design variables that are the result of that iteration.

$$\frac{df(\mathbf{x})}{d\mathbf{x}} \cdot \Delta\mathbf{x} = f(\mathbf{x}) \quad (4.14)$$

Since optimization of the strut itself is not the goal of aeroelastic tailoring of SBW configurations in this thesis work, the response of the strut to the design iteration is forced to be equal to zero. The expansion of equation 4.14 into equation 4.15 for the SBW optimization procedure shows how the strut is included in the optimization objective. Subscript w indicates that the variable belongs to the wing, whereas subscript s indicates a property of the strut.

When taking out the expression for the wing optimization objective f_w from equation 4.15, the expression in equation 4.16 is found. This expression shows that although the response of the strut is equal to zero, the strut still has an influence on the design objective of the wing f_w by means of its design variables in $\frac{df_w}{d\mathbf{x}_s}$ and \mathbf{x}_s . For this reason the sensitivity matrices that are used for optimization of the SBW need to be updated to include entries corresponding to the strut.

$$\begin{bmatrix} \frac{df_w}{d\mathbf{x}_w} & \frac{df_w}{d\mathbf{x}_s} \\ \frac{df_s}{d\mathbf{x}_w} & \frac{df_s}{d\mathbf{x}_s} \end{bmatrix} \begin{bmatrix} \mathbf{x}_w \\ \mathbf{x}_s \end{bmatrix} = \begin{bmatrix} f_w \\ 0 \end{bmatrix} \quad (4.15)$$

$$\frac{df_w}{d\mathbf{x}_w} \cdot \mathbf{x}_w + \frac{df_w}{d\mathbf{x}_s} \cdot \mathbf{x}_s = f_w \quad (4.16)$$

An elaborate description on the actual generation of the sensitivities is given by Werter (2012), so this section will only comment on how the sensitivities are updated. In practice the existing sensitivity matrices in Proteus are simply expanded for the full SBW assembly, including the DOFs of the strut. The input variables that are stored in `constant` for the wing and in `constant.truss` for the strut are stacked together into `constant.full`, which is then used as input for all sensitivity-generating functions throughout the code. As a result the sensitivities that correspond to the different parts of the code, such as to lamination parameters, cross-sectional stiffness, static aeroelastic analysis, and dynamic aeroelastic analysis, are step by step modified.

A large number of these sensitivities is not directly, but rather indirectly related to design variables \mathbf{x} . The sensitivity of the lift generated by the wing is for example not directly dependent on the design variables, but on displacement vector \mathbf{p} . This vector \mathbf{p} is in turn dependent on stiffness matrix \mathbf{C} , which is linked to the design variables by means of the constitutive lamination matrices \mathbf{A} and \mathbf{D} , as is shown in equation 4.17.

$$\frac{\partial \mathbf{L}}{\partial \mathbf{x}} = \frac{\partial \mathbf{L}}{\partial \mathbf{p}} \cdot \frac{\partial \mathbf{p}}{\partial \mathbf{C}} \left(\frac{\partial \mathbf{C}}{\partial \mathbf{A}} \cdot \frac{\partial \mathbf{A}}{\partial \mathbf{x}} + \frac{\partial \mathbf{C}}{\partial \mathbf{D}} \cdot \frac{\partial \mathbf{D}}{\partial \mathbf{x}} \right) \quad (4.17)$$

Since the strut does not generate any lift, the aerodynamic sensitivities are essentially not affected by the addition of the strut. This is also the case for $\frac{\partial \mathbf{L}}{\partial \mathbf{p}}$. For linking this expression to the structural formulation of the full SBW assembly, it needs to be linked to the array of structural coordinates of the full SBW assembly,

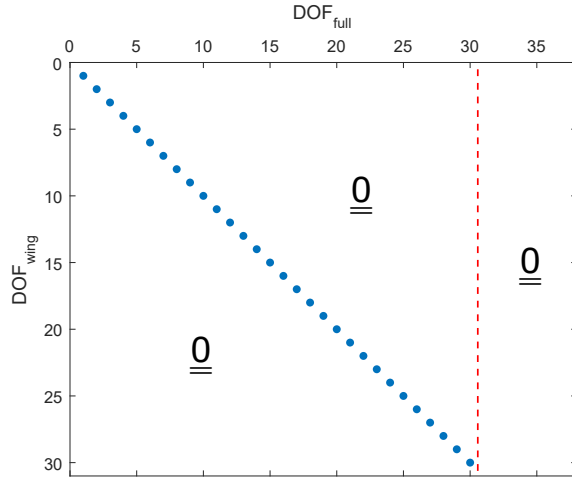


Figure 4.11: Transformation matrix to transform from wing DOFs to full assembly DOFs

and account for the addition of the number of DOFs associated with the strut $N_{DOF_{strut}}$. Equation 4.18 shows how the chain rule can be used to express this derivative in terms of the deformations of the full assembly.

$$\frac{\partial \mathbf{L}}{\partial \mathbf{p}} = \frac{\partial \mathbf{L}}{\partial \mathbf{p}_{wing}} \cdot \frac{\partial \mathbf{p}_{wing}}{\partial \mathbf{p}_{full}} \quad (4.18)$$

As any vector containing variables that belong to the wing is typically a subset of the same vector belonging to the full assembly, the second term on the right-hand side of equation 4.18 can be constructed by adding $N_{DOF_{strut}}$ zero-entry columns to a $N_{DOF_{wing}}$ by $N_{DOF_{wing}}$ identity matrix. Here $N_{DOF_{strut}}$ is the number of DOFs solely corresponding to the truss (and in this case strut) structure, and $N_{DOF_{wing}}$ is the number of DOFs corresponding to the wing.

Because the cross-sectional analysis is carried out for separate input of the wing and strut, the resulting design variables from any iteration are decomposed into a wing and strut array for analysis, after which they are stacked together again for the aeroelastic analysis and dynamic analysis. Figure 4.12 visualizes the flow of the aeroelastic optimization procedure for SBW configurations in Proteus. A comparison of figure 4.12 to figure 4.1 shows the largest modification blocks in the overall analysis and design loop for this new configuration in Proteus.

Next to the expansion of the sensitivity matrices, the list of design constraints also needs to be updated to include the constraints that correspond to the strut member. This is however simply covered by feeding the full assembly data into the strain, buckling and lamination parameter calculation functions, as depicted in figure 4.12.

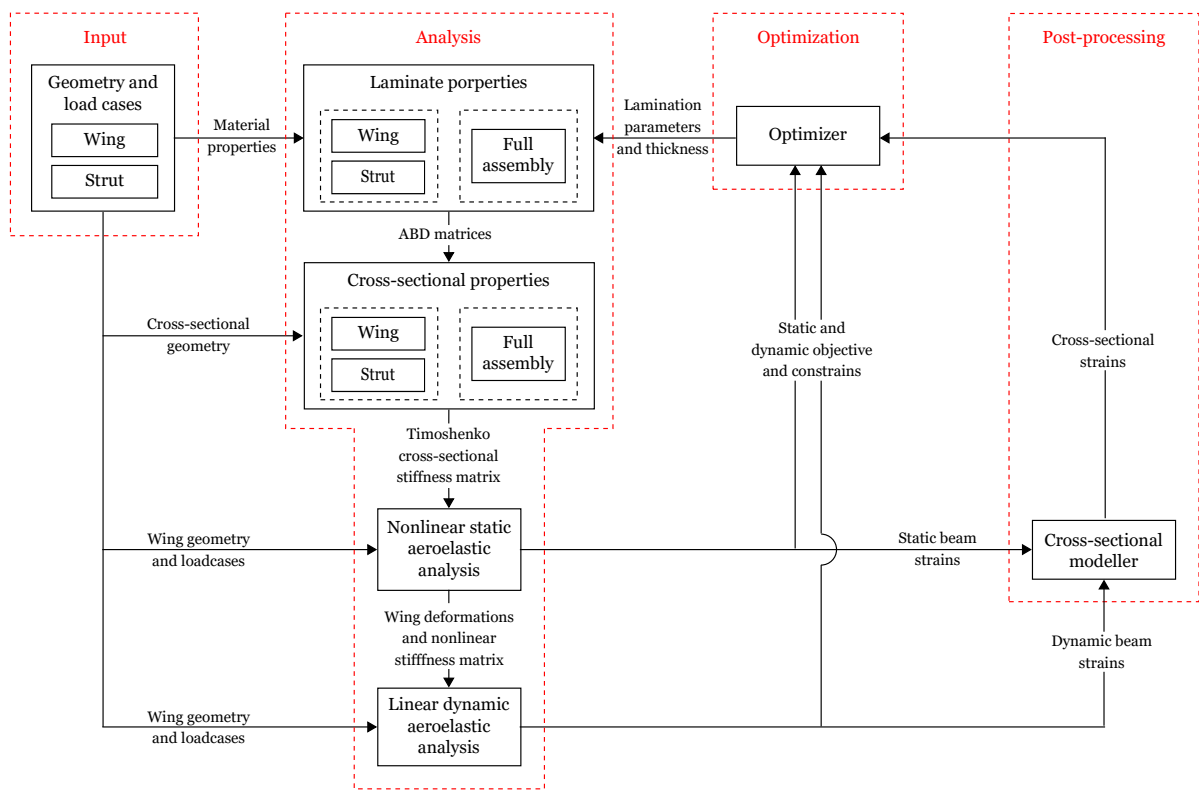


Figure 4.12: Schematic representation of modified aeroelastic and optimization loop Proteus

5

Verification

The modifications for enabling Proteus to analyze SBWs need to be verified before the framework can be used to analyze and design actual SBWs. First the static solution of the wing under a tip load is verified, followed by the dynamic solution containing eigenmodes and frequencies of the wing. Then the aeroelastic loads under a prescribed test case follow, and finally the flutter solution is verified. The reference data used for these verifications is generated with MSC Nastran analyses on the verification model that is discussed in section 5.1.

5.1. Verification model

For verification of the implementation of the strut a simple SBW model based on the Goland wing with a NACA0012 airfoil is used. The Goland wing was first introduced by Martin Goland and has been widely employed to verify aeroelastic models since (Goland, 1945). The structural properties of the Goland wing are listed in table 5.1. The remaining properties that are required for this verification study, are estimated assuming a rectangular wing box cross-section ranging 25% c to 75% c and aluminum 2024-T3 material properties (table 5.2). They are summarized in table 5.3.

The aluminum strut is attached at midspan and at 50% of the Goland chord. The other end of the strut is positioned at $z_{strut} = 1\text{m}$ below the root of the wing. A square strut cross-section is assumed of which the properties are listed in table 5.3 as well.

Table 5.1: Goland wing properties (Goland, 1945)

Property	Magnitude
$b[m]$	6.096
$c[m]$	1.8288
$EI_{22}[\text{Nm}^2]$	$9.77 \cdot 10^6$
$GJ[\text{Nm}^2]$	$9.88 \cdot 10^5$
$\rho I_p[\text{kNm}]$	7.47

Table 5.2: Aluminum 2024-T3 properties

Material property	Magnitude
$E [\text{GPa}]$	$7.31 \cdot 10^{10}$
$G [\text{GPa}]$	$2.80 \cdot 10^{10}$
$\rho [\text{kg/m}^3]$	2780

5.2. Static solution

For verification of the static FE solution a downward tip load is introduced on the Goland wing in Proteus and the velocity is set to $V = 0.01\text{ m/s}$ to exclude the occurrence of aerodynamic loads.

Table 5.3: Additional properties for SBW verification model

	Property	Magnitude
Wing	$I_{11}[m^4]$	$2.55 \cdot 10^{-3}$
	$I_{22}[m^4]$	$1.34 \cdot 10^{-4}$
	$J[m^4]$	$3.53 \cdot 10^{-5}$
	$A[m^2]$	$1.28 \cdot 10^{-2}$
Strut	$I_{11}[m^4]$	$2.67 \cdot 10^{-5}$
	$I_{22}[m^4]$	$2.67 \cdot 10^{-5}$
	$J[m^4]$	$4.00 \cdot 10^{-5}$
	$A[m^2]$	$4.00 \cdot 10^{-3}$

A tip load of 50 kN is applied to ensure a significant deflection of the wing. The result is verified with results of a Nastran SOL 101 analysis on the same beam model. The CBAR and PBAR cards are used to input the beam elements and beam properties (MSC Software Corporation, 2016b).

Tip deflection results of both analyses are shown in figure 5.1. The deflection of the clean Goland wing is also depicted to indicate the influence of the strut on the static deflection. It can be seen that for the current load case and SBW design the strut limits the tip deflection to one third of the clean wing deflection. Furthermore, it is clear that Proteus results perfectly agree with the Nastran verification results. Table 5.4 presents the numeric verification results and shows that the relative error between the Proteus and Nastran model is only 0.03%. Altogether, this confidently leads it to conclude that the strut is correctly implemented with regard to the static FE solution.

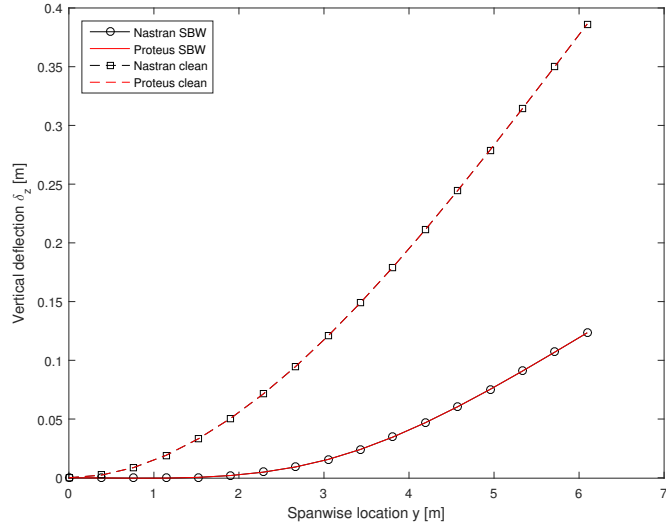


Figure 5.1: Verification results of static solution for Goland beam under 50 kN tip load

Table 5.4: Beam tip deflection verification results

Property	Nastran	Proteus	Difference [%]
$\delta_z[m]$	0.1234	0.1235	0.0258
$\theta_x[^\circ]$	0.0433	0.0433	0.0297

5.3. Dynamic solution

To be able to perform dynamic aeroelastic analyses on the SBW, the natural modes and frequencies need to be correct as well. For validation of the structural dynamic solution of the SBW in Proteus, the natural modes and frequencies resulting from the analysis are compared to the results of a Nastran SOL 103 analysis. Whereas Proteus uses a continuous mass formulation, the default mass formulation of the CBAR card that is used to model the beam in Nastran does not include torsional inertia and translates the bar mass to the

nearest grid points (MSC Software Corporation, 2016a). To be able to compare the natural frequencies and modes that follow from Proteus to Nastran, additional Nastran cards are included in the verification model for taking inertia and coupled mass effects into account. These are the COUPMASS parameter card and the BARMASS executive system parameter card (MSC Software Corporation, 2016b).

A Lanczos eigenvalue analysis is performed using the EIGRL card, with a MAX entry for normalization with respect to the maximum excitation. The eigenfrequency results of Proteus are compared to those from the Nastran verification model in figure 5.2 and table 5.5. The Proteus and Nastran eigenfrequencies agree reasonably well with each other. The largest errors exist for mode 2, mode 4 and mode 8, which are the first, second and third torsional mode, respectively. This implies that the torsional inertia formulation of the Nastran model is still different from the one in Proteus. At the same time the eigenmodes that are computed by both models show good similarity, as is shown in figure 5.3.

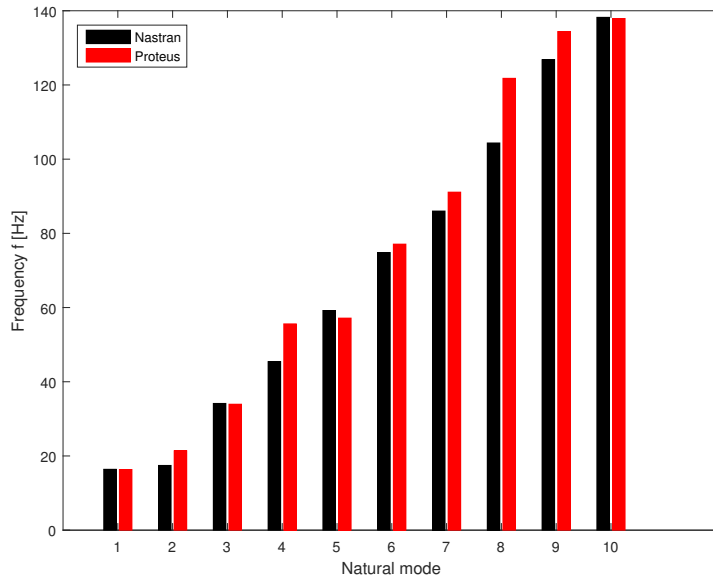


Figure 5.2: Verification results of natural frequencies of strut-braced Goland beam

Table 5.5: Natural frequency verification results - continuous mass model

Mode	Nastran [Hz]	Proteus [Hz]	Difference [%]
1	16.40	16.35	0.32
2	17.44	21.39	22.62
3	34.15	33.94	0.62
4	45.43	55.60	22.37
5	59.21	57.15	3.47
6	74.83	77.09	3.03
7	86.00	91.10	5.93
8	104.36	121.78	16.70
9	126.82	134.39	5.97
10	138.22	137.91	0.22

Since the errors between the Proteus and Nastran results for torsional modes are relatively large, a final check is done based on a lumped mass model. For this simplified model the density of the beam material is set equal to 1kg/m^3 and lumped masses of 1 kg each are added to the nodes of the beam, as shown by figure 5.4. The COUPMASS and BARMASS Nastran cards are discarded for this analysis, which means that the results of the Proteus and Nastran analyses should be exactly comparable. The results in figure 5.5 and table 5.6 finally also confirm the verification of the structural dynamic solution for mode 2, mode 4, and mode 8.

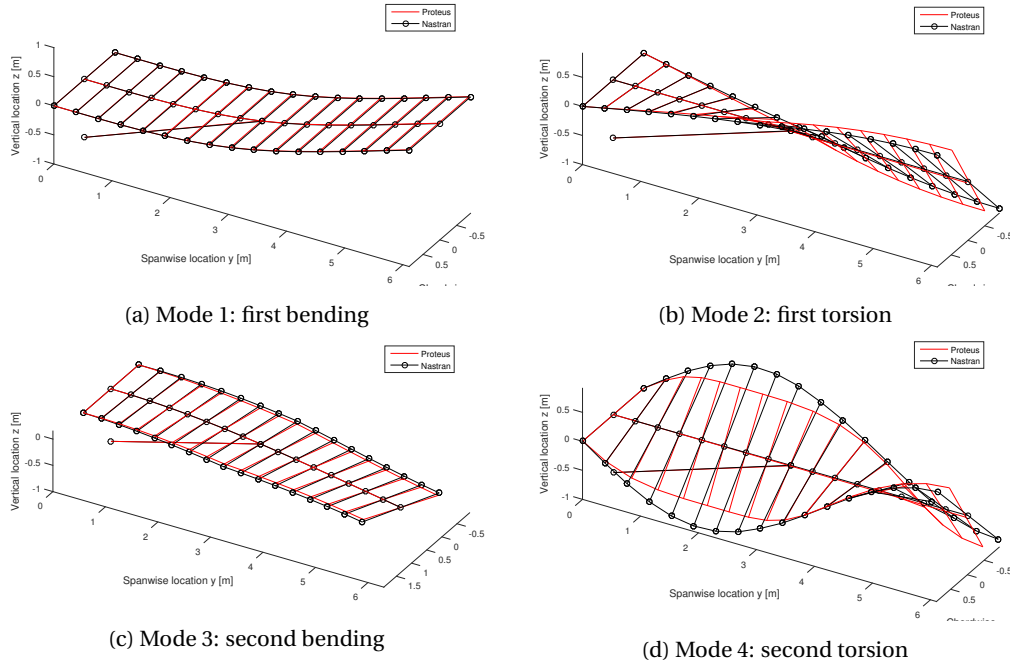


Figure 5.3: Eigenmode comparison for verification of structural dynamic solution

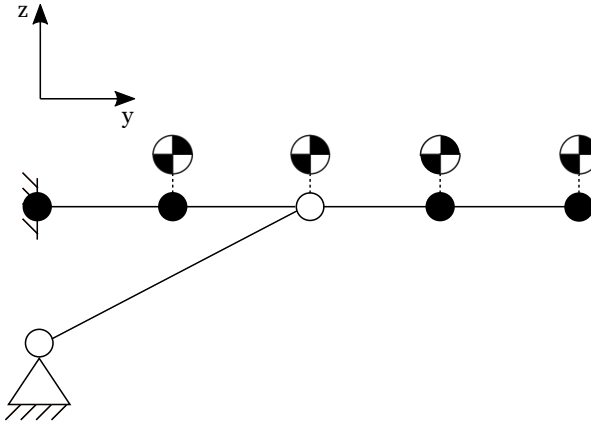


Figure 5.4: Example of lumped mass model for verification of structural dynamic solution

5.4. Aeroelastic loads

Now the structural solution of the SBW has been verified, it is time to look into the aeroelastic solution. First the static aeroelastic loads are examined and compared to the results of a Nastran SOL 144 analysis. The SPLINE2 card is used in Nastran to spline the aerodynamic surface definition onto the Goland beam. The DIVERG card is exploited to find the divergence speed, using a Mach number equal to 0.0 (MSC Software Corporation, 2016b). Table 5.7 summarizes the verification test case parameters that are applied. The resulting static deflections are shown in figure 5.6a to 5.6c and numerically presented in table 5.8. The results show that the static aeroelastic deformations obtained with Proteus agree well with the Nastran results. The comparison of divergence velocity results demonstrates good agreement as well, and thus it can be concluded that the implementation of the strut into the static aeroelastic solution in Proteus has been verified.

5.5. Flutter solution

As a final step in the verification of the aeroelastic solution of the SBW option in Proteus, the dynamic aeroelastic results are compared to those coming from a Nastran SOL 145 flutter solution. For this solution a continuous mass formulation is forced in Nastran by including the COUPMASS parameter card and the BARMASS

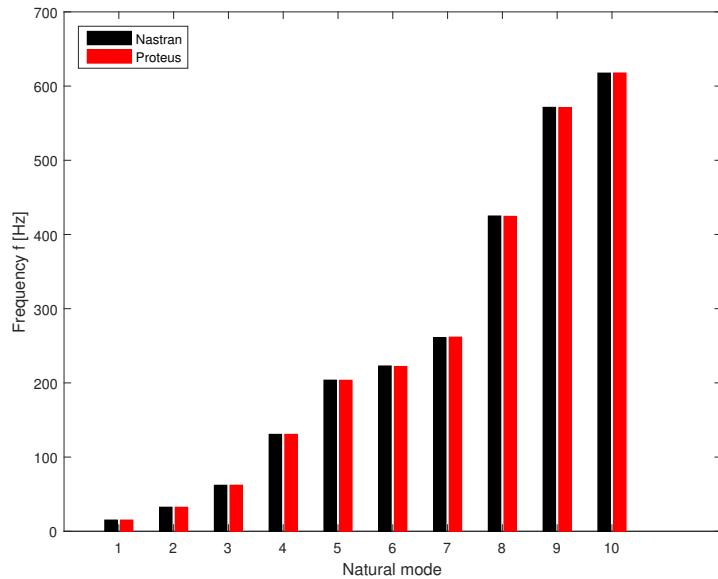


Figure 5.5: Verification results of natural frequencies of lumped mass strut-braced Goland beam

Table 5.6: Natural frequency verification results - lumped model

Mode	Nastran [Hz]	Proteus [Hz]	Difference [%]
1	15.16	15.15	0.01
2	32.44	32.44	0.00
3	62.14	62.13	0.01
4	130.70	130.68	0.02
5	203.55	203.54	0.00
6	222.15	222.15	0.00
7	261.75	261.70	0.02
8	424.57	424.48	0.02
9	571.12	571.05	0.01
10	617.68	617.65	0.00

executive system parameter (MSC Software Corporation, 2016b).

Both the complex and real eigenvalues are obtained with a Lanczos eigenvalues analysis in Nastran (EIGC and EIGRL cards, with MAX normalization entries). Analogous to the static aeroelastic verification procedure, the test case parameters listed in table 5.7 are applied for the flutter velocity verification.

To cross-check correct implementation of all parameters in Nastran, a flutter analysis of the clean Goland wing is done as well. The results of all flutter analyses are presented by table 5.9. As can be seen the clean wing is critical for flutter, while the SBW configuration is critical for divergence. Flutter occurs only at a very high velocity. Although this velocity is rather unrealistic considering any physical application, it still shows that the Proteus results are in good agreement with the reference solution in Nastran for the given conditions and thus that SBW analysis in Proteus is verified.

Flutter occurs when the third and fourth mode coalesce, which is in agreement with the findings of Zhao et al. (2015) for aeroelastic behavior of SBWs.

5.6. Sensitivity calculation

The calculation of the sensitivities corresponding to the lamination parameters, the cross-sectional stiffness, static aeroelastic analysis and dynamic aeroelastic analysis needs to be verified for correct implementation. To this end a finite difference check is performed for all sensitivity matrices. This check consists of the application of a small perturbation e to variable x . The slope of the evaluated results $f(x)$ can be calculated with the forward differential expression given by equation 5.1. The sensitivity of any function f to perturbation e is then compared to slope $\frac{\delta f}{\delta x}$ to check whether it has been calculated correctly.

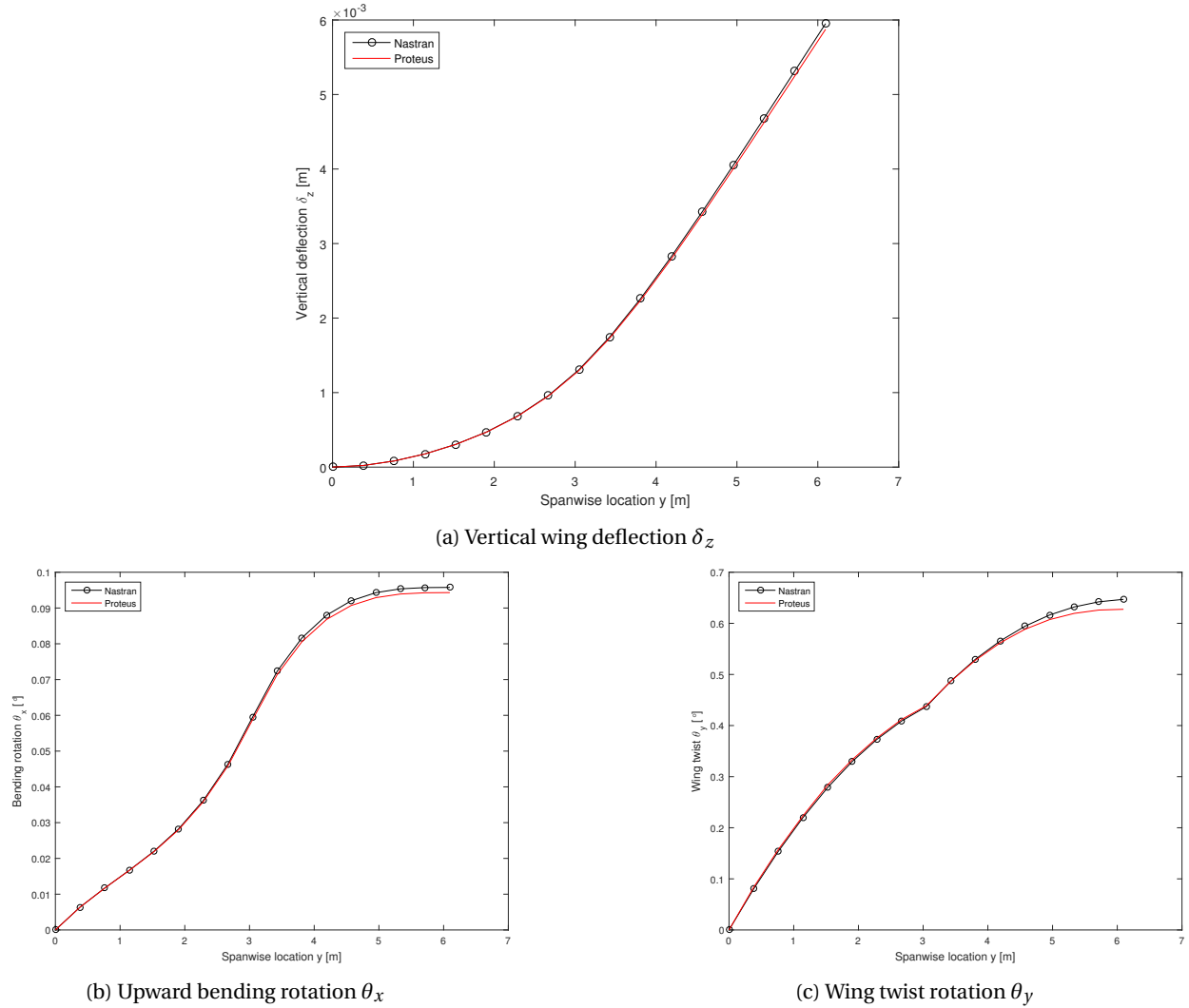


Figure 5.6: Verification results of static aeroelastic deflections for strut-braced Goland wing model

$$\frac{\partial f}{\partial x} = \frac{f(x+e) - f(x)}{e} \quad (5.1)$$

Table 5.7: Static aeroelastic verification case parameters

Parameter	Magnitude
M	0.0
Structural elements (spanwise)	16
Aerodynamic panels (spanwise)	16
Aerodynamic panels (chordwise)	5
$\alpha [^\circ]$	3.34
V [m/s]	75
h [m]	0

Table 5.8: Static aeroelastic verification results

Property	Nastran	Proteus	Difference [%]
$\delta_z[m]$	0.0060	0.0059	1.29
$\theta_x[^\circ]$	0.0017	0.0016	1.51
$\theta_y[^\circ]$	0.0113	0.0110	3.01
L [N]	11107	11062	0.41
$V_{div}[m/s]$	221	219	0.90

Table 5.9: Flutter verification results

		Nastran		Proteus		Difference [%]	
		V [m/s]	f [Hz]	V [m/s]	f [Hz]	Velocity	Frequency
Clean wing	Flutter	150	10.74	159	12.11	6.00	12.86
	Divergence	182	[-]	183	[-]	0.55	[-]
Strut-braced wing	Flutter	607	19.61	618	20.50	1.81	4.51
	Divergence	217	[-]	219	[-]	0.92	[-]

6

Optimization settings

In order to answer the research question, a series of optimizations needs to be set up. This chapter discusses the considerations that are involved, and the analyses that were performed to define the outer wing geometry, load cases, and strut configurations for design of the optimization settings.

6.1. Test case objectives

In section 3.1 the objective of this thesis work was discussed. One of the goals is to investigate the influence of the strut configuration on the outcome of aeroelastic tailoring procedures. Geometric parameters such as y_{strut} and x_{strut} of the SBW configuration are therefore not tailored in the optimizer. Moreover, because the mechanical properties of the strut itself do not have to be optimized for deriving an answer to the research question, the strut properties will be kept constant over the course of each optimization procedure. Optimizations consequently only entail tailoring of the wing for a fixed strut configuration. The influence of the strut on the tailoring result will therefore be examined by means of the outcome of a parametric study containing tailored SBW designs for different strut configurations.

This parametric study consists of a number of separate optimizations that is run for each a different SBW configuration. The examined SBW configurations are the result of combining different strut parameters with each other. The geometric configuration parameters that can be of interest in this investigation were depicted in figure 4.5. Next to the geometric parameters, the influence of the mechanical properties of the strut will be considered. The strut is modelled as a single elastic member in the SBW, with hinged connections on both ends. Its axial stiffness is thus the only mechanical property that has an influence on the aeroelastic behavior of the wing. Together with the spanwise and chordwise location of the strut-wing connection and the vertical location of the strut root, the axial stiffness of the strut completes the set of parameters that will be examined in this study.

The different SBW configurations that will be part of this research will be optimized for a design objective of minimum total mass. The total mass includes both the structural wing mass and structural strut mass.

From a review on the optimization results for all these configurations, conclusions can be drawn on the influence of the strut on aeroelastic tailoring. In addition, the best SBW design resulting from the study will be analyzed for its aeroelastic behavior.

6.2. Geometry and material

The SBW model that will be subject of the present work is a wing model that is partly based on the Boeing SUGAR planform, and that is scaled down and simplified for potential future aeroelastic wind tunnel tests. Geometry and material properties are established to enable these potential future experiments.

6.2.1. Material

To facilitate aeroelastic tailoring of the SBW composite laminate material will be used. With regard to material availability in the DASML composite lab, carbon fiber AS4/8552 material was chosen for its excellent properties. The properties of the AS4/8552 carbon fiber material are listed in table 6.1.

The maximum strain allowables in table 6.1 are including standard B-basis knockdown factors for worst environment, material scatter and barely visible impact damage (Kassapoglou, 2010).

Table 6.1: AS4/8552 material properties (Composites, 2013)

Property	Magnitude
$\rho [kg/m^3]$	1580
$E_{11} [Pa]$	$141 \cdot 10^9$
$E_{22} [Pa]$	$10 \cdot 10^9$
$G_{12} [Pa]$	$7 \cdot 10^9$
$\nu [-]$	0.3
$t_{ply} [m]$	0.00015
$X_t [Pa]$	$2207 \cdot 10^6$
$X_c [Pa]$	$1531 \cdot 10^6$
$Y_t [Pa]$	$81 \cdot 10^6$
$Y_c [Pa]$	$228 \cdot 10^6$
$S [Pa]$	$114 \cdot 10^6$
$\epsilon_{max} [-]$	0.0155
$\epsilon_{min} [-]$	-0.012
$\gamma_{max} [-]$	0.0189

For the strut an acrylate polymer material called Perspex is used as a reference. However, since the axial stiffness of the strut is one of the configuration parameters that will be varied in order to create different SBW test cases, stiffness properties will not be based on material specifications. Instead the stiffness properties are given as input from the optimization settings. The only material properties that are based on actual material data are listed in table 6.2. The corresponding shear modulus for any given elastic modulus is then derived with equation 6.1.

Table 6.2: Perspex material properties (Theplasticshop.co.uk)

Property	Magnitude
$\rho [kg/m^3]$	1180
$\nu [-]$	0.3

$$G_{12} = \frac{E_{11}}{2 * (1 + \nu)} \quad (6.1)$$

6.2.2. Planform

The size and shape of the wing are dominated by the wing planform. Currently, the most advanced TBW aircraft design existing in literature is the Boeing SUGAR TBW aircraft, which has an aspect ratio of 19.6 (Bradley et al., 2015). Since the goal of this thesis is to investigate a competitive SBW, it will be aiming at designing a wing with a similar aspect ratio. In case of future windtunnel experiments at TU Delft, the actual dimensions of the test wing will be dominated by the size of the autoclave that is required for curing a thermoset carbon fiber material. The TU Delft Scholz autoclave has an inner depth of 1.70 m (TUDelft). To ensure sufficient spacing for vacuum pumps and proper installation of the vacuum bag around the curing wing skins a maximum wing span of 1.50 m is set.

Combining the maximum possible wingspan with the pursued aspect ratio in equation 6.2, the chord length is set to 0.155 m, resulting in a final aspect ratio of 19.4. Note that b is representing half of the wing span in this report, as opposed to the conventional full span.

$$AR = \frac{(2b)^2}{S} \quad (6.2)$$

6.2.3. Airfoil

Ideally, thin airfoils would be used in case of any wind tunnel experiments in order to achieve higher deflections and to minimize the potential for flow separation. However, the extreme slenderness of the high aspect

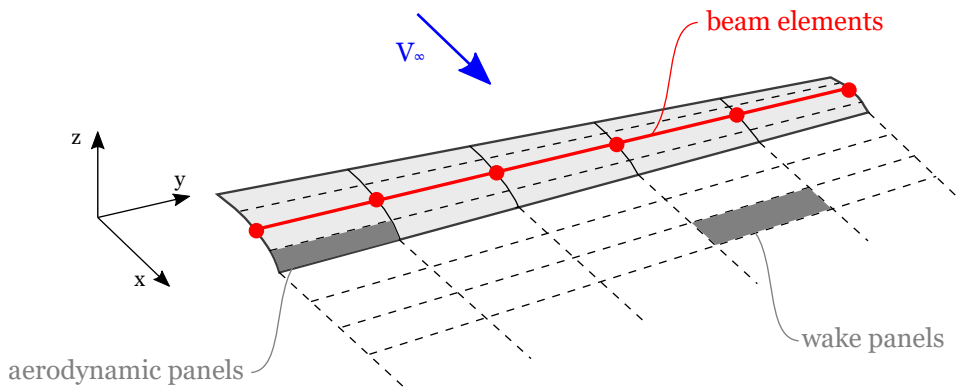


Figure 6.1: Typical discretization of wing model in Proteus

ratio SBW leaves little space for an inner wing structure. In light of possible future test model manufacture, this can complicate test model fabrication significantly. As a compromise between little flow separation and inner wing structure accommodation, it is decided that the wing will have a NACA0012 airfoil, resulting at a maximum wing thickness of 18.6 mm for the current planform. The inner structure of the wing consists of two spars, placed at 25% and 75% of the wing chord.

6.3. Modelling parameters

Any analysis or optimization in Proteus requires input of parameters that define the accuracy of the calculations and thus of the results. These inputs include the number of discretization elements used for the analysis. Figure 6.1 shows how a typical wing is discretized in Proteus. Analyses with a relatively high number of aerodynamic panels or beam elements produce more accurate results in general. However, increasing the number of panels also results in longer computation times.

Therefore, the number of panels and elements is selected such that no significant losses in accuracy occur while retaining computation time within limits. To find the number of panels that fulfills these requirements best, a convergence study was performed.

6.3.1. Convergence study for number of structural elements

Firstly, the number of required structural beam elements was investigated. With this intention an arbitrary quasi-isotropic (QI) wing having the geometric properties discussed in section 6.2 was subjected to a distributed load of 1 N in total over its full beam span. The resulting tip deflection was then plotted against the number of beam elements used for the computation. The results are shown in figure 6.2a, while the relative error with respect to the result obtained with 64 beam elements is depicted in figure 6.2b.

It can be seen that the tip displacement rapidly decreases for an increasing number of beam elements and that convergence is achieved for already eight to ten beam elements. This data point corresponds to a relative error of about 0.5%. Given these points, there is no significant benefit in further increasing the number of beam elements and therefore ten structural elements will be used as input for the SBW model.

The number of cross-sectional elements is also one of the key drivers for computational speed in Proteus. With the current spar configuration with spars at 25% and 75%, the minimum number of cross-sectional elements that can be achieved is 75. Since the influence of this parameter on the analysis result is minute, the minimum is selected for later analyses as to minimize computation time.

6.3.2. Convergence study for number of aerodynamic panels

Figure 6.3 shows the results of the convergence study for the number of aerodynamic panels in spanwise direction. Total lift is used as a measure of accuracy in this study, which was conducted at an airspeed of 25 m/s and angle of attack of 3.5°. As can be seen in figure 6.3a the total lift converges gradually to approximately 29.9 N. The relative error ranges from approximately 5.4% to 0.3%. An error below 1% requires a minimum of fourteen panels for the current wing. As the wing is 1.5m long, the final number of aerodynamic panels in spanwise direction is set to fifteen to obtain panels with round dimensions.

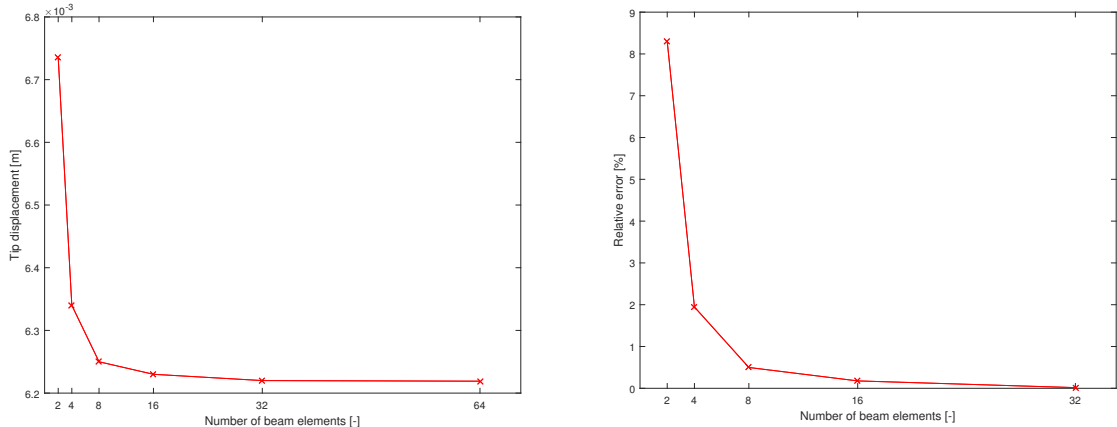


Figure 6.2: Convergence study results for number structural beam elements

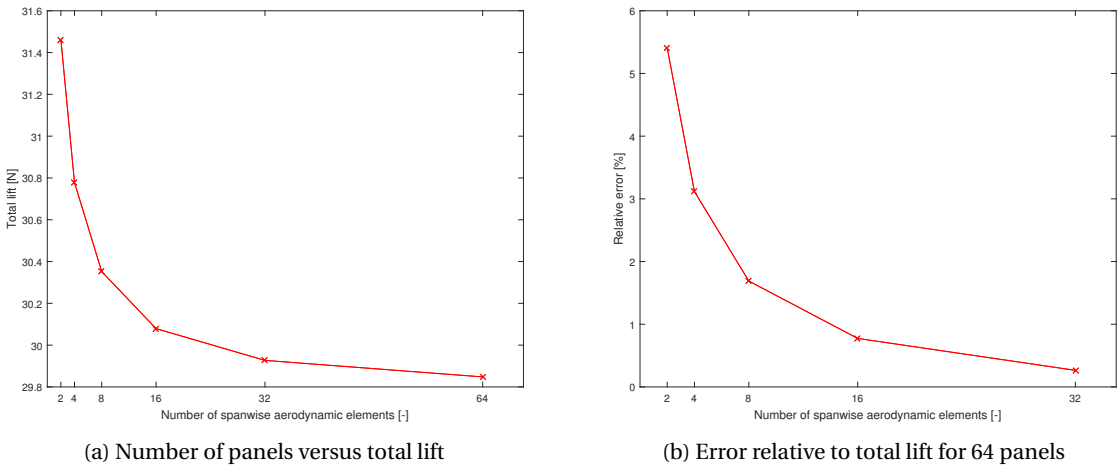


Figure 6.3: Convergence study results for number of aerodynamic panels in spanwise direction

Thirdly, the amount of aerodynamic panels in chordwise direction is determined. As a rule of thumb surface discretization methods in FE and aerodynamic analyses usually aim for realizing approximately square panels. For fifteen spanwise panels with a length of 0.1m this rule implies that the current chord length of 0.155m could accommodate a maximum of two panels.

It was found that the number of panels in this chordwise direction has a minor influence on the total lift that is generated, but that it has a significant influence on flutter velocity calculations. Figure 6.4 shows the flutter velocity result for different numbers of chordwise aerodynamic panels. It is evident that having only two aerodynamic panels in chordwise direction results in an unacceptable error of 100.0%. Increasing the number of panels to four, results in an error of 15% with respect to the flutter velocity obtained for a 64 panel case. Although eight panels result in a more reasonable error of 5%, the corresponding aspect ratio of the aerodynamic panels is 0.19, and thus far from square.

It was decided that if the aeroelastic stability constraint is active in the optimization procedure, a difference in the relative error of 10% between the four panel and eight panel case, is not very critical. To finalize the number of chordwise panels the tip deflections of the wing were therefore investigated for different numbers of panels. It was found that the effect of the number of panels on the wing twist θ_y is the largest, compared to the effect on the other deflections. Figure 6.5 shows the wing twist and the corresponding relative error to the wing tip twist computed for 32 panels in chordwise direction. The increase from four to eight panels only reduces the relative error by 0.20%, while significantly increasing computational time. It was therefore decided to use four aerodynamic panels for the analyses and optimizations that follow.

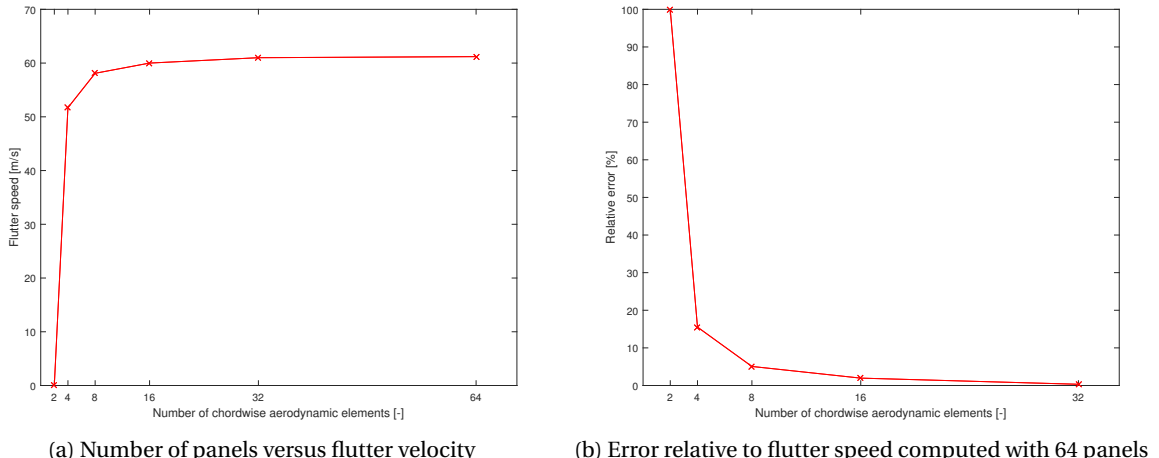


Figure 6.4: Convergence study results for number of aerodynamic panels in chordwise direction

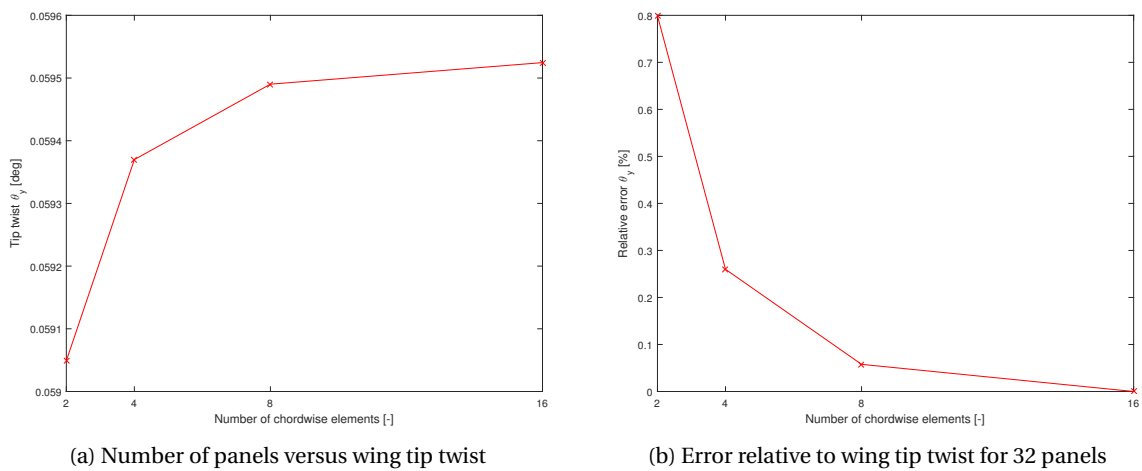


Figure 6.5: Convergence study wing twist results for number of aerodynamic panels in chordwise direction

6.3.3. Discretization of aerodynamic wake

After researching the effect of wake length on potential downwash and drag evolving from that, the length of the aerodynamic wake was set to ten chord lengths, with two wake panels per chord. Since the number of wake panels only affects the drag induced due to lift over the wing, aeroelastic tailoring procedures with a minimum weight objective will not be affected by this setting.

It should be noted that for optimizations with a maximum range objective, the number of wake panels would however play an important role, especially since low induced drag is a paramount feature of SBWs.

6.3.4. Number of design regions

Proteus allows for the definition of a certain number of chordwise and spanwise design regions for which the laminate can be optimized with respect to their layup. For the present work five design regions were specified along the wingspan, summing up to a total of twenty separate laminates for top skin, bottom skin, and the two spars. As the strut is not the main subject of optimization, it links to a single design region only. As a result four extra laminates are added, leaving a total of 24 laminates for the full SBW assembly. The numbering of the different laminate regions is depicted in figure 6.6.

6.4. Design constraints

Proteus allows for taking into account buckling, strain, aeroelastic stability, and lamination parameter constraints for design optimization. These latter constraints deserve some further explanation, as they are found to be of importance later on in this research.

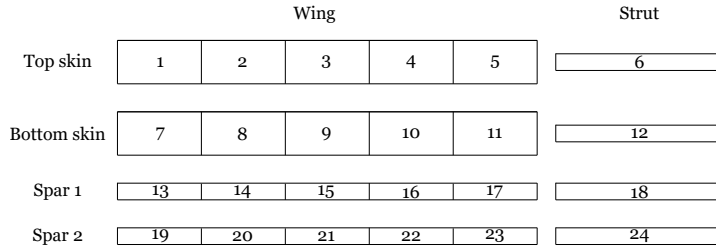


Figure 6.6: Numbering of laminate regions for SBWs under study

In Proteus laminates are described by lamination parameters instead of ply angles because of the advantages mentioned by Werter and De Breuker (2015). To ensure that the final combinations of lamination parameters correspond to designs that can be realized by physical layups, the set of feasibility constraints by equations 6.3 is defined (Hammer et al., 1997).

$$2(\xi_1)^2(1-\xi_2) + 2(\xi_3)^2(1-\xi_2) + (\xi_2)^2 + (\xi_4)^2 - 4\xi_1\xi_3\xi_4 \leq 1 \quad (6.3a)$$

$$(\xi_1)^2 + (\xi_3)^2 \leq 1 \quad (6.3b)$$

$$-1 \leq \xi_i \leq 1 \quad (6.3c)$$

These feasibility constraints apply to in-plane and out-of-plane lamination parameters. When aiming for a symmetric layup these constraints will thus only affect matrices **A** and **D** of the constitutive relations of the laminates considered (Kassapoglou, 2010).

For a symmetric laminate in Proteus, the application of these constraints will boil down to five laminate feasibility constraints, as listed below. Here, G5 defines feasibility design space with respect to the combination of in-plane and out-of-plane stiffness terms. Closed forms for the description of feasible regions for such combinations are not known, but can be approximated as is done in Proteus. As the details of this approximation are not relevant for the remaining of this work, references are made to Setoodeh et al. (2006) and Diaconu et al. (2002), who discuss different methods for approximation of feasible design regions for coupled cases.

- G1: equation 6.3a for **A**-matrix
- G2: equation 6.3b for **A**-matrix
- G3: equation 6.3a for **D**-matrix
- G4: equation 6.3b for **D**-matrix
- G5: feasibility constraint for combination **A**-matrix and **D**-matrix

6.5. Load cases

Before running any analysis or optimization, the enforced load cases need to be defined. The load case definitions are based on standard aeroelastic practice and potential testing conditions that will apply in future experiments, as will be explained in the following.

Manoeuvre loads of $+2.5g$ and $-1g$ are the load cases that are generally used in aeroelastic research, as they are found to be governing over all other possible load cases for QI wings. It is therefore intended that current thesis work will also be based on SBW optimization for these two load cases. However, since the SBW configuration under study does not include any aircraft or fuel weight data, but is rather a simple wing model, the load cases have to be quantified and introduced in a different manner.

Table 6.3: Boeing SUGAR reference data for load case calculation

Property	Magnitude
MTOW [N]	667460
Wing area S [m^2]	137.23
Cruise Mach number [-]	0.7
Cruise altitude [m]	11491

This is achieved by relating the +2.5g and -1g loads to the angle of attack. Usually, this is done by finding the trimmed angle of attack for an aircraft configuration. Again, since no aircraft weight data is available a different approach needs to be followed. With this in mind the +1g wing loading of the Boeing SUGAR reference project is reviewed, from which in combination with the wing area of the SBW under study the theoretical aircraft weight of this configuration is derived.

Table 6.3 lists the Boeing SUGAR data that is used for this derivation. A +1g wing loading of the SUGAR aircraft is calculated with equation 6.4. Relating this by means of equation 6.6 to the wing area of the present SBW model as obtained by equation 6.5, yields the theoretical MTOW.

$$\left(\frac{W}{S}\right)_{SUGAR} = \frac{667460}{137.32} = 4863.8 N/m^2 \quad (6.4)$$

$$S_{SBW} = 2b \cdot c = 3 \cdot 0.155 = 0.465 m^2 \quad (6.5)$$

$$W_{SBW} = \left(\frac{W}{S}\right)_{SUGAR} \cdot S_{SBW} = 4863.8 \cdot 0.465 = 2261.7 N \quad (6.6)$$

It is assumed that the aircraft is flying in cruise condition, which allows for the expression in equation 6.7 to be applied. Before this expression can be used to derive the angle of attack that corresponds to a +1g wing loading, the cruise speeds of the SUGAR aircraft and that for the SBW needs to be calculated.

$$L = W \quad (6.7)$$

$$TAS = M \cdot a = 0.7 \cdot 295.07 = 206.55 m/s \quad (6.8)$$

$$EAS = TAS \cdot \sqrt{\frac{\rho}{\rho_0}} = 206.55 \cdot \sqrt{\frac{0.342}{1.225}} = 109.08 m/s \quad (6.9)$$

At the given cruise altitude the speed of sound a is equal to 297.07 m/s. From equation 6.8 the true airspeed is calculated and subsequently the equivalent airspeed is derived from equation 6.9. To satisfy the expression in equation 6.7, the angle of attack of the SBW model is varied using the velocity from 6.9 until a total lift equal to 2261.7N is obtained. By feeding different angles of attack into the Proteus analysis function it was found that for an angle of attack of 3.5° the total lift is equal to 2235N, and that an angle of attack of 4.0° yields a total lift is equal to 2557N.

These angles of attack are small enough to show a linear relation with the total lift and therefore allow for linear interpolation to obtain the value that corresponds to the lift obtained in equation 6.6. The resulting angle of attack is shown in table 6.4. As lift and angle of attack are linearly related, the relation between the wing loading and the angle of attack is also linear, and the angle of attack for the +2.5g and -1g load cases can thus simply be derived. The final results are also listed in table 6.4.

Table 6.4: Load case input data

LC	Load [g]	Angle of attack [°]
[-]	+1	3.54
1	+2.5	8.85
2	-1	-3.54

Any fuel loads, non-structural masses or other external forces are discarded from the analysis. The maximum operating speed of the Open Jet Facility (OJF) at TU Delft is 25 m/s, corresponding to a Mach number of $M = 0.1$ by approximation. For the intended SBW model these velocities will thus be applied as well.

6.6. Configuration parameter studies

The SBW configurations that will be considered in this thesis work, can vary in spanwise (y_{strut}) and chordwise location (x_{strut}) of the strut-wing connection, vertical location (z_{strut}) of strut-fuselage connection and the axial stiffness of the strut (EA_{strut}). Since these variations cannot be without bounds because of the available computational capacity, a selection of the most interesting ranges for each of the parameters needs to be made.

To find a range that will give most insight for each parameter, the influence of the parameters on the behavior of the SBW is examined in a parameter study. The geometry, modeling parameters and load cases as discussed in the previous sections are applied to obtain aeroelastic analysis data on a large number of different SBW configurations. The parameter study makes use of SBW configuration parameters that range according to table 6.5.

To simplify the nomenclature for the remainder of this thesis, the span of a single wing will be indicated with b instead of the conventional $\frac{b}{2}$.

Table 6.5: Ranges for SBW configuration parameter study

SBW configuration parameter		Range entries	Unit
Chordwise location of strut-wing connection	x_{strut}	0.25, 0.50, 0.75	c
Spanwise location of strut-wing connection	y_{strut}	0.20, 0.40, 0.60, 0.80	b
Vertical location of strut-fuselage connection	z_{strut}	-0.15, -0.20, -0.25	m
Axial stiffness of strut	EA_{strut}	1.2, 20, 400, 800	kN

The ranges for x_{strut} and y_{strut} were chosen such that they provide an equal distribution of data points over their full span of interest. From literature it is known that having $y_{strut} > 0.80b$ significantly decreases the benefits of the SBW. For this reason $y_{strut} = 0.80b$ is the upper boundary for spanwise configuration data points. The maximum value of z_{strut} is based on the strut dihedral angle that is applied in the Boeing SUGAR TBW, which is equal to 15° for a strut-wing connection at 57% of the span. Applying these values to the model SBW, a maximum vertical distance of 0.25 m can be achieved.

6.6.1. Influence on aeroelastic behavior

First of all the static aeroelastic deformations are reviewed for the influence of configuration parameters. The complete set of results of this parameter study is given in appendix B, but figure 6.7 exhibits the most important conclusions that can be drawn from the results on wing tip deflection δ_z .

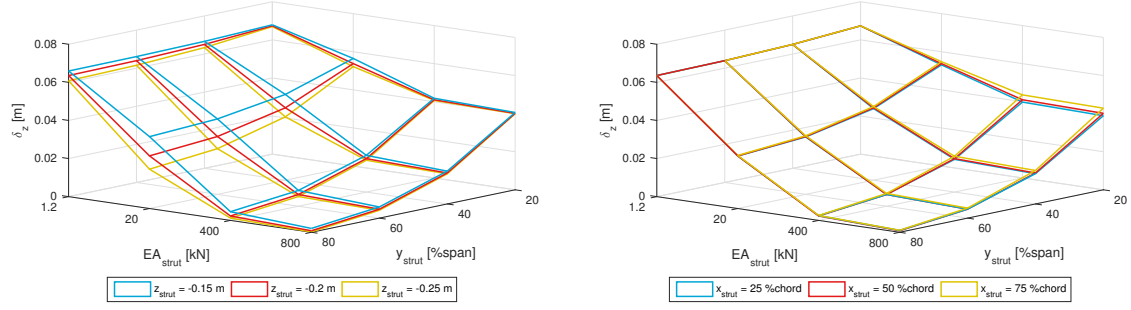
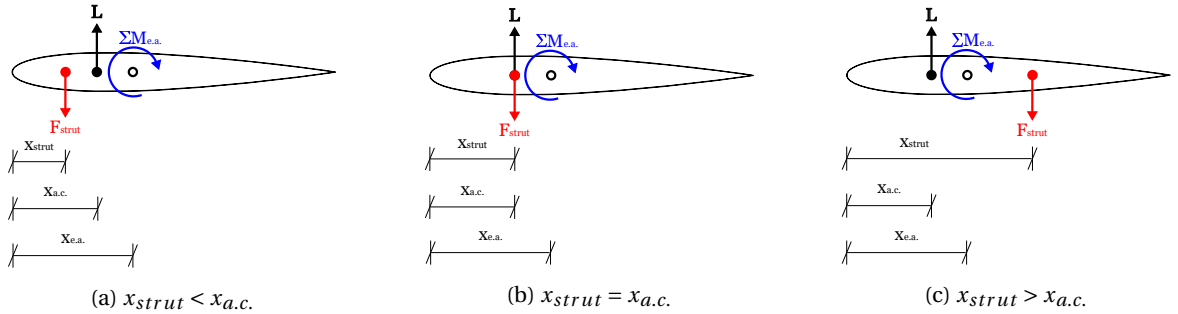
As can be seen in figure 6.7a, both EA_{strut} and y_{strut} clearly have the largest influence on the vertical aeroelastic deflection, and also that this influence is very intuitive. The more y_{strut} is located near the wing tip, and the stiffer the strut is in its axial direction, the smaller the static aeroelastic deflection.

z_{strut} has the largest effect on the vertical aeroelastic deflection for the second lowest value of strut stiffness only, while 6.7b shows that the chordwise strut position x_{strut} has little impact on δ_z . Furthermore, it is apparent that for the lowest strut stiffness, the other parameters do not seem to influence the static response very much. In appendix B, figure 6.7a and figure 6.7b are also plotted for different values of x_{strut} and z_{strut} . However, these figures indicate the exact same trends as discussed here.

When reviewing the static wing twist results in figure 6.9b, it is clear that x_{strut} does have a significant effect. The larger x_{strut} , the larger the wing twist θ_y at the tip. This can be explained by examining a cross-section of the wing at the location of the wing-strut attachment. Figure 6.8 illustrates how varying locations of x_{strut} may influence the aerodynamic pitching moment that locally acts on the wing section. Assuming the lift force acts in upward direction, tension in the strut will cause a downward tension force.

In this simple representation, the sum of moments around the elastic axis of the wing at $x_{e.a.}$ is generally defined by equation 6.10.

$$\Sigma M_{ref} = L \cdot (x_{e.a.} - x_{a.c.}) - F_{strut} \cdot (x_{e.a.} - x_{strut}) \quad (6.10)$$

Figure 6.7: Parameter study results on vertical wing tip deflection δ_z Figure 6.8: Moment around aerodynamic center for different locations of x_{strut}

Now, if $x_{strut} < x_{e.a.}$ as is the case in figure 6.8a and figure 6.8b, F_{strut} will generate a moment opposite in direction from the aerodynamic pitching moment that is generated by lift L around the reference point. As a result $\Sigma M_{e.a.}$ decreases with respect to the clean wing case, and the airfoil will twist to a smaller extent. In figure 6.8a $x_{strut} < x_{a.c.}$, causing F_{strut} to have a larger proportional contribution to $\Sigma M_{e.a.}$ than L , which can—depending on the stiffness of the strut—even result in a negative $\Sigma M_{e.a.}$, and consequently a negative rotation around its reference axis with respect to its initial position.

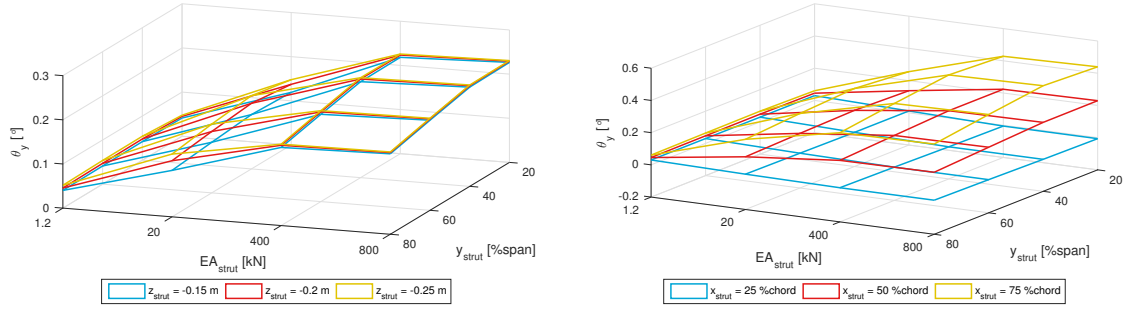
If x_{strut} moves behind the aerodynamic center, its negative contribution to $\Sigma M_{e.a.}$ decreases proportionally, resulting in an increase of the sum of moments relative to the case in figure 6.8a. When x_{strut} moves aft such that $x_{strut} > x_{e.a.}$, the contribution of F_{strut} to $\Sigma M_{e.a.}$ becomes positive and increases as x_{strut} moves towards the leading edge. Because of this increase pitching moment, the airfoil will twist around its elastic axis to a higher degree.

From these observations it can be concluded that x_{strut} has a significant effect on the aeroelastic behavior of the SBW configuration, and is therefore a very interesting parameter to further investigate with aeroelastic tailoring.

Figure 6.9a shows that z_{strut} only affects wing twist θ_y to a small extent, which is again most significant for $EA_{strut} = 10 \text{ kN}$. Compared to its effect on the vertical deflection δ_z , y_{strut} only affects the wing twist results by a modest rate. The trend of the effect is however clearly visible.

Finally, to get an idea of the influence of the different configuration parameters on the stability of the SBW, the results for the real part of the most critical eigenvalues λ of the aeroelastic system are plotted in figure 6.10. A negative value of $Re(\lambda)$ indicates aeroelastic stability. On that account it may be evident that the SBW configurations under analysis are stable but experience quite low damping at the applied airspeed, as the values for $Re(\lambda)$ are only slightly negative.

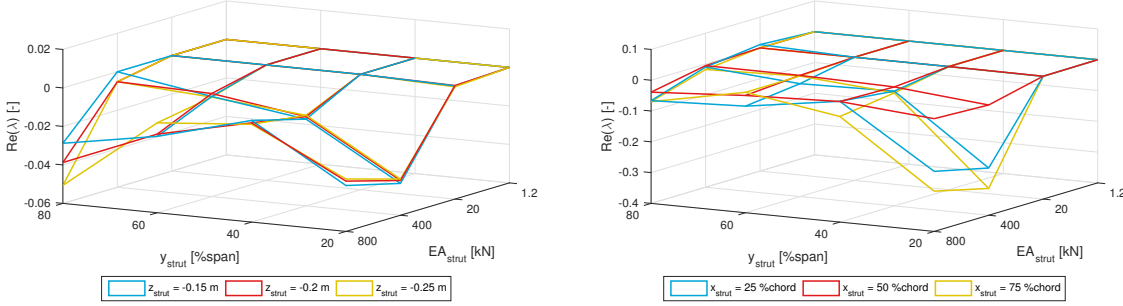
Possible causes for this low damping were already mentioned in section 2.1 and 2.2. The flexibility due to extreme wing slenderness plays an important role for aeroelastic stability of high-aspect ratio wings. Patil et al. (1999) mention that this type of aeroelastic behavior is strongly related to the distribution of modal frequencies relative to each other and the shape of corresponding modes. These will be examined and reviewed



(a) Wing tip twist θ_y for variable y_{strut} , z_{strut} and EA_{strut} , and $x_{strut} = 0.50c$

(b) Wing tip twist θ_y for variable y_{strut} , x_{strut} and EA_{strut} , and $z_{strut} = -0.20m$

Figure 6.9: Parameter study results on wing tip twist θ_y



(a) $Re(\lambda)$ for variable y_{strut} , z_{strut} and EA_{strut} , and $x_{strut} = 0.50c$

(b) $Re(\lambda)$ for variable y_{strut} , x_{strut} and EA_{strut} , and $z_{strut} = -0.20m$

Figure 6.10: Parameter study results on real part of aeroelastic eigenvalue of the SBW configuration

more elaborately for high aspect ratio wings and SBW configurations in chapter 7.

From figure 6.10a it can be observed that the vertical position of the strut at the root z_{strut} only affects the eigenvalue for low values of strut stiffness and extreme values of y_{strut} . It is shown that for a high y_{strut} an absolute larger z_{strut} results in a more stable configuration, while at the lowest y_{strut} a reversed effect occurs.

Figure 6.10b shows that the chordwise position x_{strut} only has a considerable influence on $Re(\lambda)$ for high values of EA_{strut} and low values of y_{strut} . Spanwise location of the strut y_{strut} and its stiffness EA_{strut} are evidently most dominant in determining the dynamic behavior of the SBW, but this effect also heavily depends on the specific settings of the other configuration parameters due to the generally high susceptibility of SBWs to flutter.

6.6.2. Determination of design parameters

It was already stated that $y_{strut} = 0.8b$ is the upper boundary for ranging the spanwise strut location, and that $z_{strut} = -0.25m$ is the maximum for the vertical location of the strut root. However, since only limited computational power is available for the final aeroelastic tailoring study, the most interesting configuration parameters and their corresponding ranges need to be determined.

$$\Delta_{average} = \sum_{i=1}^N \left(\frac{|h_0 - h_1|}{|h_0|} \cdot 100\% \right) \cdot \frac{1}{N} \quad (6.11)$$

Next to the qualitative assessment laid out in section 6.6.1, a quantitative study is presented in figure 6.11 to 6.14. These figures show the influence of each configuration parameter $h = \{x_{strut}, y_{strut}, z_{strut}, EA_{strut}\}$ separately, by displaying the variation of h on the x-axis, and the aeroelastic results for all possible configurations depending on the other parameters on the y-axis. Assuming each h has a range $[0, 1]$, the absolute

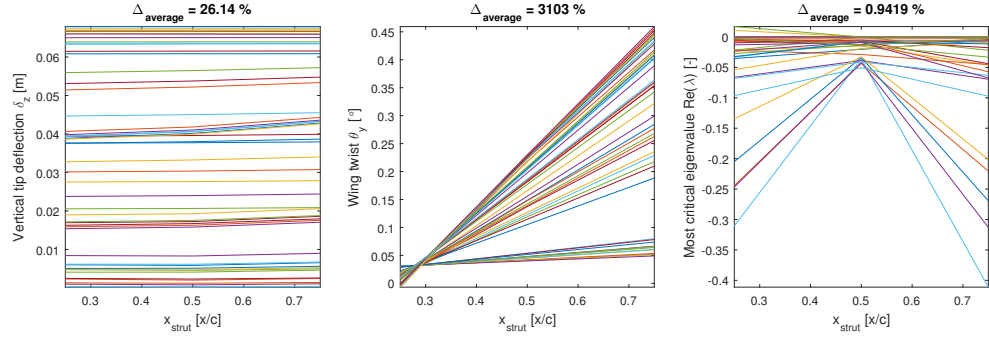


Figure 6.11: Aeroelastic behavior over range of chordwise locations of strut-wing connection for all possible configurations

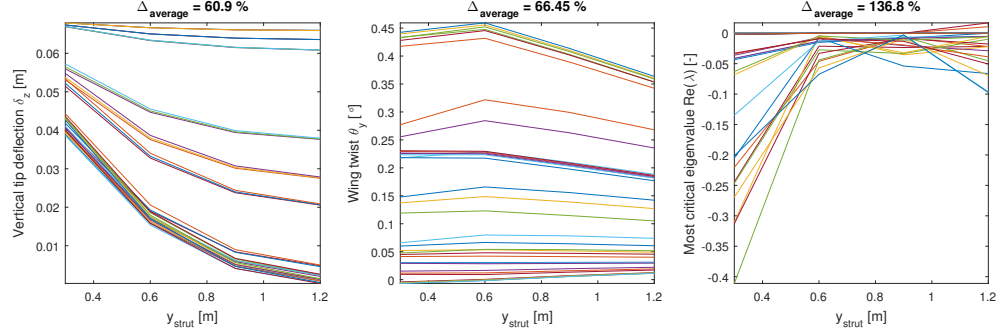


Figure 6.12: Aeroelastic behavior over range of spanwise locations of strut-wing connection for all possible configurations

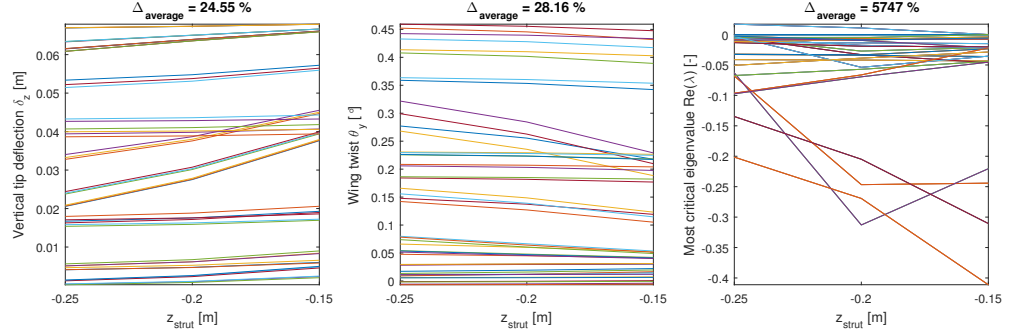


Figure 6.13: Aeroelastic behavior over range of vertical locations of strut-fuselage connection for all possible configurations

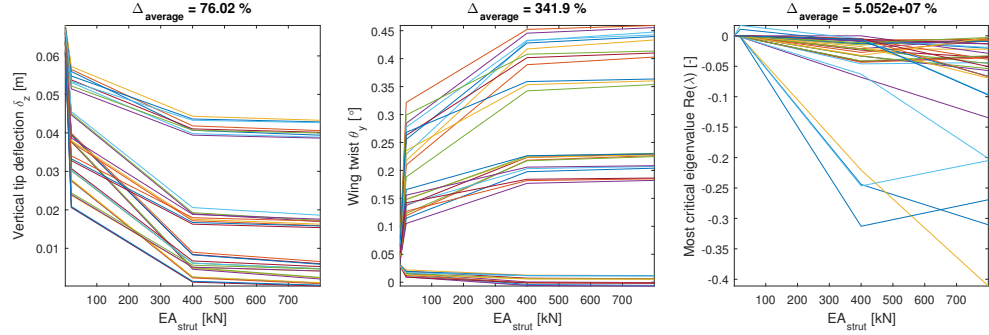


Figure 6.14: Aeroelastic behavior over range of strut axial stiffness values for all possible configurations

average difference Δ_{average} between h_0 and h_1 is defined by equation 6.11, where i varies from 1 to the total number of configurations involved N . The average difference values give an indication of the extent with which parameter h influences the aeroelastic behavior of all possible configurations over the full range of that

parameter h .

The figures show that trends for δ_z and θ_y are relatively stable compared to how $Re(\lambda)$ is influenced by each parameter. Both figure 6.7 and 6.9 already showed the evident influence that configuration parameters EA_{strut} and y_{strut} have on the static aeroelastic behavior of the SBW, and this is confirmed by figure 6.12 and figure 6.14, respectively, and by the average relative error values that they show. Therefore it is decided to take both parameters into account for the optimization study.

Figures 6.7 and 6.9 also show that the results converge to a certain value as strut stiffness increases, and that any $EA_{strut} > 500\text{kN}$ does not affect the deformation to a much larger extent than $EA_{strut} = 500\text{kN}$ does. Therefore, this will be the upper limit for this variable range. The lower limit is determined by the lowest value of axial stiffness contribution EA_{strut} that can be achieved in terms of minimum cross-sectional dimensions and material properties and is set equal to 10kN .

For y_{strut} the range as examined in the previous studies shows clear influence and relevance for further investigation. Hence, y_{strut} will be varied over the same range for the optimization studies as is done here.

Section 6.6.1 pointed out that z_{strut} only has a small influence on the aeroelastic behavior of the SBW, and only for specific combinations of the other parameter values. This can be explained by the fact that the examined range for z_{strut} was small to begin with. On the other hand, investigation of larger values of vertical distance is not relevant as was explained earlier. The average difference values in figure 6.13 confirm the small effect of z_{strut} on the aeroelastic behavior of the SBW, when compared to the differences over the parameter ranges in figure 6.11, 6.12, and 6.13. Therefore, it is decided to only investigate the maximum value, and fix the vertical location of the strut-fuselage connection to $z_{strut} = -0.25\text{m}$.

As the chordwise location of the strut-wing connection, x_{strut} , does have a serious influence on the wing twist, this parameter will be taken into account in detail as well. The range for this parameter includes the thickest point of the airfoil, being at 30%. To view beneficial effect of a strut in front of the aerodynamic center, $x_{strut} = 15\%$ is picked, while $x_{strut} = 50\%$ and $x_{strut} = 75\%$ can show the adverse effect of a strut connected towards the leading edge of the wing in two degrees.

6.6.3. Design parameter synthesis

The main conclusion to be drawn from the configuration parameter studies is that the vertical location of the strut-fuselage connection, z_{strut} , has a very minor influence on the static aeroelastic deformations of the SBW under study within its realistic bounds.

The configuration parameters that had the largest influence on the aeroelastic response of the investigated SBWs are listed in table 6.6. The 64 SBW configurations that can be defined by a possible combination of these parameters will be subjected to further analyses and used in the optimization studies in chapter 7.

Table 6.6: Optimization study configuration set

Configuration parameter	Analysis set	Unit
x_{strut}	15,30,50,75	%c
y_{strut}	20,40,60,80	%b
EA_{strut}	10,50,100,500	kN

6.7. Initial guess

The gradient-based optimizer in Proteus starts its optimization from an initial guess provided by the user. For physical relevance and applicability of the optimization result, the initial guess ideally is a feasible configuration with respect to all applied constraints.

Because the strut properties are predetermined and will remain constant to a certain extent throughout the optimization procedures, an initial guess only concerns the initial skin laminate orientation and thickness. The initial laminate is based on best practice in aeroelastic tailoring, while the thickness is ideally tuned such that no constraints are violated at the start of the optimization.

The extreme slenderness of the wing in the SBW configuration makes it however very susceptible to flutter and therefore all constraints need to be analyzed fully in order to find a feasible starting point for the optimization procedure.

A second issue in finding a feasible guess concerns the fact that there is a large number of SBW configurations to consider, of which each shows very divergent configuration properties. Due to rather large differences between one configuration and the next, no initial guess was found to be feasible for all 64 configurations from the optimization set.

As a starting point for the stiffness orientation a quasi-isotropic layup with specifications listed in table 6.7 was selected.

Table 6.7: Initial laminate specification

Fiber angle [°]	Thickness percentage [%]
±45	50
90	25
0	25

For the purpose of avoiding flutter, a smaller thickness appeared to be advantageous in general but in turn caused buckling and strain constraint violations. The corridor of feasible initial guesses between stability constraints and material failure showed to be extremely small. It was therefore decided to select an initial guess that would at least not violate buckling or strain constraints, while violating a minimum of stability constraints. The selected initial thickness distribution is summarized in table 6.8. These and all other settings discussed in this chapter are summarized in appendix A.

Table 6.8: Initial thickness distribution

Design region	1	2	3	4	5
t [mm]	2.0	1.75	1.5	1.25	1.0

6.8. Advanced sensitivity studies

As the full set of SBW configurations for optimization is rather large and the available computational power is limited, it might be worth it to reconsider the set of configurations prior to the optimization campaign.

The earlier discussed parameter study was aimed at finding the SBW configurations that would lead to the most valuable insights in the corresponding aeroelastic behavior. The most important conclusion was that z_{strut} would remain constant for the final configurations to be considered. Instead of performing 64 separate optimization procedures for all configurations that were defined in table 6.6, an advanced sensitivity study is performed on the untailored SBW configurations to see whether this design space, and in turn the required computational power can be reduced. Lift distribution, aeroelastic deflections, shear force distribution and root bending moment are reviewed for all configurations in order to find the configurations for which aeroelastic tailoring is expected to yield the best understanding of the application of this technique on SBWs.

6.8.1. Static aeroelastic deflection

The static deflection results of the tailored clean wing that will be discussed in section 7.1, will reveal the minor extent of static aeroelastic twist the wing model is experiencing. It appears that the initial wing design as presented in chapter 6 has a very high torsional stiffness, and it is suspected that the addition of a strut will not change this behavior to a large degree. In order to draw any conclusions on how the strut will influence aeroelastic behavior in this regard, the static aeroelastic deflections of the 64 untailored SBW configurations are reviewed.

Figure 6.15 shows the vertical deflections δ_z of 32 out of 64 untailored SBW configurations that came out of chapter 6. The set of figures shows a number of general trends regarding the influence of the configuration parameters on δ_z . Results for the configurations with $y_{strut} = 20, 80\%b$ are given in appendix C, and demonstrate the same trends.

Firstly, it is clear that the combination of any y_{strut} and the highest value of EA_{strut} have the largest influence on the vertical deflection of the wing. The strut configurations with the lowest EA_{strut} do not display much difference for increasing values of y_{strut} .

The second thing that may be clear is that the chordwise location of the strut-wing connection, x_{strut} , is only of minor influence on the vertical wing deflection. In section 6.6 it became apparent that x_{strut} does however have a significant influence on wing twist. In order to further investigate this influence on the 64 SBW configurations from the optimization study set, the wing twist results are given in figure 6.16.

As can be seen, the influence of x_{strut} on wing twist is in agreement with the earlier theory explained by figure 6.8. Regardless of the spanwise strut location, the effect is more profound for higher values of EA_{strut} . Since the physical principle of this effect is fairly clear, aeroelastic tailoring of the full set of SBW configurations with varying x_{strut} may not add any more insights of paramount importance, than those insights that would result from aeroelastic tailoring of a smaller selection of SBW configurations. To further investigate this assumption the influence on lift distribution is reviewed.

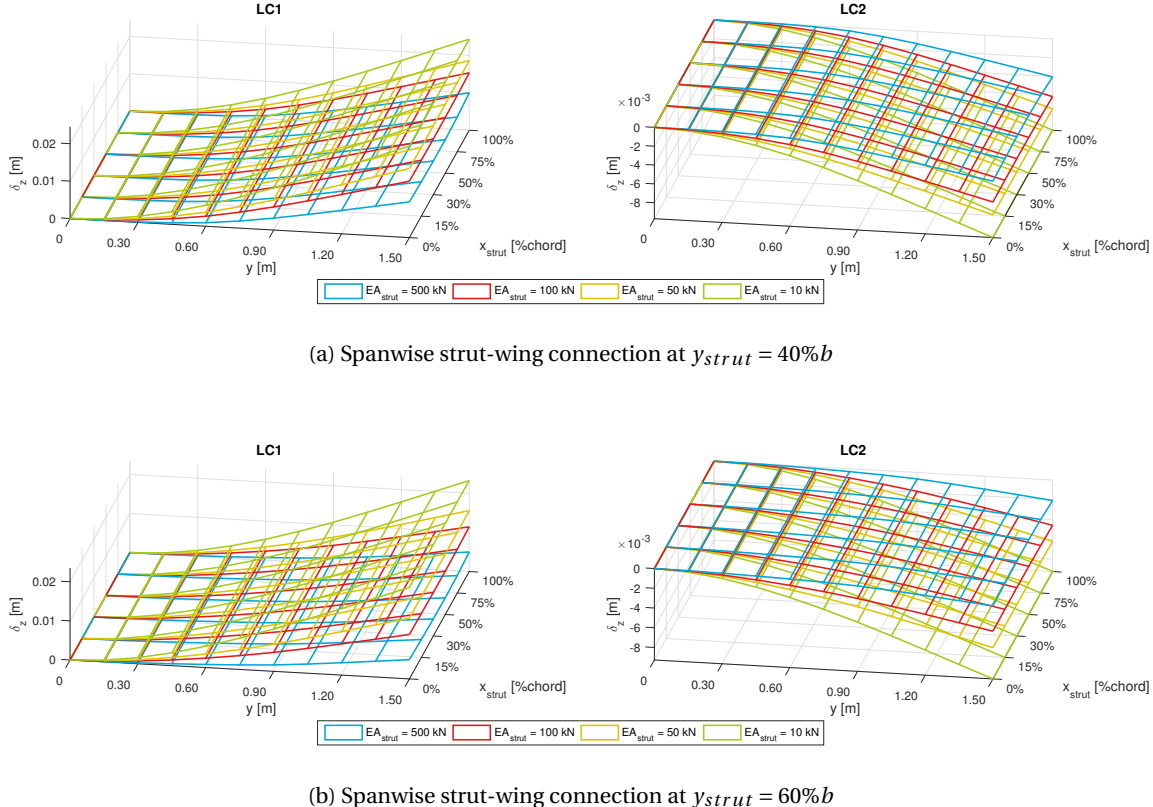


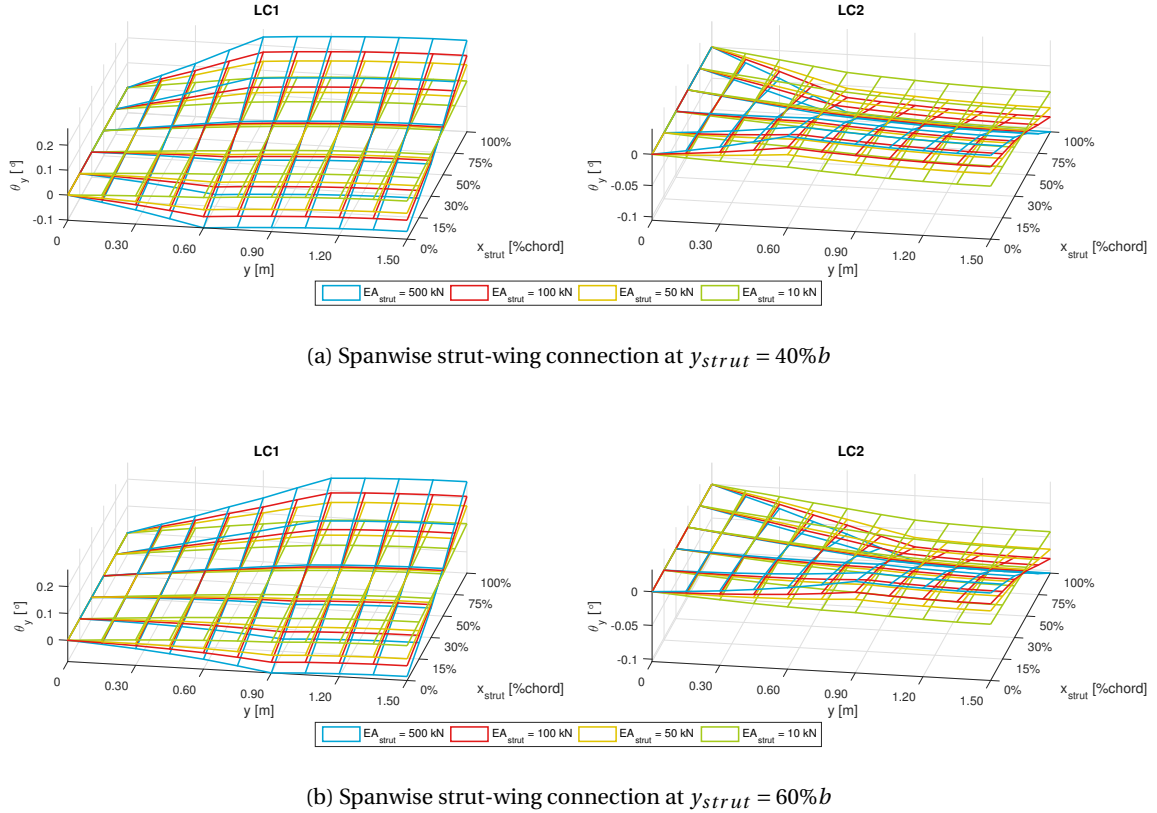
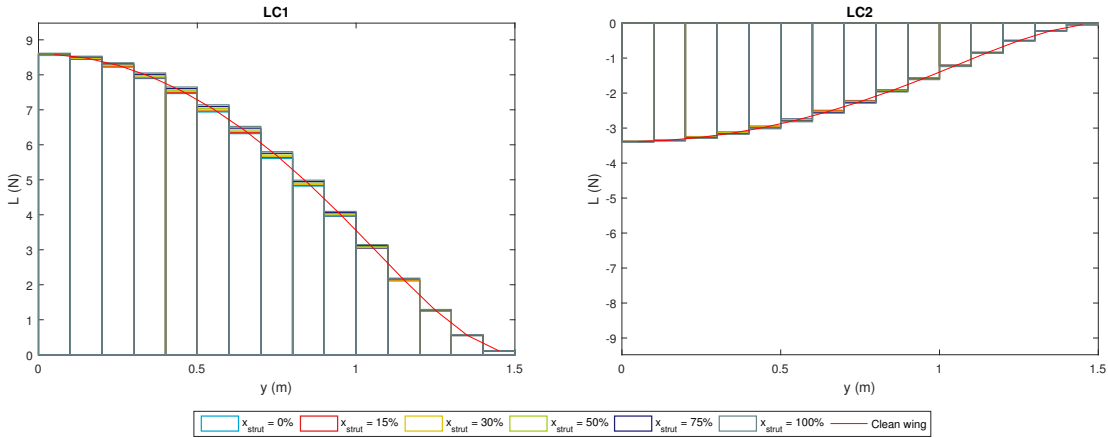
Figure 6.15: Vertical wing displacement δ_z for initial SBW designs

6.8.2. Lift distribution

It is believed that the largest differences in aeroelastic response, and thus in the eventual tailoring result will originate from differences in lift distribution. Therefore the lift distribution for varying values of x_{strut} is examined to verify whether omitting a selection from the x_{strut} analysis set that was specified in table 6.6 does not result in discarding paramount observations that could show contrasting behavior.

The largest variations in lift distribution are expected for that range of SBW configurations that show the largest differences in wing twist. Section 6.8.1 discussed that this correlates with strut members with a relatively high axial stiffness, such as $EA_{strut} = 500\text{ kN}$. Accordingly, the lift distribution for a set of configurations with $EA_{strut} = 500\text{ kN}$ is investigated. In figure 6.17 the lift distribution for four different, untailored SBW configurations with fixed y_{strut} and EA_{strut} is presented.

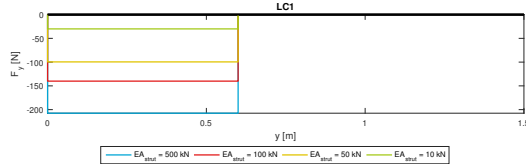
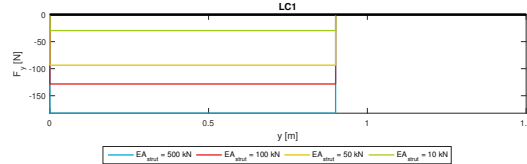
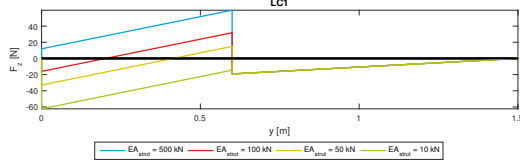
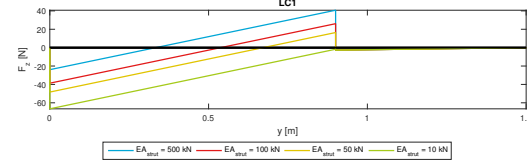
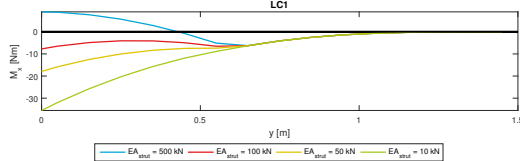
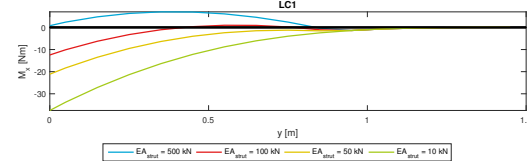
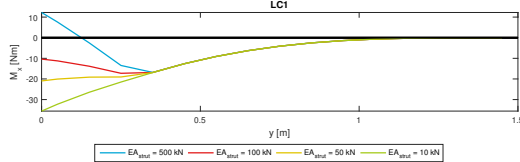
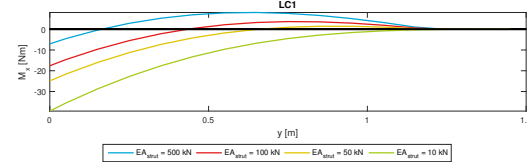
The figure displays a very small variation in lift distribution for the configurations that are considered. On that account it is safe to discard a subset of the 64 SBW configurations—associated with both variations in x_{strut} and low values of EA_{strut} —out the optimization studies.

Figure 6.16: Wing twist θ_y for initial SBW designsFigure 6.17: Lift distributions for four untailored SBW configurations with $EA_{strut} = 500\text{ kN}$ and $y_{strut} = 60\%b$

6.8.3. Shear force distribution and root bending moment

The next step in the advanced sensitivity studies is a review of the influence of the different SBW configurations on the normal force, shear force and moment distribution within the structure.

Figure 6.18 shows the how the axial force at the inboard part of the wing changes for variations in EA_{strut} for $y_{strut} = 40\%b$ and $y_{strut} = 60\%b$. For a higher axial stiffness of the strut, the tension force exerted on the wing by the strut member is larger. As a consequence the normal or axial force in the inboard part of the wing also increases with increasing EA_{strut} . When comparing the two cases for $y_{strut} = 40\%b$ and $y_{strut} = 60\%b$, it appears that smaller values of y_{strut} result in a higher normal force. This can evidently be explained by the

(a) Spanwise strut-wing connection at $y_{strut} = 40\%b$ (b) Spanwise strut-wing connection at $y_{strut} = 60\%b$ Figure 6.18: Normal force at inboard part of SBW with $x_{strut} = 30\%c$ and varying EA_{strut} for load case 1(a) Spanwise strut-wing connection at $y_{strut} = 40\%b$ (b) Spanwise strut-wing connection at $y_{strut} = 60\%b$ Figure 6.19: Shear force diagram SBW with $x_{strut} = 30\%c$ and varying EA_{strut} for load case 1(a) Spanwise strut-wing connection at $y_{strut} = 40\%b$ (b) Spanwise strut-wing connection at $y_{strut} = 60\%b$ Figure 6.20: Moment diagram SBW with $x_{strut} = 30\%c$ and varying EA_{strut} for load case 1(a) Spanwise strut-wing connection at $y_{strut} = 20\%b$ (b) Spanwise strut-wing connection at $y_{strut} = 80\%b$ Figure 6.21: Moment diagram SBW with $x_{strut} = 30\%c$ and varying EA_{strut} for load case 1

decreasing moment arm of the strut for approximately equal upward bending forces in the wing.

In figure 6.19 it is visible that the jump in vertical shear force is indeed larger for the $y_{strut} = 40\%b$ -case than for the $y_{strut} = 60\%b$ -case, as follows from the sum of bending moments around the x-axis of the wing.

The bending moment diagrams in figure 6.20 show how the sum of moments is distributed throughout the wingspan. The diagrams show the relieving effect of the strut on the root bending moment of the wing, which is essentially the most important feature of the SBW concept. The relieving effect increases for increasing axial stiffness of the strut, here controlled by EA_{strut} . The strut with the weakest axial stiffness, $EA_{strut} = 10\text{ kN}$ shows a bending moment that approaches the bending moment of the clean wing. At the same time a reversal of the moment direction is shown for the strut with $EA_{strut} = 500\text{ kN}$ with respect to the other values for axial strut stiffness. This positive bending moment at the root is caused by the large contribution the 500 kN strut provides.

The diagrams for the $y_{strut} = 20\%b$ and $y_{strut} = 80\%b$ cases in figure 6.21 expose no large deviations from the behavior depicted in figure 6.20. For $y_{strut} = 80\%b$ the contribution of the strut to counteract the bending moment caused by aerodynamic lift is allowed to be smaller than for the other cases, because of its larger moment arm with respect to the wing root. Consequently, the deviation of the current moment

distribution with respect to that of the clean wing is smaller and thus suggests that this test case will not yield any unpredictable tailoring behavior.

The SBW configurations in figure 6.21a show more or less the same moment distribution as figure 6.20a but with a sharper kink at the location of the strut-wing connection at $y = 20\%b$. For $y > y_{strut}$ M_x is approximately identical to that of the clean wing. Given these points, aeroelastic tailoring results on these configurations are not expected to show any additional insights that cannot be derived from the results on the SBWs with $y = 40\%b$ in combination with figure 6.21a. Therefore, it is decided that the configurations with $y = 20\%b$ could be discarded from the optimization set.

6.8.4. Synthesis

The sensitivities studies that were presented in the previous sections gave a better insight in what could be expected from the optimization studies that were planned. The small extent of twist, and the even smaller changes in lift distributions that these caused gave way to the decision of omitting a subset of the x_{strut} -configurations from the optimization studies that will follow.

The analysis of root bending moment and shear force distribution for the full set of SBW configurations suggests that aeroelastic tailoring of SBW configurations associated with $y_{strut} = 20\%b$ and $y_{strut} = 80\%b$ would not add any contrasting or unpredictable observations to the bulk of optimization results.

Therefore it was decided that the full set of SBW configurations that was specified in section 6.6.3 could be decreased to the following subset, without excluding any of the data points required for answering the research question. The final set of SBW configurations is then defined by table 6.9.

Table 6.9: Final set of SBW configuration for aeroelastic tailoring studies

	$EA_{strut}[kN]$	$x_{strut} = 15\%c$	$x_{strut} = 30\%c$	$x_{strut} = 50\%c$	$x_{strut} = 75\%c$
$y_{strut} = 40\%b$	500	x	x	x	x
	100	-	x	-	-
	50	-	x	-	-
	10	-	x	-	-
$y_{strut} = 60\%b$	500	-	x	-	-
	100	-	x	-	-
	50	-	x	-	-
	10	-	x	-	-

7

Aeroelastic tailoring results

This chapter will discuss the results of the optimization studies that were done. First, the optimization results of a clean wing will be discussed in order to create a valid reference point for later conclusions. This is then followed by the studies on SBWs.

7.1. Clean wing reference optimization

In order to identify any benefits of the best optimized SBW over the clean wing configuration, all optimization results need to be compared to an optimized clean wing design. The initial clean wing design that was subjected to aeroelastic tailoring for this purpose, holds the exact same geometric and material properties as the SBW configurations that are considered in this research, except for missing a strut member. The load cases and optimization objective that were used in the optimization are also identical to the settings discussed in chapter 6.

7.1.1. Tailored clean wing design

It was found that the initial guess based on these properties and settings was experiencing a dynamic aeroelastic instability at the start of the optimization procedure. As this was the only constraint that was actually being violated, the optimizer tailored the wing such that aeroelastic stability was achieved after the first two design iterations. From that point onward, the tailored wing design smoothly developed as is depicted by the fast and almost continuous convergence of the optimization objective shown in figure 7.1.

Figure 7.2 shows the result of the aeroelastic tailoring procedure. From left to right the skin thickness and laminate stiffness direction are shown for top and bottom skin, respectively. On the bottom row of figure 7.2 the same is done for the spars.

The thickness plots show that the overall thickness of the wing was significantly reduced, explaining the

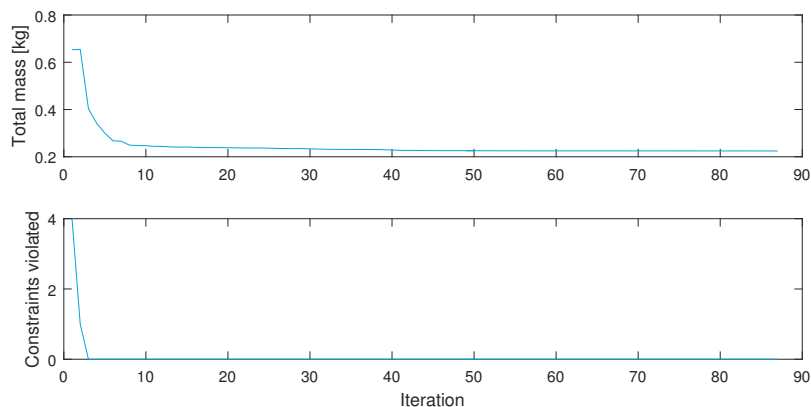


Figure 7.1: Clean wing optimization progress

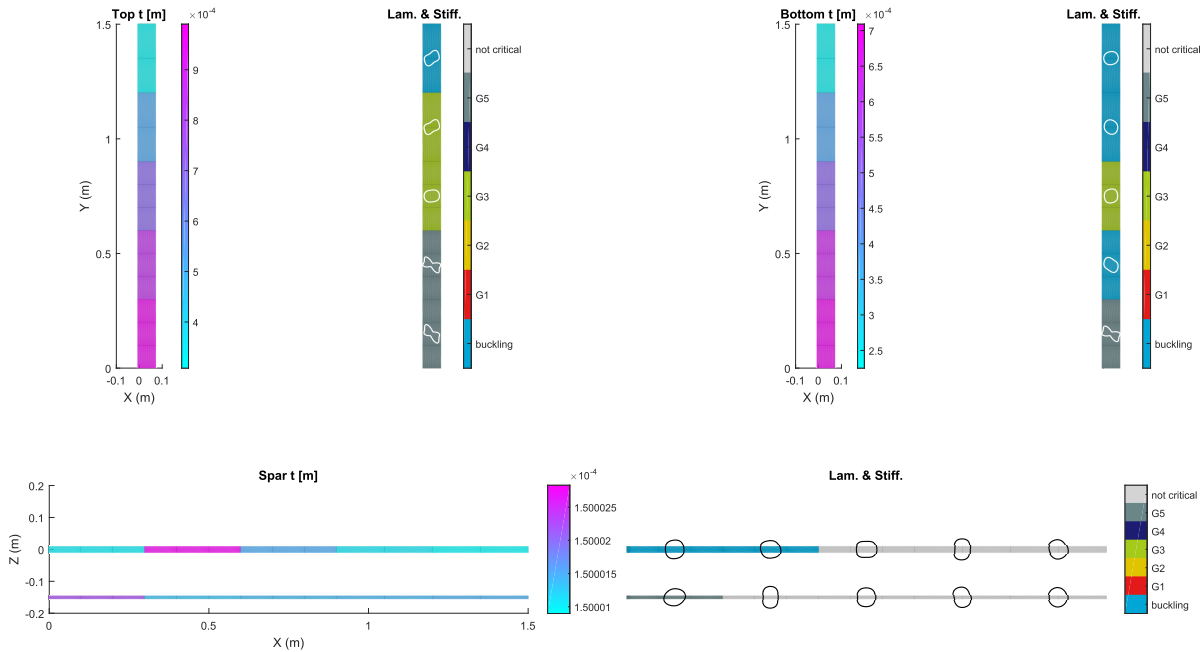


Figure 7.2: Thickness and directional stiffness of the optimized clean wing design

evident drop in total wing mass illustrated in figure 7.1. While the thickness decrease from wing root to tip in the top and bottom skin remained gradual, the optimized spar thickness became constant over the full length of the wing and equal to the lower thickness boundary that was set for the optimization.

The bottom skin enjoys a smaller thickness than the top skin, which can simply be explained by the fact that the negative wing load from LC2 is smaller in magnitude than the load from LC1, and thus results in the bottom skin to be less critical for buckling than the top skin.

As opposed to the thickness, the results for directional laminate stiffness initially seem less intuitive. The white colored polar plots in figure 7.2 represent the thickness-normalized modulus of elasticity that is obtained by equation 7.1 for each design region (Werter and De Breuker, 2015). By the inverse of the generalized constitutive laminate relations, the plotted stiffness is thus related to the A-matrix of the laminate only (Kassapoglou, 2010).

It should be noted that a quasi-isotropic laminate would be represented by a perfect circle as it has equal stiffness in all directions.

$$\hat{E}_{11}(\theta) = \frac{1}{\hat{a}_{11}} \quad (7.1)$$

The directional stiffness result shows bending-torsion coupling at the root and tip section of the top skin and at the root section of the bottom skin. Figure 7.3a illustrates how this specific result may influence any wing deformations caused by aerodynamic loading. For a positive load case the wing tip will in this case twist upward around the local stiffness axis, and thus create more lift. For the root section an opposite effect will occur. Given these points it is implied that the wing was optimized by creating a wash-out effect at the wing root and a wash-in effect at the tip. These effects are the respective inboard shift and outboard shift of lift forces and are related to the local wing twist.

For a typical wing, wing twist is ideally reduced towards the tip such that lift forces shift inboard, relieving the root bending moment, tip deflection and avoid wing tip stall. In the case of aeroelastic tailoring wash-in and wash-out effects induced by wing deformation such as twist and bending can be controlled by the proper selection of ply angles and distribution of laminate thickness (Hertz et al., 1981). Aeroelastic tailoring commonly addresses divergence issues and for that purpose introduces bend-twist coupling to produce wing wash-out at outboard sections of the wing, while the root section experiences wash-in or a lesser extent of wash-out (Werter and De Breuker, 2015). An example of such aeroelastic tailoring from Werter and De

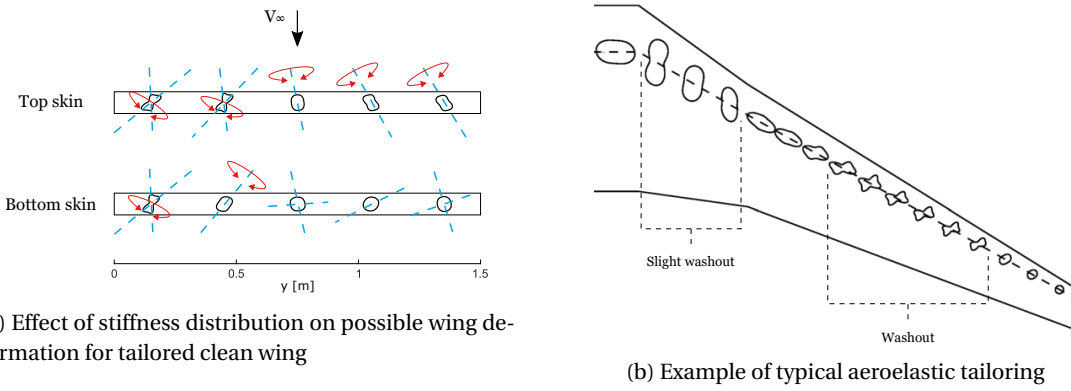


Figure 7.3: Examples of tailoring effect

Breuker (2015) is shown in figure 7.3b.

The tailored SBW design in figure 7.2 thus realizes the exact opposite of the example tailoring result. In order to explain this behavior, the static wing deformation is reviewed to be able to see how the static aeroelastic behavior of the current wing is influenced by the tailoring result. Furthermore, the constraints that were active over the course of design iterations are inspected to see what constraints were the key drivers in the design.

7.1.2. Static aeroelastic deformation

Figure 7.4 shows how the thickness and directional stiffness optimization influence the static aeroelastic deformation of the wing with respect to the initial design. There are two things that can immediately be observed. The first is that the vertical tip deflection of the tailored wing is almost three times larger than for the initial design as shown in figure 7.5, indicating that the initial design was over designed in terms of the deflection it allowed.

A second observation concerns the extremely small extent to which the wing is twisting around its y-axis. In order to see how tailoring influences the twist behavior of the wing, the quantified twist results are plotted in figure 7.5, for the initial design and tailored wing respectively.

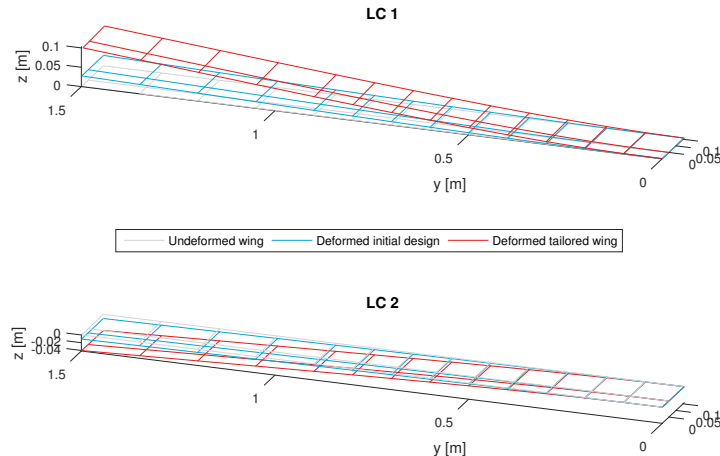


Figure 7.4: Comparison of static aeroelastic deformation of untailored and tailored clean wing

The extent of the effects of wash-out and wash-in are clearly visible. Tailoring for wash-out at the root indeed results in a negative twist for this section, albeit to a small extent. Figure 7.2 shows a transition in stiffness direction from the second to the third design region. This transition coincides with a change in slope of the wing twist angle at $y = 0.6m$ that is shown in figure 7.5. The wash-in effect that is introduced by the bending-torsion coupling in the two outer design regions is introducing a reduction in twist angle, as

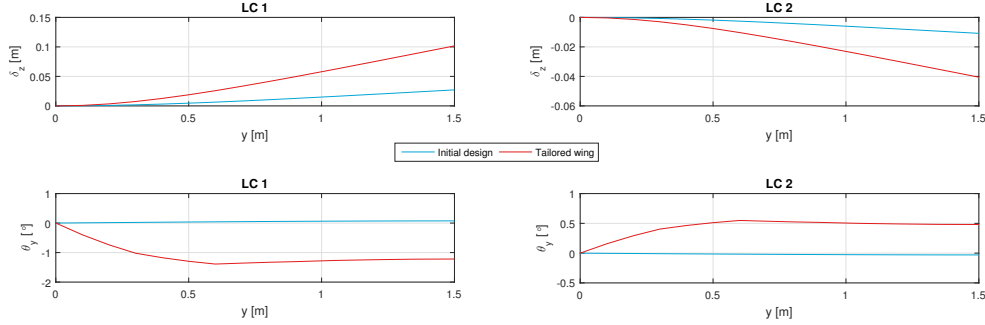


Figure 7.5: Comparison of static aeroelastic vertical deflection and twist of untailored and tailored wing

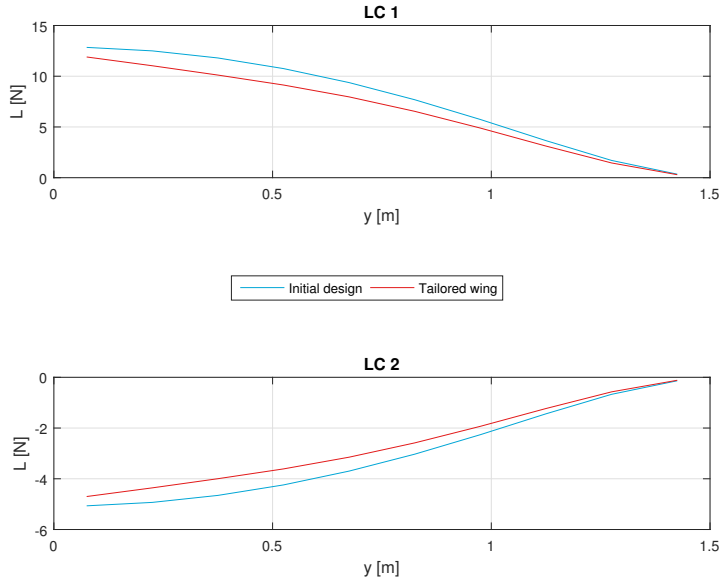


Figure 7.6: Comparison of lift distribution for untailored and tailored wing

is expected, but by a very small degree only. As a result the negative wing twist angle of $\theta_y = -1.3^\circ$ remains approximately constant for $0.6m < y < 1.5m$. Figure 7.6 shows the self-evident effect the tailoring result has on the lift distribution. The wash-out of lift at the root section is clearly visible when comparing the lift distribution for both load cases with those of the untailored clean wing.

It seems that there is thus an advantage for a negative twist angle, and a decrease in lift for a straight clean wing with a high aspect ratio ($AR = 19.4$). To get better insight in the key drivers in the optimization, the active design constraints are examined.

7.1.3. Active design constraints

From the constraint violation history of the optimization procedure, the list of most active constraints for the final design was retrieved. As the initial design had dynamic aeroelastic instabilities, it may be no surprise that aeroelastic constraints play an important role in the tailoring procedure.

The constraint that is most active for the converged optimization is Aeroelastic stability, LC...¹ with $-3.9041e-07$ and is followed by the constraints that are directly associated with the laminates that have been visualized in figure 7.2. The figure highlights that in addition to the active aeroelastic stability constraint, the final clean wing design is mostly constrained by buckling and laminate feasibility constraints. It was found that strain constraints were not active in any of the outer design iterations.

For conventional wings it would be rather unusual that laminate feasibility constraints play such a large role in aeroelastic tailoring. Figure 7.2 shows that the inner design regions are dominated by the G5 constraint, indicating the critical nature for the specific combination of A- and D-matrix terms in these lami-

nates. The third and fourth design region of the top skin and the third region of the bottom skin show G3 as the most active constraint, which is associated with the D-matrix as was explained in section 6.4.

Both the G3 and G5 constraints (partly) concern laminate feasibility with respect to the D-matrix. Figure 7.2 thus implies that the pure bending characteristics of the tailored clean wing laminates that are highlighted in green and dark green colors, are close to obstructing laminate feasibility. The minor static aeroelastic deflections are most likely not driving the laminates to develop such extreme characteristics. Therefore the most active stability constraint is investigated for its corresponding modal behavior.

Investigation of the critical aeroelastic eigenmode that corresponds to the aeroelastic stability constraint, shows that the wing is optimized for avoiding flutter instabilities in the first place. The three most critical eigenvalues are listed in table 7.1. Figure 7.7 is presenting the details of the most critical eigenmode.

Table 7.1: Most critical eigenvalues of clean wing

$Re(\lambda)$	$f[\text{Hz}]$
-3.90E-07	35.97
-0.0419	198.01
-0.2914	504.91

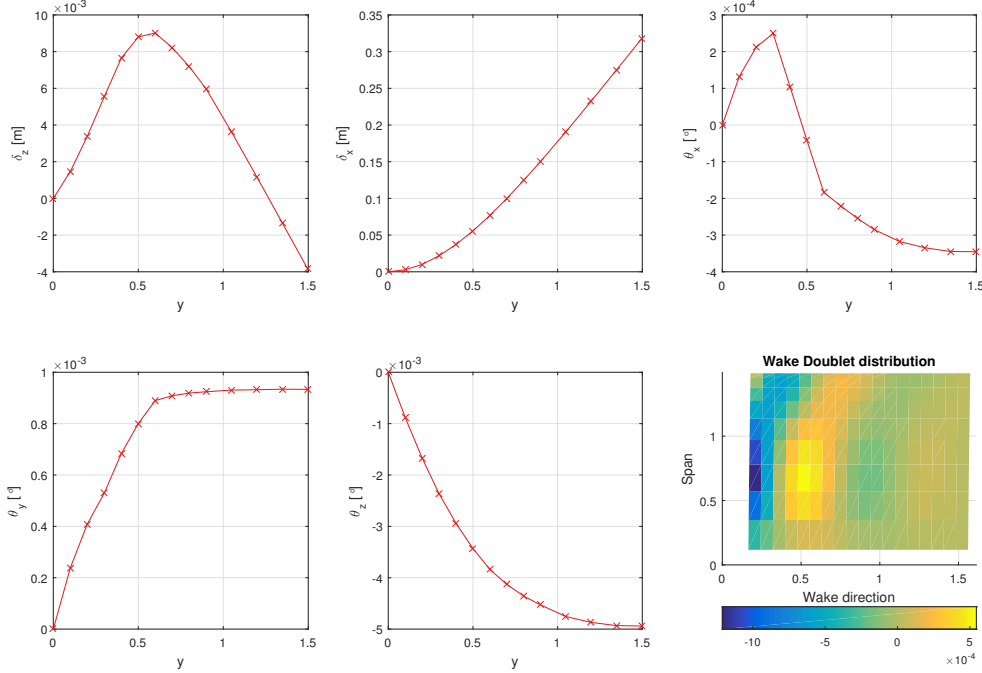


Figure 7.7: Characteristics of critical eigenmode for tailored clean wing

It can be observed that the critical mode concerns in-plane bending of the wing, which makes it identical to the second structural eigenmode. In spite of being very small in terms of magnitude, the vertical deflection and wing twist show a clear change at $y = 0.6\text{m}$, which is again coinciding with the transition from the second to the third design region and consequently the transition from the attained wash-out effect at the root to a QI laminate midspan, and wash-in effect towards the tip.

The visualization of the doublet strength in the wake of the wing confirms the flutter motion that is suggested by the complex eigenvalue. The fact that the wing is clearly not optimized to avoid divergence but for flutter instead, partly explains the wash-in tailoring effects near the tip of the wing. Weisshaar (1987) actually already discussed the presence of wash-in has a beneficial effect on flutter speeds and that the same effect causes a decrease in divergence speed. Georghiades and Banerjee (1997) shows how modal interchanges caused by changes in ply angles are responsible for the beneficial effect of wash-in on flutter speed.

From the earlier observations from figure 7.2 it can be concluded that next to active flutter constraints, the laminate feasibility constraint 6.3b for the D-matrix is most active for the middle section of the wing, while constraints on the combination of A- and D-matrix terms are most active for the first two design regions. The extreme susceptibility to flutter also explains this uncommon occurrence of the lamination parameter constraints as part of the the most active design drivers. Apparently, the design space for an aeroelastically stable wing with such high aspect ratio is very narrow. As a result the converged design hits boundaries associated with laminate feasibility instead of strain or buckling. Although for completely different wing and plate models, the studies of Kameyama and Fukunaga (2007) on aeroelastic tailoring for flutter constraints also present maximum flutter speed on the feasibility boundaries of the lamination parameters that concern the out-of-plane stiffness matrix \mathbf{D} . These results are not directly applicable to the current work, but do indicate that laminate feasibility boundaries do play an important role in aeroelastic tailoring for flutter instabilities.

7.2. SBW optimization results

Aeroelastic tailoring was conducted for all fourteen SBW configurations indicated in table 6.9. This section will present and discuss the results of these optimizations with the aim of completing the research objective as defined in chapter 1. Similar to the discussion in section 7.1, the thickness and stiffness of the tailored wings will first be reviewed, followed by the corresponding static aeroelastic deformations, and a discussion on the design constraints that were active during the different tailoring procedures.

In order to compare the results of the different configurations to each other, three subsets are specified from the total of fourteen. These subsets are:

- A) SBWs with fixed y_{strut} and x_{strut} , and varying EA_{strut}
- B) SBWs with fixed y_{strut} and EA_{strut} , and varying x_{strut}
- C) SBWs with fixed x_{strut} and varying y_{strut}

7.2.1. Thickness and directional stiffness results

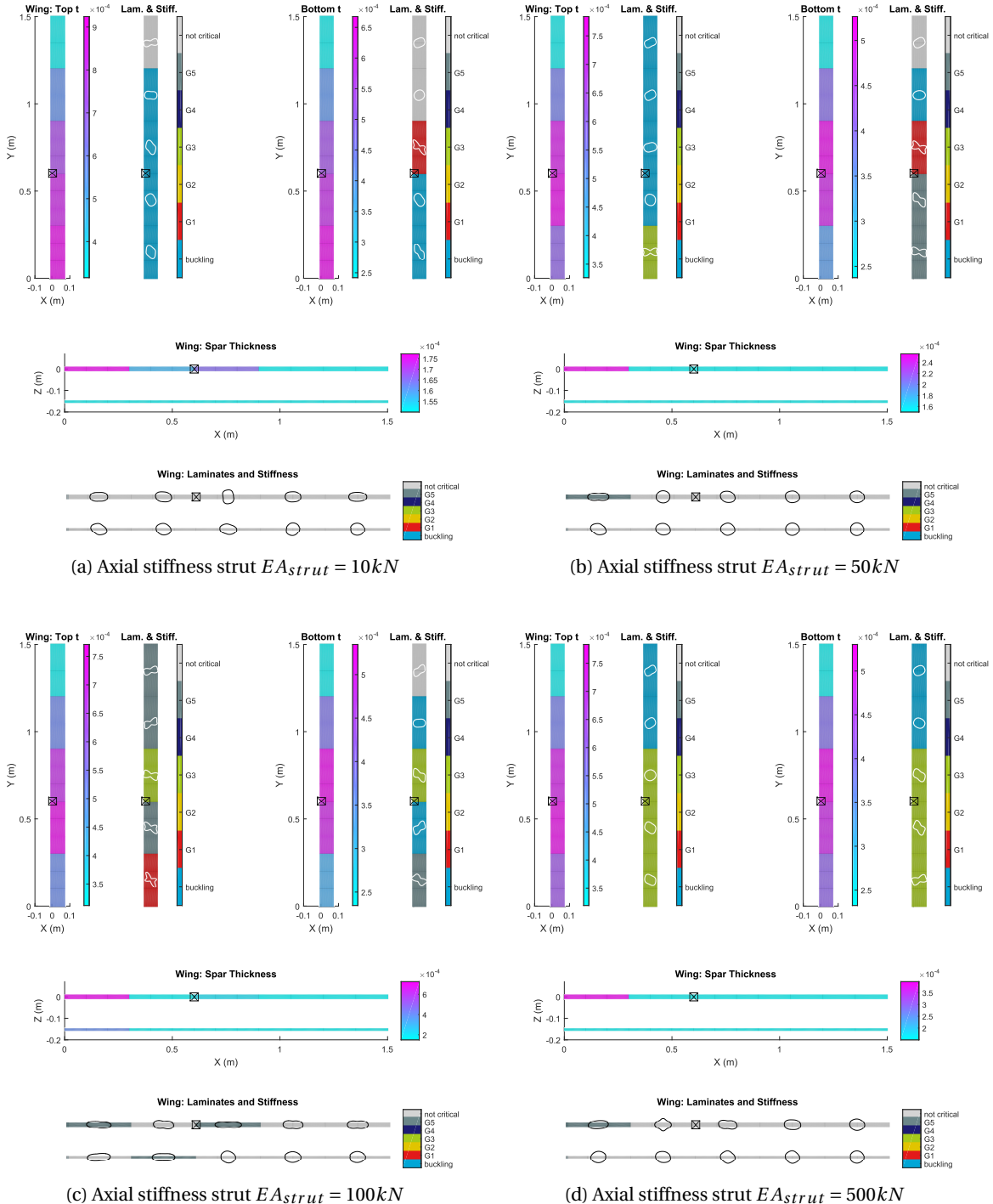
For each of the configurations within these three sets the thickness and directional stiffness results of the top and bottom skin and both spars are visualized in figures 7.8-7.11. The most active design constraints are also depicted in these figures, but will be discussed later on in section 7.2.3.

Subset A: $y_{strut} = 40\%b$, $x_{strut} = 30\%c$, with varying EA_{strut}

Figure 7.8 presents the thickness and stiffness plots for the first set of tailored SBW configurations. The location of the strut-wing connection is indicated with the boxed cross at $y = 0.6m$.

From comparison of the optimization results of the four SBW configurations in figure 7.8, a number of observations can be made with regard to the influence of the strut. Firstly, the optimized thickness reaches its maximum in proximity of the strut-wing connection for all configurations, except for the one in figure 7.8a with the weakest axial strut stiffness. This latter configuration shows a gradual thickness decrease from wing root to tip, while it also employs the largest maximum wing thickness of all four configurations presented in the figure. These results can be linked to figure 6.20a, that revealed that the bending moment distribution throughout the wing is almost not affected by the strut with the lowest axial stiffness ($EA_{strut} = 10kN$). Accordingly, the wing skins need more thickness to both carry the bending moment caused by the aerodynamic lift force acting on the wing and avoid skin buckling.

The other three configurations with higher values for EA_{strut} show little difference in thickness distribution with respect to each other. In contrast, the spar thickness does show significant differences from one tailored SBW to the other. The $EA_{strut} = 100kN$ case shows a maximum spar thickness that is almost twice that of the cases with $EA_{strut} = 50kN$ and $EA_{strut} = 500kN$. The distribution of thickness over the different laminate regions within the spars is however very similar for each of the four configurations. The first laminate region in the front spar is where the maximum thickness is applied, whereas the other regions in front and rear spar have an almost constant minimum thickness. The fact that the laminate in the first region of the front spar is much thicker than that of the rear spar, implies a wash-out effect at the inboard part of all four configurations, and thus confirms the effect that is related to the directional stiffness results of the top and bottom skins.

Figure 7.8: Tailoring results for SBW configurations with $x_{strut} = 30\%c$ and $y_{strut} = 40\%b$

The configurations with the largest maximum spar thickness also show the most profound stiffness tailoring, as can be seen in figure 7.8b and 7.8c. While the SBWs with $EA_{strut} = 50kN$ and $EA_{strut} = 500kN$ only have strong tailoring in the longitudinal direction in the first design region of the front spar, the $EA_{strut} = 100kN$ -case also shows stiffness with strong directionality in the second and third design region of the front spar and in the first two regions of the rear spar. The longitudinal direction of the tailored spar stiffnesses can be linked to the normal force that acts on the wing inboard of the strut, as was shown in figure 6.18.

The tailored stiffness of the top and bottom skins of this subset of SBWs also show some considerable

differences. One thing they do have in common is the occurrence of wash-out at the wing root and wash-in at the tip, similar to the tailored clean wing discussed in section 7.1, albeit to different extent.

The most pronounced stiffness tailoring is visible in the $EA_{strut} = 100kN$ -case in figure 7.8c, while the top skins of the SBW with $EA_{strut} = 50kN$ and $EA_{strut} = 500kN$ show the smallest relative degree of stiffness tailoring. The corresponding bottom skins however, do show more distinct tailoring of the stiffness direction. It is interesting to note that the first design region of these skins actually show less pronounced wash-out than the bottom skin of the $EA_{strut} = 100kN$ -SBW, and that the first region in the bottom skin of figure 7.8d actually shows a small degree of wash-in. Finally, the bottom skin of the SBW with $EA_{strut} = 100kN$ also demonstrates the alternation of wash-out and wash-in between design regions.

Figure D.1 in appendix D provides the same results for configurations with $y_{strut} = 60\%b$, $x_{strut} = 30\%c$ and varying EA_{strut} . These will be further discussed in comparison with the SBWs with $y_{strut} = 40\%b$ in section 7.2.1.

Subset B: $EA_{strut} = 500kN$, $y_{strut} = 40\%b$, with varying x_{strut}

The tailoring results of the second set of SBW optimizations are presented in figure 7.9. In each of the four subplots the location of the strut-wing connection is again indicated with a black mark.

The tailored thickness for these four test cases displays approximately the same results for top and bottom skins regarding maximum and minimum thickness, and the distribution of the thickness steps. The optimized spars do however display different thickness results for each of the configurations. The SBWs with $x_{strut} = 15 - 50\%c$ have constant spar thickness for all but the first front spar region, which holds the maximum thickness.

Distinct stiffness tailoring in the spars is less apparent for subset B than for subset A. The influence of EA_{strut} on this development was already discussed in section 7.2.1.

The $x_{strut} = 75\%c$ configuration employs the thinnest spars, and shows a more gradual spar thickness decrease towards the tip of the wing than the other configurations. Furthermore, this configuration is the only one in this set where the rear spar has a larger thickness near the root than the front spar. This implies the presence of a wash-in effect in the inboard region of the wing and actually contradicts the effects that are suggested by the tailored stiffness of the top and bottom skins of this SBW.

Similar to the results of the clean wing and those of the SBWs from subset A, the tailored stiffness results in the top skins do hint towards the presence of wash-out near the root and wash-in at the wing tip, and thus for flutter tailoring. Within the set of configurations in figure 7.9, the SBW with $x_{strut} = 30\%c$ displays the smallest degree of stiffness directionality, while the SBW with $x_{strut} = 50\%c$ employs the most directional stiffness.

For all four SBWs the inner design region of the bottom skin holds a significant smaller degree of wash-out than the other inboard regions, and the SBW with $x_{strut} = 30\%c$ even shows a small wash-in effect, as was already pointed out in section 7.2.1.

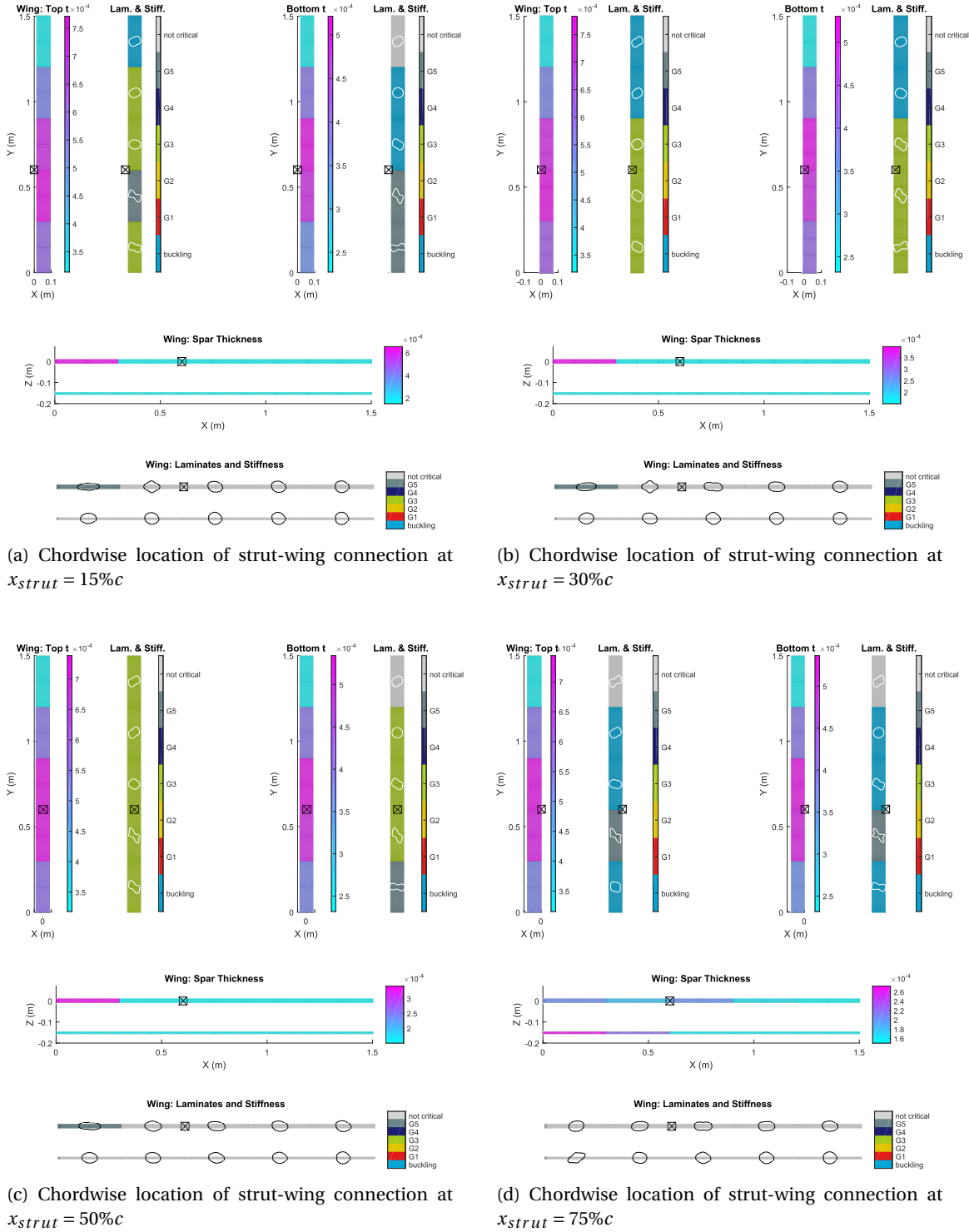
Appendix D gives the same figure for comparison of the effect of x_{strut} on the tailoring result for SBWs with $y_{strut} = 60\%b$. The top and bottom skin thickness and stiffness results are strongly comparable to the observations discussed here for the configurations with $y_{strut} = 40\%b$.

Subset C: $x_{strut} = 30\%c$, $EA_{strut} = 100kN$, with varying y_{strut}

Now the effects of x_{strut} and EA_{strut} on the aeroelastic tailoring results have been discussed for the SBWs with $y_{strut} = 40\%b$, a final comparison with the tailoring results on the SBWs with $y_{strut} = 60\%b$ needs to be done.

Figure 7.10 presents the tailoring results of two SBWs with both $x_{strut} = 30\%c$ and $EA_{strut} = 100kN$. Figure 7.10a shows the tailored design of the SBW with $y_{strut} = 40\%b$ and figure 7.10b presents the tailored $y_{strut} = 60\%b$ -SBW.

It is clear that although especially the top skin of the SBW in figure 7.10a shows the wash-out and wash-in effects that were discussed earlier, the SBW with $y_{strut} = 60\%b$ in figure 7.10b employs the same stiffness direction all over the top skin. The wash-in effect that is suggested by these results acts over the full wing, and implies that the SBW with $y_{strut} = 60\%b$ is more critical with respect to flutter than the SBW with $y_{strut} = 40\%b$. At the same time the tailored stiffness in the bottom skin seems to counteract this effect to

Figure 7.9: Tailoring results for SBW configurations with $EA_{strut} = 500kN$ and $y_{strut} = 40\%$

a large extent. Only the laminate region at the wing tip shows wash-in, similar to the top skin stiffness. The same observations can be made for the SBW configuration with $y_{strut} = 60\%b$ and $EA_{strut} = 50kN$, for which the tailoring results are presented in figure D.1b in appendix D.

Observations with respect to thickness distribution throughout the wing show the same mechanism for both SBW configurations. Maximum skin thickness is applied to the laminate regions that enclose the strut-

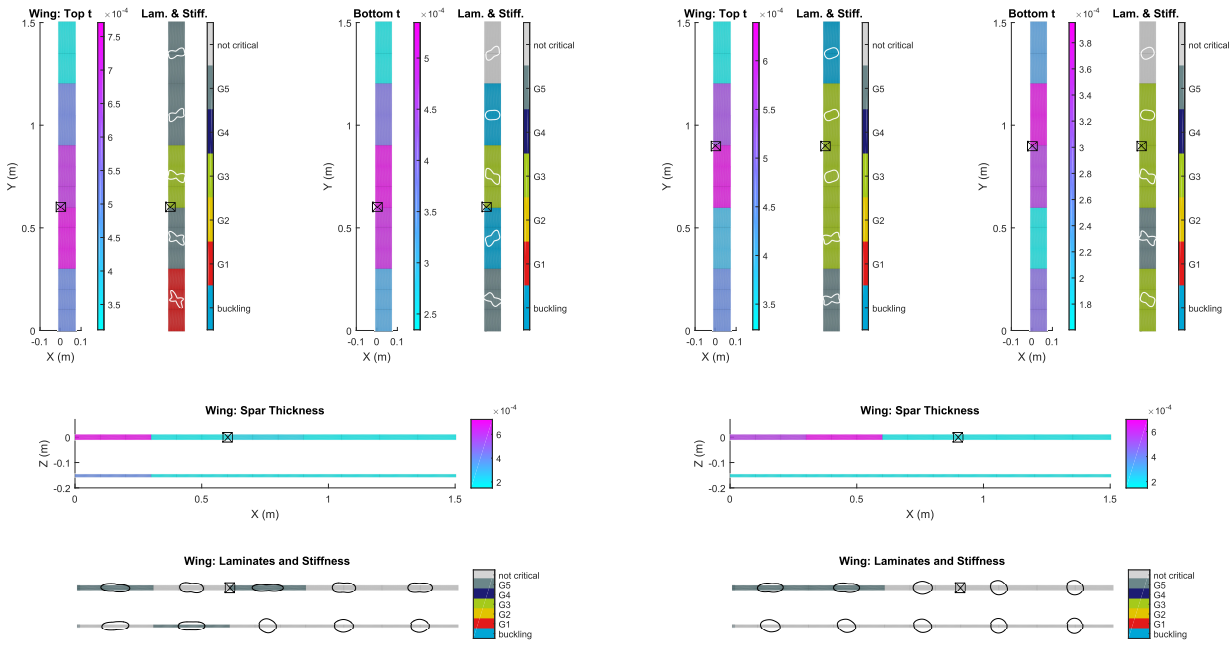


Figure 7.10: Tailoring results for SBW configurations with $x_{strut} = 30\%c$ and $EAs_{strut} = 100kN$

wing connection, yet the SBW with $y_{strut} = 60\%b$ shows smaller values for this maximum thickness.

The optimized maximum spar thickness is very similar for the two configurations. At the same time the $y_{strut} = 60\%b$ -case holds a larger region of this maximum thickness as compared to the case with $y_{strut} = 40\%b$. This can simply be linked to the larger span that is affected by the normal force caused by the horizontal component of the force induced by the strut.

The stiffness tailoring in the spars of the SBW in figure 7.10b does not show any unexpected behavior at this point, but is somewhat less pronounced than the one in figure 7.10a. This can be related to the decrease in normal force that was observed for increasing y_{strut} in section 6.8.3.

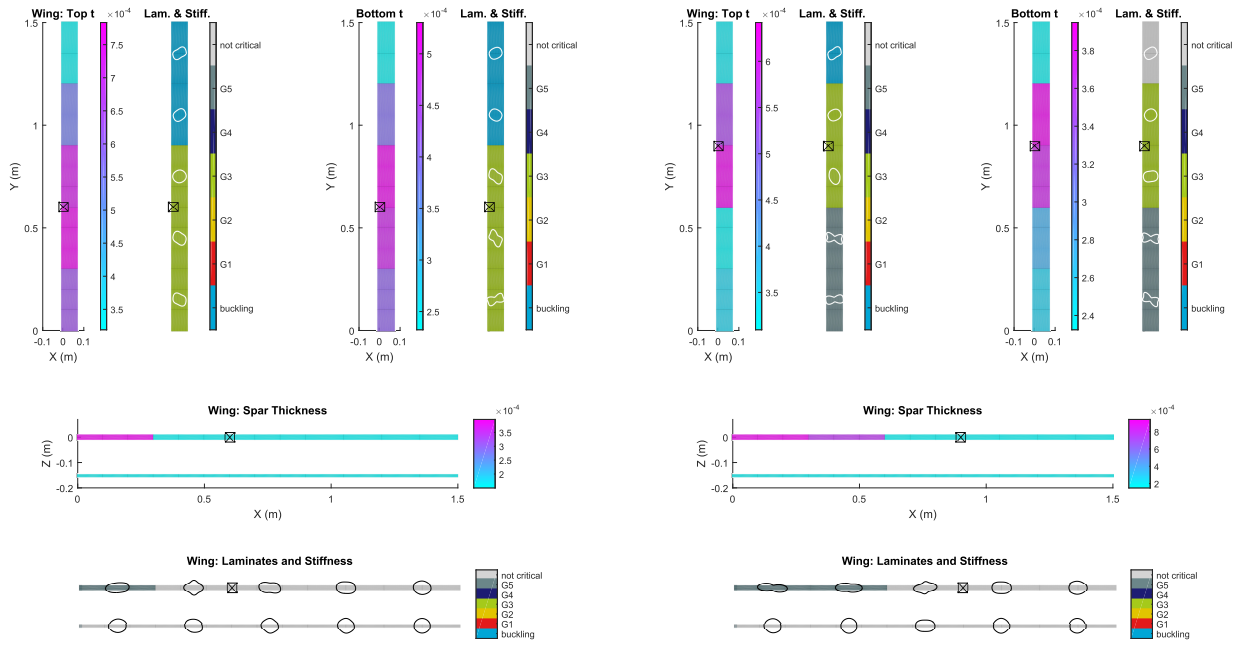
The most important conclusion that can be drawn from this direct comparison is that the stiffness tailoring results in top and bottom skins for the SBW with $y_{strut} = 60\%b$ in figure 7.10b are more or less counter-acting each other, whereas the stiffness results in both skins in the SBW in figure 7.10a contribute to the same effect.

Figure 7.11 shows the same comparison as figure 7.10, but then for configurations with $EAs_{strut} = 500kN$. The thickness distribution in the spars follow the same principle as was the case for the SBWs in figure 7.10. The maximum thickness is however much higher for the SBW with $y_{strut} = 60\%b$ than for the $y_{strut} = 40\%b$ SBW. This observation suggests that the spar-induced-wash-out effect at the root is much larger for the configuration in figure 7.11b.

A comparison of the tailored spar stiffness between these two configurations does not yield any new insights with respect to the SBWs in figure 7.10. The thickness distribution in the top and bottom skin also follow the same trends as seen for the sets that were discussed previously.

Stiffness tailoring results in top and bottom skin in figure 7.11b are however more dissimilar from one laminate region to another than can be seen in figure 7.11a or for the SBW with $EAs_{strut} = 60\%b$ in figure 7.10b.

Although the optimized thickness in the spars still suggests that the SBWs with $y_{strut} = 60\%b$ are tailored for wash-out at the root, this is not confirmed by the stiffness distribution in the upper and lower skins. To be able to explain why the tailored SBWs show the thickness and stiffness properties they obtained through aeroelastic tailoring, a closer look at the resulting aeroelastic deformations and active design constraints needs to be taken.

Figure 7.11: Tailoring results for SBW configurations with $x_{strut} = 30\%c$ and $EA_{strut} = 500\text{kN}$

7.2.2. Static aeroelastic deflection of tailored SBWs

A quick glance at figure 7.12, reveals that aeroelastic tailoring resulted in a small relief in tip deflection compared to the initial designs. All other configurations show the same behavior, as can be seen in appendix E.

Only the SBWs with $x_{strut} > 30\%c$ in figures E.1 show an increase of positive wing twist with respect to the initial design. Although a positive twist relates to the presence of a wash-in effect, which would be disadvantageous for any conventional wing, the aeroelastic tailoring did apparently not have the incentive to avoid this deformation. The SBW with $x_{strut} = 50\%c$ shows the same deformation, although to a smaller extent.

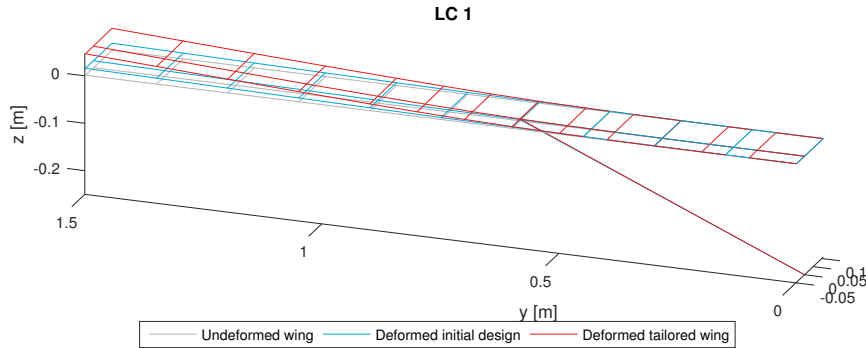
Figure 7.12: Static aeroelastic deformation of SBW with $y_{strut} = 40\%b$, $x_{strut} = 30\%c$ and $EA_{strut} = 100\text{kN}$ for load case 1

Figure 7.13 provides the quantified wing twist and vertical deformation that correspond to the tailored SBWs from subset A with $y_{strut} = 40\%b$. The relieving effect of aeroelastic tailoring on vertical deflection δ_z is strongly related to the stiffness of the strut and shows no surprises. Figure 7.14 presents the same data for SBWs from subset B with $y_{strut} = 40\%b$.

θ_y shows larger variations between the four configurations presented. The effect of the tailored stiffness in the five design regions can be recognized by the kinks shown in θ_y at the borders of those regions. The

first three laminate regions ($0 < y < 0.9\text{m}$) show the most variation, while regions towards the tip show more or less constant twist, which is very similar to the effect tailoring of the clean wing showed in figure 7.5. The inboard laminate regions in figure 7.5 indicated a wash-out effect that is indeed causing a negative wing twist in these regions.

The wing twist results in figure 7.13 also reveal that the wash-in effect that was implied by the tailored wing tip stiffness in 7.8, does not result in actual wash-in with respect to the wing twist. The tailored stiffness does stop negative wing twist to further progress after $y > 0.9\text{m}$, but only decreases the degree of wash-out initiated at the root section, instead of introducing actual wash-in. This can be related to the smaller amount of strain that is present towards the wing tip than at the root. As a result, the stiffness tailoring at the tip is of smaller influence, which is this case stabilizes the wing twist.

It can be seen the reduction of wash-out towards the wing tip is most distinct for the SBW with $EA_{strut} = 100\text{kN}$. Figure 7.8c shows that this is also the SBW with the most pronounced tailoring, which proves that the tailored stiffness and aeroelastic wing twist are indeed in very close relation.

Furthermore, figure 7.13 shows increasing values of θ_y for decreasing EA_{strut} . Figure 7.14 illustrates the strong influence of x_{strut} on θ_y that was earlier found in the sensitivity studies in section 6.8. θ_y is positive for $x_{strut} > 30\%c$, which shows that even though the wing is tailored, the mechanism explained in figure 6.8 in section 6.6, still holds. The kink at $y = 0.6\text{m}$ is caused by the presence of the strut-wing connection at this location.

For all SBW configurations reviewed in these two figures, aeroelastic tailoring has resulted in increased deflections. The results of the SBWs with $y_{strut} = 60\%b$ are presented in appendix E, and display the same effects as discussed here.

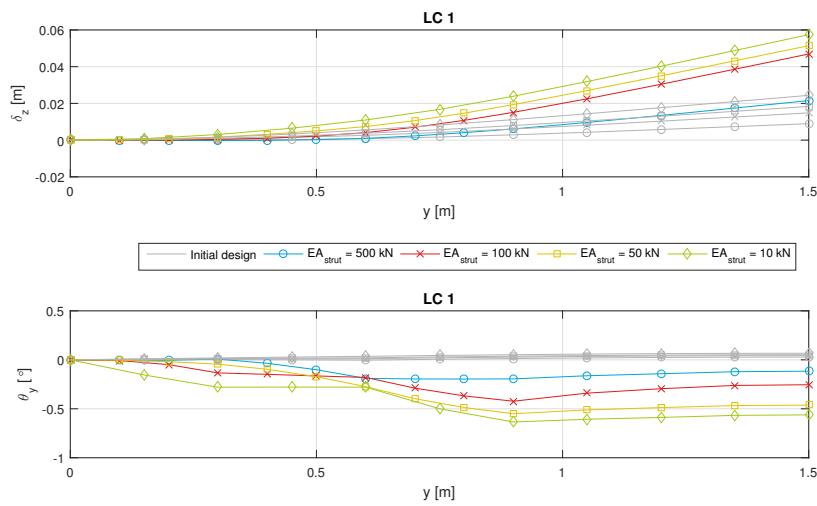


Figure 7.13: Static aeroelastic deformation of SBWs with $y_{strut} = 40\%b$, $x_{strut} = 30\%c$, and varying EA_{strut} for load case 1

To conclude the study on the effect of aeroelastic tailoring on aeroelastic deflections of the fourteen SBWs that were optimized, figures 7.15 and 7.16 summarize the vertical tip deflection $\delta_{z_{tip}}$ and tip twist $\theta_{y_{tip}}$ for the full set of tailored SBW configurations.

Figure 7.15 shows that the deflections of the tailored designs are generally larger than those of the corresponding initial designs. Furthermore, the aeroelastic tailoring procedures enabled larger deflections for all considered configurations, except for the SBW with $EA_{strut} = 500\text{kN}$, $x_{strut} = 30\%c$, $y_{strut} = 60\%b$. Deflections increase for decreasing axial strut stiffness EA_{strut} and for decreasing y_{strut} , as was expected based on the sensitivity studies in section 6.8.

Figure 7.15 shows a relative large difference between $\delta_{z_{tip}}$ of the tailored SBW with $EA_{strut} = 100\text{kN}$, $x_{strut} = 30\%c$, $y_{strut} = 40\%b$, and its equivalent with $y_{strut} = 60\%b$, compared to the other configurations. Now, examination of figure 7.10 reveals that the corresponding stiffness results of the $y_{strut} = 40\%b$ -case in figure 7.10a has a more pronounced wash-in effect at the tip than the SBW with $y_{strut} = 60\%b$ in figure 7.10b. This comparison this proves that a more pronounced wash-in effect at the tip indeed results in a larger vertical wing tip deflection.

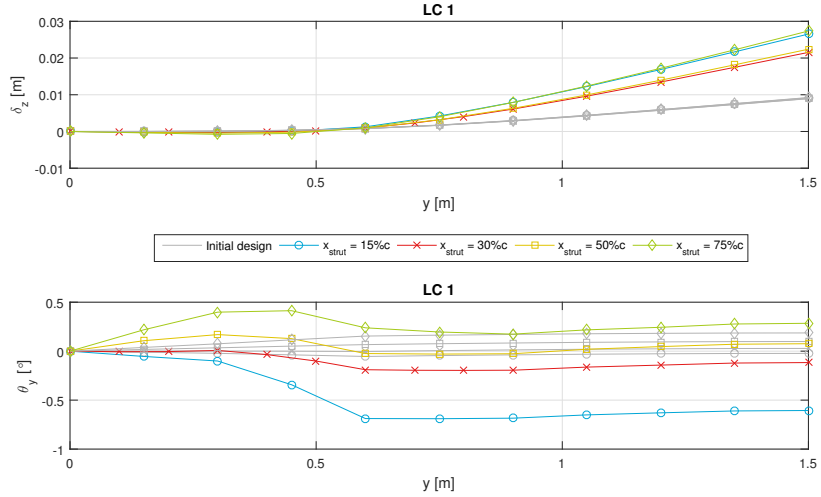


Figure 7.14: Static aeroelastic deformation of SBWs with $y_{strut} = 40\%b$, $EA_{strut} = 500kN$, and varying x_{strut} for load case 1

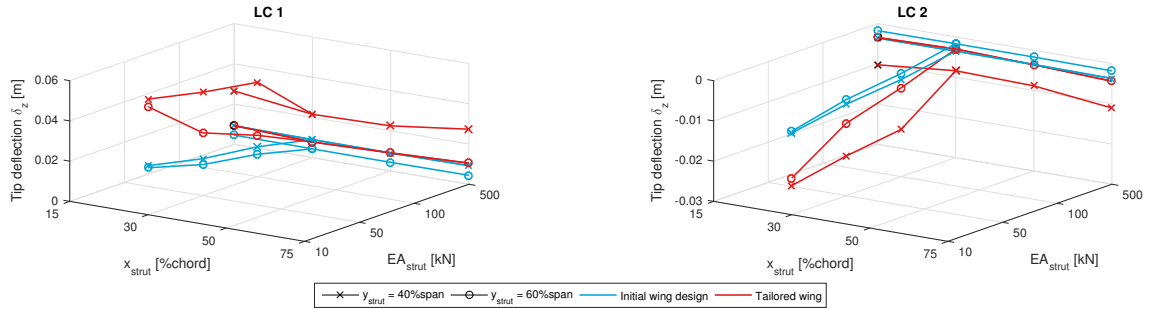


Figure 7.15: Vertical tip deflection for $\delta_{z_{tip}}$ for all SBW configurations from the optimization set

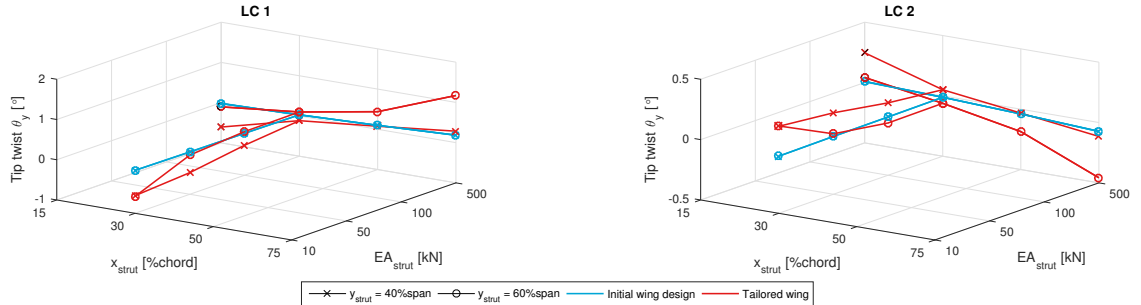


Figure 7.16: Tip twist $\theta_{y_{tip}}$ for all SBW configurations from the optimization set

This investigation is repeated for the SBWs with $EA_{strut} = 500kN$ and $x_{strut} = 30\%c$. Figure 7.11 depicts a smaller difference in wash-in tailoring at the wing tip between the SBWs with $y_{strut} = 40\%b$ and $y_{strut} = 60\%b$, than was visible for the two configurations in figure 7.10. This smaller difference is directly related to the smaller difference in $\delta_{z_{tip}}$ that is shown in figure 7.15 for these SBWs.

The wing tip twist results in figure 7.16 show a less clear increase or decrease from initial design to tailored wing. As was also noted for the clean wing in figure 7.5, the initial wing design experiences almost no twist for the applied load cases. Figure 7.16 illustrates how the twist increases for increasing x_{strut} , well in line with the expected effect.

Additionally, the total lift results are plotted in figure 7.17. Although the differences are small, it clearly

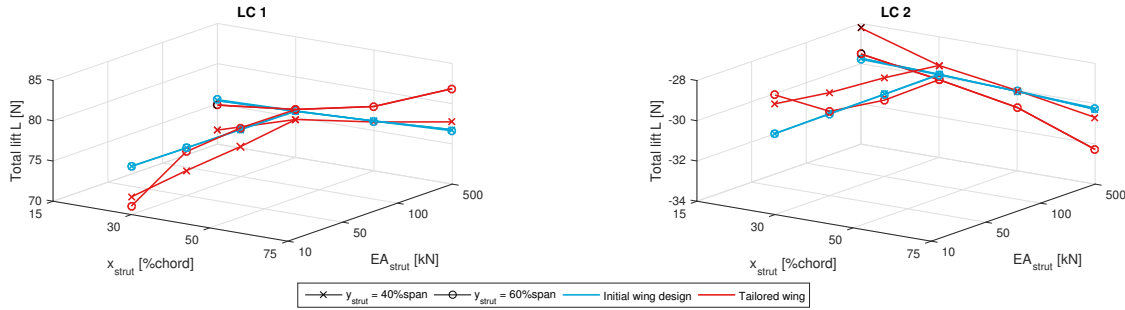


Figure 7.17: Total lift L for all SBW configurations from the full optimization set

visible that the total lift generated by the wing is in very tight relation with the tip twist shown in figure 7.16, and thus with the degree of wash-in that is achieved at the wing tip.

Although the previous results can all be related to the thickness and stiffness tailoring results that were presented in section 7.2, a full explanation for the uncommon of wash-out tailoring at the root of the tailored SBWs has not been found yet. Therefore, the constraints that were driving the tailoring procedures towards their final result are investigated in section 7.2.3.

7.2.3. Active design constraints

Table 7.2 summarizes the most critical constraints for each of the initial SBW design and their final tailoring result. A review of the constraint violation history of all fourteen tailoring procedures shows that the design of all SBWs is eventually mainly driven by flutter constraints, which explains the presence of wash-in tailoring at the wing tips (Weisshaar, 1987). In the first ten or fifteen iterations buckling of the top and bottom skin are key drivers after any aeroelastic instabilities have been resolved. Once the design has converged the most violated constraints are associated with lamination parameters and aeroelastic stability of the SBW. Strain did not play a role in the outer design iterations for any of the SBWs, except for laminate regions 6, 12, 18 and 24 corresponding to the strut with $EA_{strut} = 10kN$.

Table 7.2: Final set of SBW configuration for aeroelastic tailoring studies

SBW configuration			Nr. of violated constraints at start	Most violated constraint	
$y_{strut}[\%b]$	$x_{strut}[\%c]$	$EA_{strut}[kN]$		initial design	final design
40	15	500	1	flutter	G5: lam.2
	30	500	1	flutter	G3: lam.7
	30	100	2	flutter	G1: lam.9
	30	50	5	flutter	flutter
	30	10	2	flutter	G1: lam.9
	50	500	1	flutter	flutter
	75	500	0	flutter	G5: lam. x
60	15	500	0	flutter	G5: lam.14
	30	500	0	flutter	G5: lam.7
	30	100	2	flutter	flutter
	30	50	3	flutter	G5: lam.8
	30	10	1	flutter	G5: lam.7
	50	500	1	flutter	G3: lam.8
	75	500	0	flutter	G5: lam.20

The most active constraints that have a direct relation to the laminates, are highlighted in figure 7.8 to 7.11 and figures D.1 to D.2 in appendix D. The light blue patches in the indicate the laminates critical buckling. From comparing the results of optimization subsets A, B and C to each other, it becomes apparent that the tailored SBWs with the strut at 60% of their span experience less buckling, than the SBWs with $y_{strut} = 40\%b$. The generally smaller root bending moment for the former set of configurations and the smaller vertical tip deflection that were identified in earlier discussions can be linked to this observation.

The grey patches indicate laminates that are not subjected to one of the first 30 most violated constraints. 'Not critical'-laminates are typically found at the bottom skin near the wing tip, which is also the laminate that appears to be tailored less than the other laminate regions with respect to stiffness.

The trends with respect to active design drivers, show to be similar to those observed for tailoring of the clean wing. The uncommon occurrence of the constraints on lamination parameters G3 and G5 as the most violated constraints indicates that the flutter margin is maximized at the boundaries of the laminate feasibility region (Diaconu et al., 2002). This is again linked to the extreme narrow band in which the SBW configurations experience aeroelastic stability. To further investigate the aeroelastic stability of the SBWs, the most critical aeroelastic modes are examined.

The complete set of the most critical aeroelastic eigenmodes is provided by appendix G. The characteristics of the most critical aeroelastic modes for SBWs subset A are given here by figure 7.18. The corresponding eigenvalues are provided by table 7.3. The magnitude of the real part of the eigenvalues reveals that though the aeroelastic modes are stable, they are associated with very low damping. The table also presents the intuitive effect that an increase in strut stiffness results in an increase in flutter frequency. Furthermore, it appears that an increase in strut stiffness corresponds to a more stable configuration, except for the SBW with $EA_{strut} = 100kN$, which is the configuration with the lowest damping in this list. The most critical eigenvalues for SBWs with $y_{strut} = 60\%$ that are provided by table G.1 exhibit the same trends, but are even more critical in terms of damping than the eigenvalues in table 7.3. Going back to figure 7.11, this can be related to a larger area of wash-in stiffness tailoring that is observed for $y_{strut} = 60\%$ than for $y_{strut} = 40\%$.

Table 7.3: Most critical eigenvalues for SBWs from subset A ($y_{strut} = 40\%$)

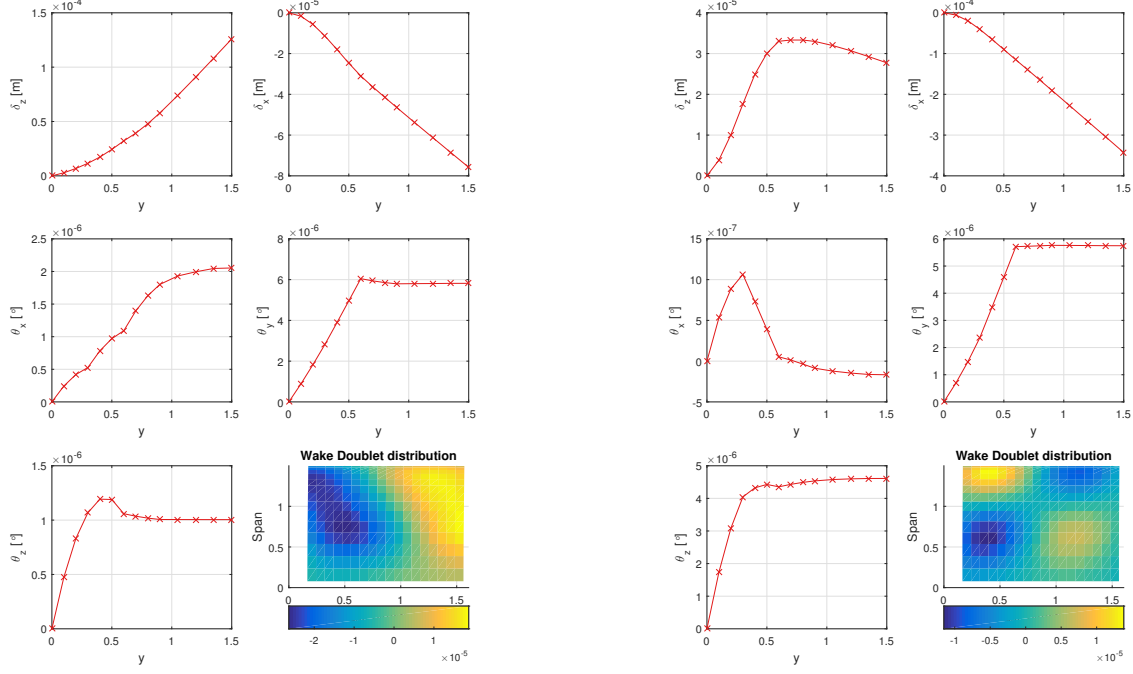
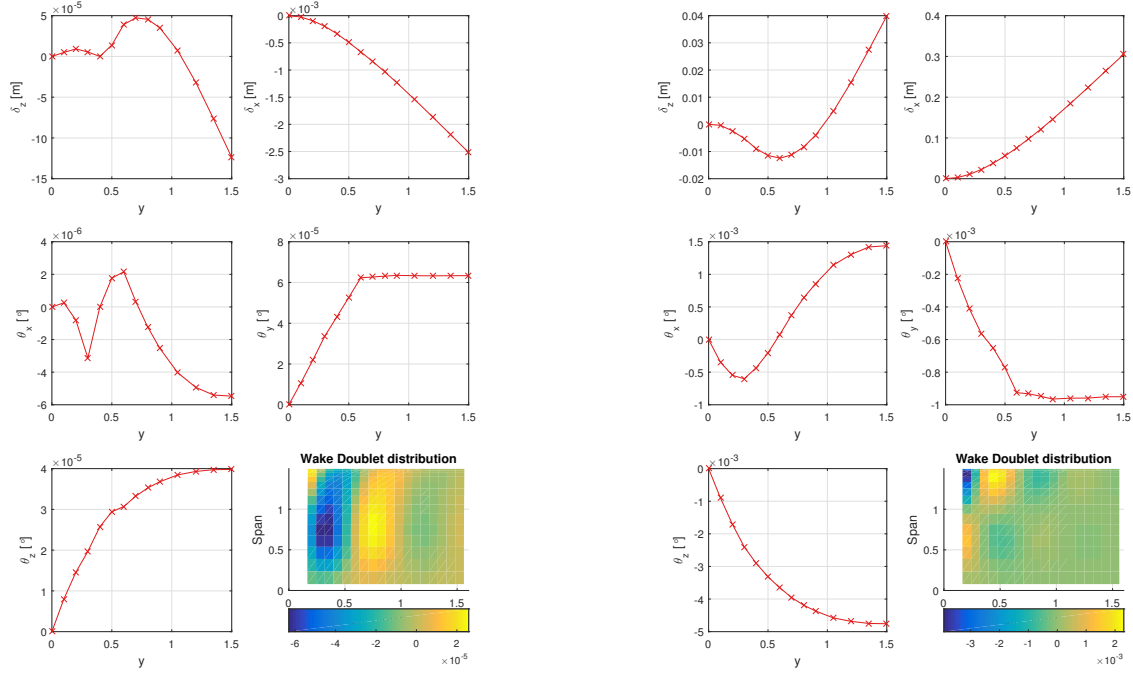
SBW configuration			Most critical aeroelastic eigenvalue	
$y_{strut}[\%b]$	$x_{strut}[\%c]$	$EA_{strut}[kN]$	$Re(\lambda)$	$f[Hz]$
40	30	10	-0.0001	11.41
	30	50	-0.0003	16.49
	30	100	-3.27E-08	32.38
	30	500	-0.0129	38.32

The deformations that correspond to the most critical eigenmode shown in figure 7.18 clearly expose the location of the strut-wing connection. Although the wing twist angles are small, all θ_y -plots show a clear kink at $y = 0.6m$, where the connection is located.

The narrow band of aeroelastic stability that is dominating the tailoring results is confirmed by the extreme small deformations that correspond to the critical modes for the SBWs with $EA_{strut} = 10, 50, 100kN$. The modes are associated with bending-torsion coupling and in-plane bending but to very minimal extent. The configuration with the highest axial strut stiffness in figure 7.18d does experience a mode that would actually be visible with the naked eye, which is a combination of in-plane and out-of-plane-bending. Figure G.1 in appendix G demonstrates that for configurations with $y_{strut} = 60\%b$ an increase in EA_{strut} also relates to more distinct eigenmodes, with respect to the magnitude of the corresponding deformations.

For each of the four configurations in figure 7.18 the alternating doublet strengths in the wake confirm the existence of flutter. With that observation it can be concluded that the aeroelastic tailoring results of these four SBWs are dominated by a very small but critical flutter mode.

The other subsets of SBW configurations that present the characteristics of their corresponding critical modes in figure G.1 show comparable behavior. The eigenmodes in figures G.2 and G.3 correspond to subset B with $EA_{strut} = 500kN$ and therefore also show much more distinct deformations than are visible in figure 7.18. As a consequence their doublet distributions deviate from those seen for subset A.

(a) Axial strut stiffness $EA_{strut} = 10\text{kN}$ (b) Axial strut stiffness $EA_{strut} = 50\text{kN}$ (c) Axial strut stiffness $EA_{strut} = 100\text{kN}$ (d) Axial strut stiffness $EA_{strut} = 500\text{kN}$ Figure 7.18: Characteristics of most critical eigenmodes for SBWs from subset A ($y_{strut} = 40\%$ and $x_{strut} = 30\%$)

7.3. Tailored SBW mass

To conclude the large set of results the tailoring procedures are investigated with regard to the optimization objective.

7.3.1. Convergence history

Aeroelastic tailoring was performed on fourteen different SBW configurations. It was found that they not only resulted in a large variation of stiffness and thickness distributions, but also the optimization procedure itself showed noticeable differences. In order to compare the convergence histories of all optimizations that were performed, the definition of the three configuration subsets as defined in section 7.2 is used.

The convergence history of subset A in figure 7.19 shows a number of jumps in the SBW mass over the coarse of the design iterations for the configurations with $EA_{strut} < 500\text{ kN}$. It seems that for these configurations the optimization finds itself stuck in a local minimum at certain points throughout the process. The optimization procedures for subset B in figure 7.20 show a much smoother progress, and were consequently terminated at an earlier stage than those in subset A.

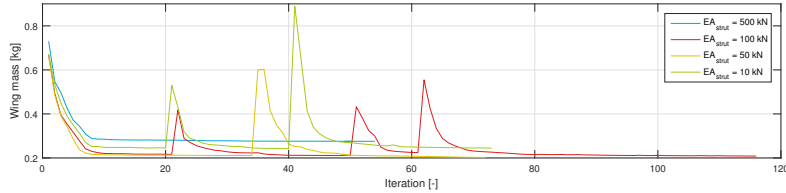


Figure 7.19: Convergence history for SBWs from subset A with $y_{strut} = 40\%$, $x_{strut} = 30\%$, and varying EA_{strut}

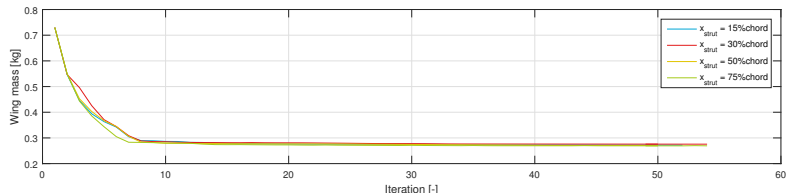
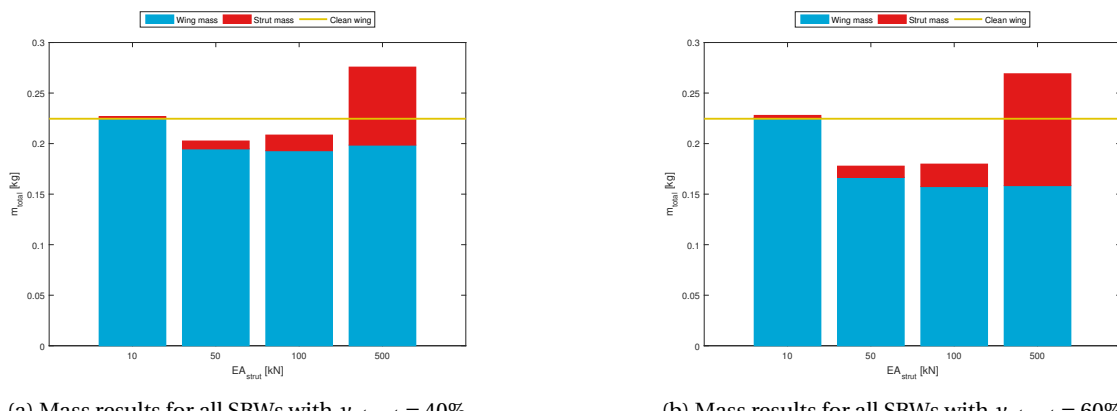


Figure 7.20: Convergence history for SBWs from subset B with $EA_{strut} = 500\text{ kN}$, $y_{strut} = 40\%$, and varying x_{strut}

7.3.2. Optimized SBW mass

Finally, the actual objective of the optimization procedures is investigated to find the most optimal SBW design in terms of mass. Figure 7.21 and 7.22 together illustrate how the total mass of the full set of tailored SBW configurations is build up. Table 7.4 provides the corresponding numerical mass values and the differences with respect to the tailored clean wing.



(a) Mass results for all SBWs with $y_{strut} = 40\%$

(b) Mass results for all SBWs with $y_{strut} = 60\%$

Figure 7.21: Static aeroelastic deflection for SBW configurations in subset A ($x_{strut} = 30\%$)

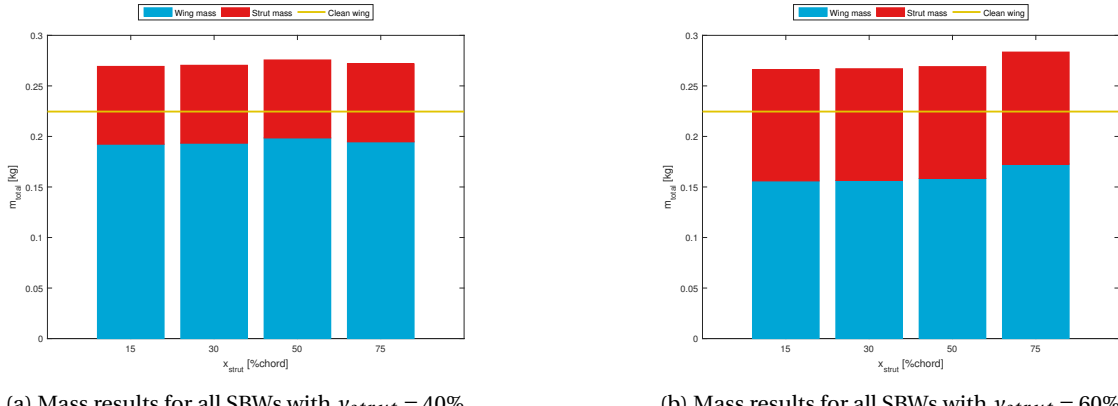
(a) Mass results for all SBWs with $y_{strut} = 40\%$ (b) Mass results for all SBWs with $y_{strut} = 60\%$ Figure 7.22: Static aeroelastic deflection for SBW configurations in subset B ($EA_{strut} = 500\text{kN}$)

Table 7.4: Mass results of aeroelastic tailoring procedures

SBW configuration			Mass [kg]	Mass difference w.r.t. tailored clean wing [%]
y_{strut} [%b]	x_{strut} [%c]	EA_{strut} [kN]		
Clean wing			0.2246	-
40	15	500	0.2718	21.02
	30	500	0.2757	22.75
	30	100	0.2084	-7.21
	30	50	0.2026	-9.80
	30	10	0.2268	0.98
	50	500	0.2704	20.39
	75	500	0.2696	19.90
60	15	500	0.2835	26.22
	30	500	0.2691	19.81
	30	100	0.1797	-19.99
	30	50	0.1777	-20.88
	30	10	0.2279	1.47
	50	500	0.2670	18.88
	75	500	0.2660	18.43

In figure 7.21 it can be seen that although the wing mass is smallest for the configurations associated with $EA_{strut} = 500\text{kN}$, the addition of the strut weight makes them much heavier than the tailored clean wing. It is interesting to see that the SBWs with $y_{strut} = 60\%$ result in the lightest configurations, while the longer strut member adds more mass compared to the strut at $y_{strut} = 40\%$.

Apparently, the relieving effect of the strut at $y_{strut} = 60\%$ on the root bending moment causes a weight saving potential that is larger than the mass increase that originates from increasing strut length from a strut with $y_{strut} = 40\%$ to a strut with $y_{strut} = 60\%$.

Figure 7.22 shows the tailored mass results for the SBWs in subset B. Since this subset consists of configurations with the largest axial strut stiffness, the strut makes a very large contribution to the total weight. As a result all SBWs in figure 7.22 have a larger mass than the clean wing. An isolated look at the effect of x_{strut} on the wing mass only reveals however that a strut-wing connection near the leading edge is favourable over a chordwise location to the rear.

Based on the final mass results presented in this section, it can be concluded that the SBW with a strut at 60% of its span and axial stiffness within a range from 50 to 100 kN results in the best design, with a maximum mass decrease of 20.9% with respect to the tailored clean wing. The study on the effect of chordwise strut location x_{strut} suggests that an even lighter design could be found when combining the former finding with $x_{strut} < 30\%$.

8

Conclusions and recommendations

This thesis involved the investigation of aeroelastic tailoring for weight minimization on an elementary strut-braced wing (SBW) design. SBWs are believed to have great potential because of the aerodynamic efficiency enabled by the high slenderness of the wings. At the same time this high degree of slenderness results in great wing flexibility which in turn makes the configurations very prone to aeroelastic instabilities. SBWs have been the focus of increased research attention over the last few years, from which the most state-of-the-art SBW is currently being developed by Boeing in light of their Subsonic Ultra Green Aircraft Research (SUGAR). Nevertheless, flutter constraints and active load alleviation systems still cause critical weight penalties that diminish the benefits of SBWs with respect to clean wings.

To test whether aeroelastic tailoring can increase the potential of SBWs by taking away the need for flutter weight, the existing aeroelastic tailoring framework Proteus was modified and verified to enable strut-braced wing design, after which fourteen SBWs —differing in strut configuration— and one clean reference wing were optimized for minimum weight.

8.1. Conclusion

Tailoring of the clean wing resulted in the development of a wash-out effect at the root of wing while the wing tip was optimized for wash-in as to increase flutter margins. Also the spar thickness tailoring induced wash-out near the root. The static aeroelastic deformations of the wing clearly indicated the effect of the stiffness tailoring, but the incentive for tailoring for specific stiffness distributions was coming from the aeroelastic stability constraints that showed to be very active throughout the optimization procedure. Because the extremely narrow band of aeroelastic stability for this high aspect ratio wing, lamination parameter constraints turned out to be part of the most active constraints.

For all SBWs the optimized thickness achieves its maximum in the laminate regions that enclose the strut-wing connection and reduces again towards the wing tip. In general, the tailored SBWs showed stiffness distributions comparable to that of the tailored clean wing, implying the presence of a wash-out effect at the wing root and wash-in at the tip. Stiffness tailoring in the spars is however very strongly related to the magnitude of compressive normal force that the strut introduced in the wing when applying tension for a positive wing loading.

For SBWs with a spanwise strut location further away from the wing root, the optimized stiffness distribution in the top and bottom skins appeared to be more volatile from one design region to another. The combination of the stiffness and thickness distribution throughout the skins in these wings also did not consequently aim at a certain effect, but appeared to be rather contradicting. Larger regions of wash-in tailoring corresponded, and thus larger regions of tailoring for flutter, corresponded to lower damping values.

Static aeroelastic deformations of the tailored SBWs were mainly dominated by the strut configuration parameters, e.g. chordwise and spanwise location of the strut-wing connection, and the axial stiffness of the strut member. The deformations generally decrease for an increase in axial stiffness of the strut or an increase in span. The chordwise location of the strut-wing connection showed to strongly influence the wing twist, which increases for a connection moving aft. The total lift exhibited in turn a very strong relation to the amount of wing tip twist.

The tailored stiffness at the root of the SBWs indeed related to an increasing degree of wash-out, but the suggested wash-in effect at the tip merely caused the wing twist to become constant over the remaining part of the wing, causing a slight decrease of the wash-out effect instead of causing actual wash-in. This could however still be related to tailoring for flutter.

Similar to the process observed in the clean wing optimization, the key drivers in the first stages of the optimization were buckling constraints, while aeroelastic stability and lamination parameter constraints dominated the converged design.

From a review of the most critical eigenmodes of the tailored SBW designs it was found that struts with a higher axial stiffness result in more distinct eigenmodes that are excited at higher frequencies, while lower values of axial stiffness correspond to modes that are associated to extremely small deformations and lower frequencies.

Finally, it was found that the tailored wing mass decreases for increasing strut stiffness, but that this is not necessarily true for the total mass of the configuration. The best SBW design is found in the configuration with a strut that connects at 60% of the wingspan, and has the second lowest axial stiffness out of the analysis range. A mass reduction of 20.9% with respect to the clean wing is achieved, which again shows the great potential of SBWs over conventional wings, but —more importantly— indicates the added value of the application of aeroelastic tailoring to these configurations and its power to avoid flutter without paying weight penalties that have been dominating SBW-research up to this point.

Although further research should be done on full scale SBWs, the results of this work certainly demonstrate that aeroelastic tailoring can successfully overcome flutter weight penalties and leaves promising windows for improvement of the full scale Boeing SUGAR wing.

8.2. Recommendations

The research performed for this thesis work sheds a light on the attributes of the application of aeroelastic tailoring to SBW designs. The assumptions and limitations that were posed on this research open a number of openings for improvement of this work.

The most prominent point for improvement is the expansion to a full scale strut- or truss-braced wing, with the same dimensions as the Boeing SUGAR wing. The present studies were performed on a simplified scale model, so although the results are positive, further research should be done on full scale models in order to draw conclusions directly relevant for large-passenger aircraft wings. Advanced research effort should then also include all non-structural masses such as engines, control surfaces and fuel tanks in order to compare results of aeroelastic tailoring to the untailored SUGAR wing and find its direct benefits. To be able to fully implement the SUGAR wing into the aeroelastic tailoring framework, Proteus should be expanded for truss-braced wing design, where the supporting structure consists of multiple members.

If aeroelastic tailoring on this state-of-the-art model then eliminates flutter weight penalties as is implied by the promising results of the current work, the future of aviation will no longer only entail the ever conventional tube-wing aircraft but head towards the strut-braced wing in order to seriously address the significant contribution of air transport to global CO_2 production.

Secondly, the aeroelastic tailoring results could be validated with aeroelastic wind tunnel experiments on the scale models similar to the wing model described by this thesis.

Additionally, the results and final conclusions also hint for areas where this research can be continued and improved. To improve the work on a smaller scale, the size of the optimized section of the wing could be increased, since it is currently only spanning half of the wing cross-section. Furthermore, the number of design regions could be increased to identify a more accurate stiffness distribution.

A third expansion of the current work could be directed at optimization of the thickness and stiffness distribution in the strut itself, as the strut properties were kept constant so far. This would entail additional modifications to the Proteus framework.

Fourthly, the fact that lamination parameter constraints were one of the most active constraints during optimization, directs towards further investigation of the relation between laminate feasibility regions and critical flutter speeds.

Finally, as the results suggest that an even lighter SBW design can be achieved when combining the optimum configuration with a strut-connection more towards the leading edge of the wing, the optimization set could be expanded to include such configurations.

Bibliography

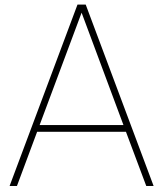
- Timothy Allen, Bradley Sexton, and Matthew J Scott. SUGAR Truss Braced Wing Full Scale Aeroelastic Analysis and Dynamically Scaled Wind Tunnel Model Development. In *56th AIAA/ASCE/AHS/ASC Structures, Structural Dynamics, and Materials Conference*, number January, pages 1–8. AIAA SciTech, Kissimmee, FL, 2015. ISBN 9781624103421. doi: doi:10.2514/6.2015-1171.
- Robert E Bartels, Robert C Scott, Timothy J Allen, and Bradley W Sexton. Aeroelastic Analysis of SUGAR Truss-Braced Wing Wind-Tunnel Model Using FUN3D and a Nonlinear Structural Model. In *56th AIAA/ASCE/AHS/ASC Structures, Structural Dynamics, and Materials Conference*, number January, pages 1–15, Kissimmee, FL, 2015. AIAA SciTech. ISBN 978-1-62410-342-1. doi: doi:10.2514/6.2015-1174.
- Jean Marc Battini and Costin Pacoste. Co-rotational beam elements with warping effects in instability problems. *Computer Methods in Applied Mechanics and Engineering*, 191(17-18):1755–1789, 2002. ISSN 00457825. doi: 10.1016/S0045-7825(01)00352-8.
- Manav Bhatia, Rakesh Kapania, Maarten van Hoek, and Raphael Haftka. Structural Design of a Truss Braced Wing: Potential and Challenges. In *50th AIAA/ASME/ASCE/AHS/ASC Structures, Structural Dynamics, and Materials Conference - Done*, number May, Palm Springs, CA, 2009. ISBN 978-1-60086-975-4. doi: 10.2514/6.2009-2147.
- Manav Bhatia, Ohad Gur, Joseph A Schetz, William H Mason, and Raphael T Haftka. Progress Towards Multidisciplinary Design Optimization of Truss Braced Wing Aircraft with Flutter Constraints. In *AIAA/ISSMO Multidisciplinary Analysis Optimization Conference*, number September, Fort Worth, Texas, 2010. ISBN 9781600869549. doi: 10.2514/6.2010-9077.
- Manav Bhatia, Rakesh K. Kapania, and Raphael T. Haftka. Structural and Aeroelastic Characteristics of Truss-Braced Wings: A Parametric Study. *Journal of Aircraft*, 49(1):302–310, 2012. ISSN 0021-8669. doi: 10.2514/1.C031556.
- Maxwell Blair, Robert A. Canfield, and Ronald W. Roberts. Joined-Wing Aeroelastic Design with Geometric Nonlinearity. *Journal of Aircraft*, 42(4):832–848, 2005. ISSN 00218669. doi: 10.2514/1.2199.
- Marty K. Bradley and Christopher K. Droney. Subsonic Ultra Green Aircraft Research: Phase I Final Report. Technical Report NASA/CR-2011-216847, Boeing Research & Technology, Huntington Beach, 2011.
- Marty K Bradley, Timothy J Allen, and Christopher K Droney. Subsonic Ultra Green Aircraft Research: Phase II – Volume III – Truss Braced Wing Aeroelastic Test Report NASA STI Program . . . in Profile. III(April 2014), 2014.
- Marty K. Bradley, Christopher K. Droney, and Timothy J. Allen. Subsonic Ultra Green Aircraft Research. Phase II - Volume I - Truss Braced Wing Design Exploration. Technical Report NASA/CR-2015-218704, Boeing Research and Technology, Huntington Beach, 2015.
- G Carrier, O Atinault, S Dequand, J L Hantrais-Gervois, C Liauzun, B Paluch, a M Rodde, and C Toussaint. Investigation of a Strut-braced wing configuration for future commercial transport. In *28th Congress of the International Council of the Aeronautical Sciences*, 2012. ISBN 9781622767540.
- Rauno Cavallaro and Luciano Demasi. Challenges, Ideas, and Innovations of Joined-Wing Configurations: A Concept from the Past, an Opportunity for the Future. *Progress in Aerospace Sciences*, 87:1–93, 2016. ISSN 03760421. doi: 10.1016/j.paerosci.2016.07.002.
- Rauno Cavallaro, Luciano Demasi, and Andrea Passariello. Nonlinear Analysis of PrandtlPlane Joined Wings: Effects of Anisotropy. *AIAA Journal*, 52(5):964–980, 2014. ISSN 0001-1452. doi: 10.2514/1.J052242.

- Imon Chakraborty, Taewoo Nam, Jonathan R. Gross, Dimitri N. Mavris, Joseph a. Schetz, and Rakesh K. Kapania. Comparative Assessment of Strut-Braced and Truss-Braced Wing Configurations Using Multidisciplinary Design Optimization. *Journal of Aircraft*, 52(6):2009–2020, 2015. ISSN 0021-8669. doi: 10.2514/1.C033120.
- P.C. Chen and E. Sulaeman. Nonlinear Response of Open/Closed-Loop Aeroelastic System Using a Discrete State-Space Approach. In *44th AIAA/ASME/ASCE/AHS/ASC Structures, Structural Dynamics, and Materials Conference*, number April, Norfolk, VA, 2003. ISBN 978-1-62410-100-7. doi: 10.2514/6.2003-1734.
- Gabriel P Chiozzotto. Conceptual Design Method for the Wing Weight Estimation of Strut-Braced Wing Aircraft. In *5th CEAS Air & Space Conference*, 2015.
- John M. Coggin, Rakesh K. Kapania, Joseph A Schetz, H. Vijayakumari, and Wei Zhao. Nonlinear Aeroelastic Analysis of a Truss Based Wing Wind Tunnel Model. In *55th AIAA/ASME/ASCE/AHS/SC Structures, Structural Dynamics, and Materials Conference*, number January, National Harbor, MD, 2014. doi: 10.2514/6.2014-0335.
- Hexcel Composites. HexPly 8552 Product Data, 2013. URL [https://www.google.nl/url?sa=t&q=esrc=s&source=web&cd=1&cad=rja&uact=8&ved=0ahUKEwjnq07zxJLSAhUJrRoKHR_{_}CCY4QFggcMAA&url=http%3A%2F%2Fwww.hexcel.com%2FResources%2FDataSheets%2FPreg-Data-Sheets%2F8552_{_}eu.pdf&usg=AFQjCNGt5LSVqsFNwxr7dRNqRM-CMR2nkw&{&}.](https://www.google.nl/url?sa=t&q=esrc=s&source=web&cd=1&cad=rja&uact=8&ved=0ahUKEwjnq07zxJLSAhUJrRoKHR_{_}CCY4QFggcMAA&url=http%3A%2F%2Fwww.hexcel.com%2FResources%2FDataSheets%2FPreg-Data-Sheets%2F8552_{_}eu.pdf&usg=AFQjCNGt5LSVqsFNwxr7dRNqRM-CMR2nkw&{&})
- Robert D. Cook, David S. Malkus, Michael E. Plesha, and Robert J. Witt Witt. *Concept and Applications of Finite Element Analysis*. 2002. ISBN 978-0-471-35605-9.
- Roeland De Breuker. *Energy-based Aeroelastic Analysis and Optimisation of Morphing Wings*. Phd, TU Delft, 2011.
- L. Demasi and E. Livne. Aeroelastic coupling of geometrically nonlinear structures and linear unsteady aerodynamics: Two formulations. *Journal of Fluids and Structures*, 25(5):918–935, 2009. ISSN 08899746. doi: 10.1016/j.jfluidstructs.2009.03.001.
- C. G. Diaconu, M. Sato, and H. Sekine. Feasible region in general design space of lamination parameters for laminated composites. *AIAA Journal*, 40(3):559–565, 2002. ISSN 0001-1452. doi: 10.2514/3.15097.
- F. E. Eastep, V. a. Tischler, V. B. Venkayya, and N. S. Khot. Aeroelastic Tailoring of Composite Structures. *Journal of Aircraft*, 36(6):1041–1047, 1999. ISSN 0021-8669. doi: 10.2514/2.2546.
- G.A. Georghiades and J.R. Banerjee. Flutter modes of composite wings exhibiting wash-in and wash-out. *Collection of Technical Papers - AIAA/ASME/ASCE/AHS/ASC Structures, Structural Dynamics and Materials Conference*, 1:749–758, 1997. ISSN 02734508. doi: 10.2514/6.1997-1267.
- F H Gern, E Sulaeman, R K Kapania, Aiaa Asme, Asce Ahs, April Atlanta, H Gern, and Amir H Naghshineh-pour. Flexible Wing Model for Structural Sizing and Multidisciplinary Design Optimization of a Strut-Braced Wing. In *41st AIAA/ASME/ASCE/AHS Structures, Structural Dynamics, and Materials Meeting & Exhibit*, number April, Atlanta, 2000a.
- Frank Gern, Andy Ko, Erwin Sulaeman, Rakesh Kapania, William Mason, Bernard Grossman, and Raphael Haftka. Passive load alleviation in the design of a strut-braced wing transonic transport aircraft. In *8th Symposium on Multidisciplinary Analysis and Optimization*, number c, Long Beach, CA, 2000b. doi: 10.2514/6.2000-4826.
- Frank Gern, Andy Ko, Bernard Grossman, Rafael Haftka, Rakesh Kapania, William Mason, and Joseph Schetz. Transport Weight Reduction Through MDO: The Strut-Braced Wing Transonic Transport. In *35th AIAA Fluid Dynamics Conference and Exhibit*, Toronto, 2005. ISBN 978-1-62410-059-8. doi: 10.2514/6.2005-4667.
- Frank H. Gern, Andy Ko, Erwin Sulaeman, John F. Gundlach, Rakesh K. Kapania, and Raphael T. Haftka. Multidisciplinary Design Optimization of a Transonic Commercial Transport with Strut-Braced Wing. In *World Aviation Conference*, volume 38, pages 1006–1014, San Francisco, CA, 1999. ISBN 0021-8669. doi: 10.2514/2.2887.

- Frank H. Gern, Amir H. Naghshineh-Pour, Erwin Sulaeman, Rakesh K. Kapania, and Raphael T. Haftka. Structural Wing Sizing for Multidisciplinary Design Optimization of a Strut-Braced Wing. *Journal of Aircraft*, 38(1):154–163, 2001. ISSN 0021-8669. doi: 10.2514/2.2747.
- M Goland. The Flutter of a Uniform Cantilevered Wing. *Journal of Applied Mechanics*, 12(4):{A}197—{A}208, 1945.
- Joel M Grasmeyer. *Multidisciplinary Design Optimization of a Strut-Braced Wing Aircraft*. Msc, Virginia Polytechnic Institute and State University, 1998.
- O Gur, M Bhatia, J A Schetz, W H Mason, R K Kapania, and D N Mavris. Design optimization of a truss-braced-wing transonic transport aircraft. *Journal of Aircraft*, 47(6):1907–1917, 2010. ISSN 0021-8669. doi: 10.2514/1.47546.
- V.B. Hammer, M.P. Bendsøe, R. Lipton, and P. Pedersen. Parametrization in laminate design for optimal compliance. *International Journal of Solids and Structures*, 34(4):415–434, 1997. ISSN 00207683. doi: 10.1016/S0020-7683(96)00023-6.
- T. J. Hertz, M. H. Shirk, R. H. Ricketts, and T. A. Weisshaar. Aeroelastic Tailoring with Composites Applied to Forward Swept Wings. nov 1981.
- M. Hurel. The Advantages of High Aspect Ratios. *Interavia*, 7(12):695–699, 1952.
- Masaki Kameyama and Hisao Fukunaga. Optimum design of composite plate wings for aeroelastic characteristics using lamination parameters. *Computers and Structures*, 85(3-4):213–224, 2007. ISSN 00457949. doi: 10.1016/j.compstruc.2006.08.051.
- Christos Kassapoglou. *Design and Analysis of Composite Structures*. John Wiley & Sons Ltd., first edition, 2010. ISBN 9780470972700. doi: 10.1002/9780470972700.
- Robert M. Kulfan and John D. Vachal. Wing Planform Geometry Effects on Large Subsonic Military Transport Airplanes. Technical report, Boeing Commercial Airplane Company, Seattle, WA, 1978.
- E Livne. Aeroelasticity of Joined-Wing Airplane Configurations: Past Work and Future Challenges- A Survey. In *42nd AIAA/ASME/ASCE/AHS/ASC Structures, Structural Dynamics, and Materials Conference*, number April, Seattle, WA, 2001. doi: AIAA-2001-1370.
- E. Livne and Terrence a. Weisshaar. Aeroelasticity of Nonconventional Airplane Configurations-Past and Future. *Journal of Aircraft*, 40(6):1047–1065, 2003. ISSN 0021-8669. doi: 10.2514/2.7217.
- Wrik Mallik, Rakesh K. Kapania, and Joseph A. Schetz. Multidisciplinary Design Optimization of Medium-Range Transonic Truss-Braced Wing Aircraft with Flutter Constraint. In *54th AIAA/ASME/ASCE/AHS/ASC Structures, Structural Dynamics, and Materials Conference*, Boston, 2013. ISBN 978-1-62410-223-3. doi: 10.2514/6.2013-1454.
- Wrik Mallik, Rakesh K Kapania, and Joseph A Schetz. Effect of Flutter on the Multidisciplinary Design Optimization of Truss-Braced-Wing Aircraft. *Journal of Aircraft*, 52(6):1858–1872, 2015. doi: 10.2514/1.C033096.
- Nicholas A. Meadows, Joseph A. Schetz, Rakesh K. Kapania, Manav Bhatia, and Guclu Seber. Multidisciplinary Design Optimization of Medium-Range Transonic Truss-Braced Wing Aircraft Transport Aircraft. *Journal of Aircraft*, 49(6):1844–1856, 2012. ISSN 0021-8669. doi: 10.2514/6.2013-1454.
- MSC Software Corporation. *MSC Nastran 2016 Dynamic Analysis User's Guide*. MSC Software Corporation, Newport, 2016a. ISBN 0369111222.
- MSC Software Corporation. *MSC Nastran 2016 Quick Reference Guide*. MSC Software Corporation, Newport Beach, CA, 2016b. ISBN 0369111222.
- Amir H Naghshineh-pour. *Structural Optimization and Design of a Strut-Braced Wing Aircraft*. Msc, Virginia Polytechnic Institute and State University, 1998.

- Taewoo Nam, Imon Chakraborty, Jonathan Gross, Dimitri N Mavris, Joseph A Schetz, and Rakesh K Kapania. Multidisciplinary Design Optimization of a Truss-Braced Wing Concept. In *14th AIAA Aviation Technology, Integration, and Operations Conference*, number June, Atlanta, GA, 2014. ISBN 9781624102820. doi: 10.2514/6.2014-2423.
- M. J. Patil and Dewey H. Hodges. On the importance of aerodynamic and structural geometrical nonlinearities in aeroelastic behavior of high-aspect-ratio wings. *Journal of Fluids and Structures*, 19(7):905–915, 2004. ISSN 08899746. doi: 10.1016/j.jfluidstructs.2004.04.012.
- Mayuresh J Patil, Dewey H Hodges, and Carlos E S Cesnik. Characterizing the Effects of Geometrical Nonlinearities on Aeroelastic Behavior of High-Aspect-Ratio Wings. *International Forum on Aeroelasticity and Structural Dynamics, Williamsburg, Virginia, USA, June 22 - 25, 1999*, pages 1–10, 1999.
- Mayuresh J. Patil, Dewey H. Hodges, and Carlos E. S. Cesnik. Nonlinear Aeroelastic Analysis of Complete Aircraft in Subsonic Flow. *Journal of Aircraft*, 37(5):753–760, sep 2000. ISSN 0021-8669. doi: 10.2514/2.2685.
- M.J.a Patil, D.H.a Hodges, and C.E.S.b Cesnik. Nonlinear Aeroelasticity and Flight Dynamics of High-Altitude Long-Endurance Aircraft. *Journal of Aircraft*, 38(1):88–94, 2001. ISSN 0021-8669. doi: 10.2514/2.2738.
- W. Pfenninger. Laminar flow control laminarization. In *AGARD Spec. Course on Concepts for Drag Reduction*, jun 1977.
- Werner Pfenninger and Chandra S. Vemuru. Design aspects of long range supersonic LFC airplanes with highly swept wings. In *Aerospace Technology Conference and Exposition*, pages 87–100, Anaheim, California, 1988. ISBN <http://ntrs.nasa.gov/search.jsp?R=19890063986>.
- Robert C Scott, Timothy Allen, Mark Castelluccio, Bradley Sexton, Scott Claggett, John R Dykman, Christie Funk, David Coulson, and Robert E Bartels. Aerovielastic Wind-Tunnel Test of the SUGAR Truss Braced Wing Wind-Tunnel Model. In *56th AIAA/ASCE/AHS/ASC Structures, Structural Dynamics, and Materials Conference*, number January. AIAA SciTech, Kissimmee, FL, 2015. ISBN 9781624103421. doi: doi:10.2514/6.2015-1172.
- Guclu Seber, Hongjun Ran, Joseph A Schetz, and Dimitri N Mavris. Multidisciplinary Design Optimization of a Truss Braced Wing Aircraft with Upgraded Aerodynamic Analyses. In *29th AIAA Applied Aerodynamics Conference*, number June, pages 1–15, Honolulu, 2011. ISBN 9781624101458.
- Shahriar Setoodeh, Mostafa M. Abdalla, and Zafer Gürdal. Approximate feasible regions for lamination parameters. *{Collection of Technical Papers - 11th AIAA/ISSMO Multidisciplinary Analysis and Optimization Conference}*, 2(September):814–822, 2006. ISSN 13598368. doi: 10.1016/j.compositesb.2005.12.001.
- Michael H. Shirk, Terrence J. Hertz, and Terrence A. Weisshaar. AEROELASTIC TAILORING - THEORY, PRACTICE, AND PROMISE. *Journal of Aircraft*, 23(1):6–18, 1986. ISSN 00218669.
- P.M. Smith, J. Deyoung, W.A. Lovell, J.E. Price, and G.F. Washburn. A study of High-Altitude Manned Research Aircraft Employing Strut-Braced Wings of High-Aspect Ratio. Technical Report February 1981, NASA Langley Research Center, Hampton, Virginia, 1981.
- Erwin Sulaeman, Rakesh Kapania, and Raphael Haftka. Parametric Studies of Flutter Speed in a Strut-Braced Wing. In *43rd AIAA/ASME/ASCE/AHS/ASC Structures, Structural Dynamics, and Materials Conference*, number April, Denver, Colorado, 2002. ISBN 978-1-62410-117-5. doi: 10.2514/6.2002-1487.
- Erwin Sulaeman, Rakesh Kapania, and Raphael Haftka. Effect of Compressive Force on Flutter Speed of a Strut-Braced Wing. In *44th AIAA/ASME/ASCE/AHS Structures, Structural Dynamics, and Materials Conference*, number April, Norfolk, Virginia, 2003. ISBN 978-1-62410-117-5. doi: 10.2514/6.2002-1487.
- Theplasticshop.co.uk. Perspex Cell Cast Acrylic Technical Data Sheet. URL https://www.theplasticshop.co.uk/plastic{_}technical{_}data{_}sheets/_perspex{_}technical{_}properties{_}data{_}sheet.pdf.
- Faculteit Luchtvaart-& Ruimtevaarttechniek TU Delft. DASML Equipment. URL <https://www.tudelft.nl/lr/organisatie/afdelingen/dasml/equipment/>.

- R.V. Turriziani, W.A. Lovell, G.L. Martin, J.E. Price, E.E. Swanson, and G.F. Washburn. Preliminary Design Characteristics of a Subsonic Business Jet Concept Employing an Aspect Ratio 25 Strut-Braced Wing. Technical report, NASA Langley Research Center, Hampton, Virginia, 1980.
- Johan Visschedijk. Johan Visschedijk Collection, 2008. URL <http://1000aircraftphotos.com/Contributions/Visschedijk/8394.htm>.
- Guangqiu Wang, Jie Zeng, Jen-Der Lee, Xi Du, and Xiaowen Shan. Preliminary Design of a Truss-Braced Natural-Laminar-Flow Composite Wing via Aeroelastic Tailoring. *ASDJournal*, 3(3):1–17, 2015. doi: 10.3293/asdj.2015.36.
- Terrence Weisshaar and D-H. Lee. Aeroelastic Tailoring of Joined-Wing Configurations. In *43rd AIAA/ASME/ASCE/AHS/ASC Structures, Structural Dynamics, and Materials Conference*, number April, Denver, CO, 2002. ISBN 978-1-62410-117-5. doi: 10.2514/6.2002-1207.
- Terrence A. Weisshaar. Aeroelastic tailoring - Creative uses of unusual materials. *AIAA/ASME/ASCE/AHS 28th Structures, Structural Dynamics and Materials Conference, Monterey, California, April 6-8, 1987*, 1987. doi: doi:10.2514/6.1987-976.
- Noud Werter. *An Advanced Aeroelastic Tailoring Tool for Wing Optimisation*. Msc, TU Delft, 2012.
- Noud P M Werter and Roeland De Breuker. Aeroelastic Tailoring and Structural Optimisation using an Advanced Dynamic Aeroelastic Framework. In *IFASD 2015: 16th International Forum on Aeroelasticity and Structural Dynamics*, Sint Petersburg, Russia, 2015.
- Edward V White. Novel Control Effectors for Truss Braced Wing. Technical Report August, 2015.
- Wei Zhao, Rakesh K Kapania, Joseph A Schetz, John M Coggin, Timothy J. Allen, and Bradley W. Sexton. Nonlinear Aeroelastic Analysis of SUGAR Truss-braced Wing (TBW) Wind-tunnel Model (WTM) Under In-plane Loads. In *56th AIAA/ASCE/AHS/ASC Structures, Structural Dynamics, and Materials Conference*, number January, pages 1–22, Kissimmee, FL, 2015. AIAA SciTech. ISBN 978-1-62410-342-1. doi: doi:10.2514/6.2015-1173.



Summary of optimization settings

By means of tables A.1 to A.4 a clear overview is given for all optimization settings that were applied for the present thesis work. A discussion of the presented settings was provided in chapter 6.

A.1. Fixed model parameters

The parameters listed in table A.1 will remain fixed for all SBW configurations. The table summarizes all that was discussed in section 6.2.

Table A.1: Geometric parameters of SBW model

Geometric parameter	Parameter	Justification
Half span $b[m]$	1.5	Max. dimension of TUD autoclave is 1.7 m
Chord length $c[m]$	0.155	For obtaining desired aspect ratio
Aspect ratio [-]	19.35	AR of Boeing SUGAR SBW is 19.55
Airfoil	NACA0012	Scaled fuselage height based on SUGAR SBW
Vertical strut location $z_{strut}[m]$	-0.25	Provide thickness for inner structure
Wing box modelling %c	25-75	For limited amount of required cross-sectional elements
Spar locations %c	25,75	For limited amount of required cross-sectional elements

The resulting cross-section of the untailored wings is depicted in figure A.1, including the initial locations of shear center and center of gravity.

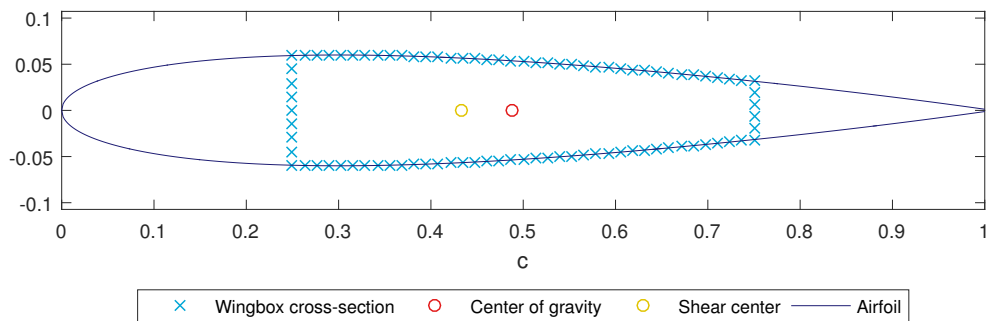


Figure A.1: Wing cross-section typical for all SBW configurations before tailoring

A.2. Modelling parameters

Table A.2 summarizes the conclusions of section 6.3.

Table A.2: Modelling parameter for SBW model

Modelling parameter	Amount	Justification
Nr. spanwise laminates	5	Ease of future manufacturing
Nr. chordwise laminates	1	Very small chord length
Nr. of beam elements	10	Convergence study result
Nr. of spanwise aerodynamic panels	15	Convergence study result
Nr. of chordwise aerodynamic panels	4	Convergence study result
Length of wake [c]	10	see section 6.3.3
Nr. of wake panels per c	2	see section 6.3.3
Nr. of cross-sectional elements	75	Minimum required for given
cross-section Minimum laminate thickness	t_{ply}	Ply thickness of AS4/8552 composite
material Maximum laminate thickness	$40*t_{ply}$	-

A.3. Proteus inputs

The remaining inputs required to start an aeroelastic tailoring procedure in Proteus are listed in table A.3.

Table A.3: Other Proteus inputs

Input	Entry	Remarks
Linear/nonlinear	0	Nonlinear analysis
Weight definition	1	-
Derivative	0	-
Gravity	0	-
Optimiser	GCMMA	-
Analysis	1	Classical analysis
Objective	1	Weight minimizations
Angle of attack limit	0	-
Blending constraints	0	-
Aileron effectiveness	0	-
Buckling	1	-
1g twist	0	-
Analysis type	1	Aeroelastic tailoring

A.4. Load case data

Section 6.5 explained how the inputs for application the governing static maneuver loads were derived. Table A.4 lists all data required for the load input section in the Proteus input file.

Table A.4: Load case parameters

Load parameter	Entry	Justification
Mach number [-]	0.1	For $EAS = 25 m/s$ at sea level
EAS [m/s]	25	Maximum operation speed OJF TU Delft
Altitude [m]	0	Sea level conditions
Load factor [-]	1	Load factor is regulated by angle of attack
Gust	0	-
Trim	0	No aircraft weight data available for SBW model
Angle of attack [$^\circ$]	8.9, -3.5	see section 6.5

B

Additional results of configuration parameter study

A selection from the complete set of results of the configuration parameter study was already discussed in section 6.6. This appendix includes all other figures from the set of results that support the conclusions drawn in section 6.6.

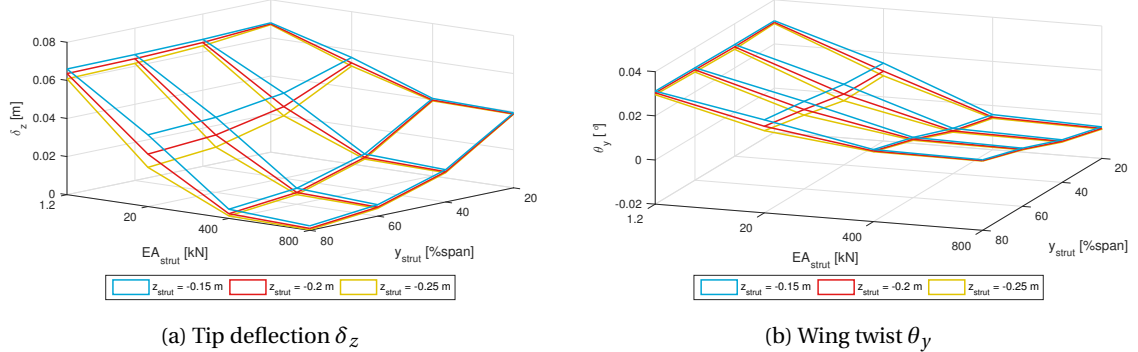


Figure B.1: Parameter study results on wing tip deformation for variable y_{strut} , z_{strut} and EA_{strut} , and $x_{strut} = 25\%c$

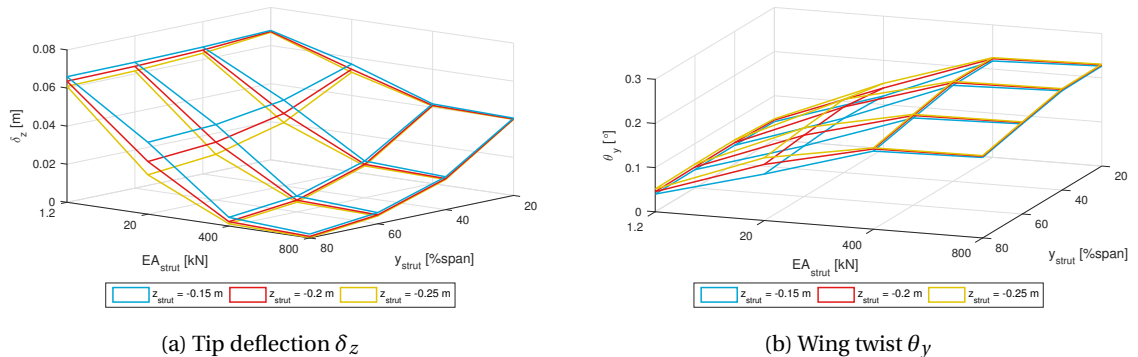


Figure B.2: Parameter study results on wing tip deformation for variable y_{strut} , z_{strut} and EA_{strut} , and $x_{strut} = 50\%c$

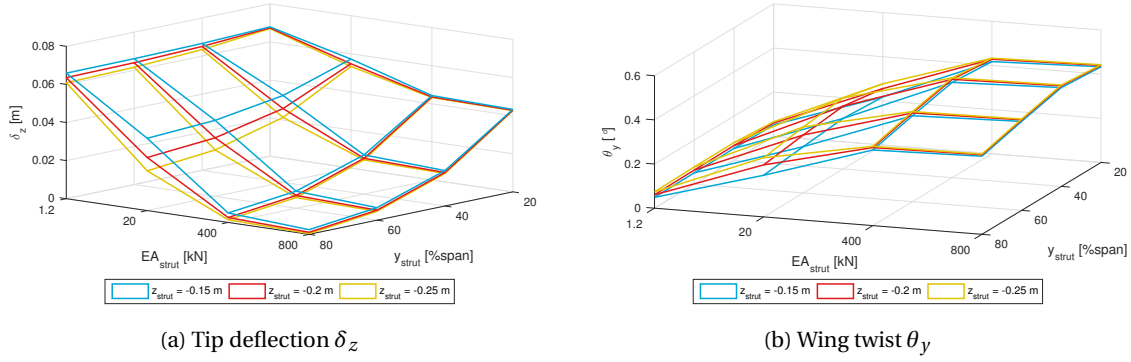


Figure B.3: Parameter study results on wing tip deformation for variable y_{strut} , z_{strut} and EA_{strut} , and $x_{strut} = 75\%c$

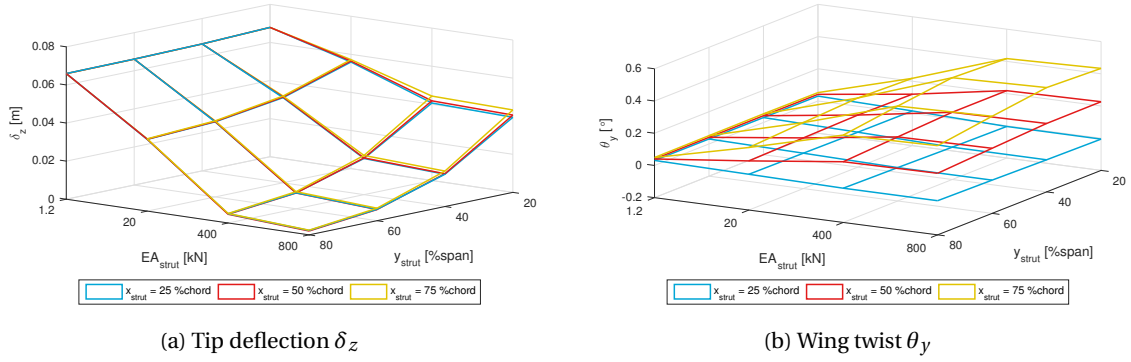


Figure B.4: Parameter study results on wing tip deformation for variable y_{strut} , x_{strut} and EA_{strut} , and $z_{strut} = -0.15m$

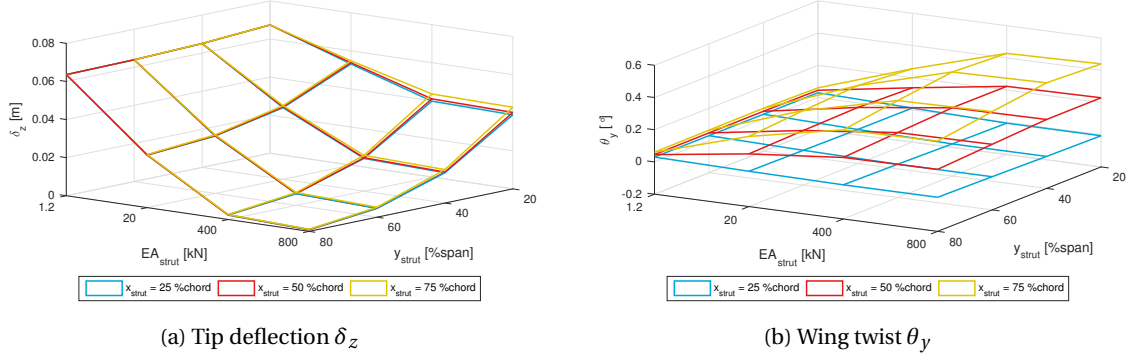


Figure B.5: Parameter study results on wing tip deformation for variable y_{strut} , x_{strut} and EA_{strut} , and $z_{strut} = -0.20m$

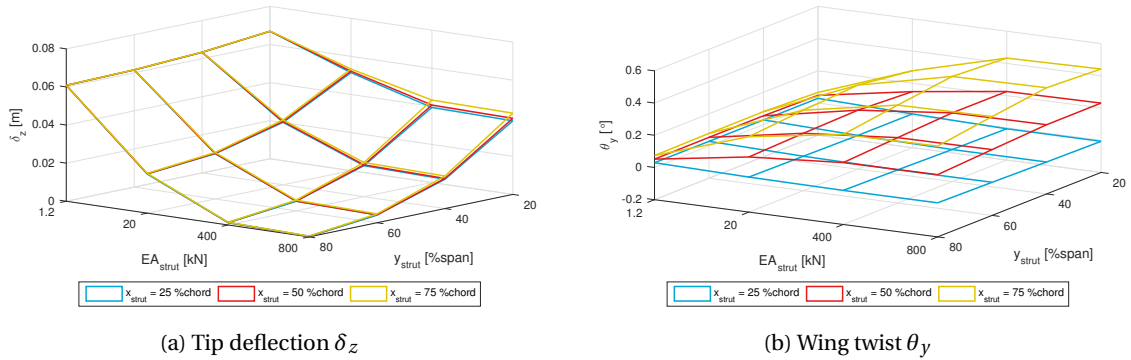
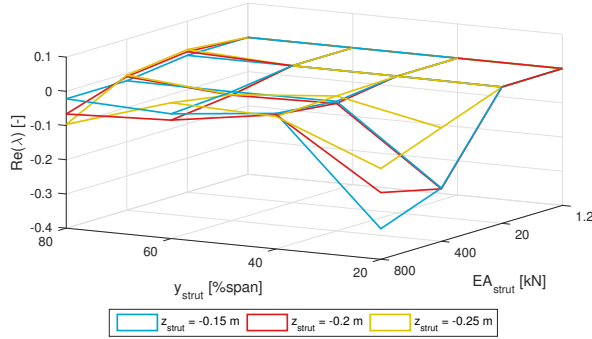
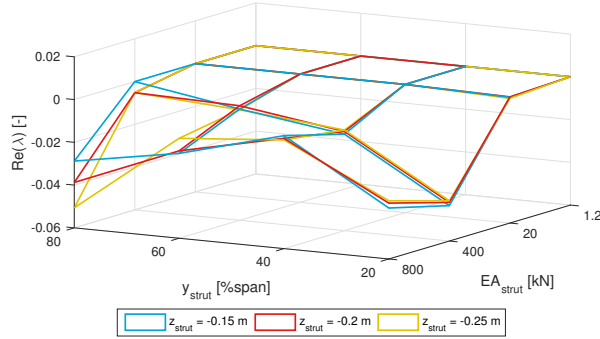
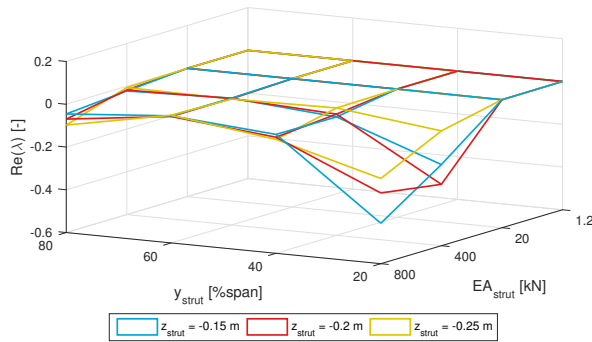


Figure B.6: Parameter study results on wing tip deformation for variable y_{strut} , x_{strut} and EA_{strut} , and $z_{strut} = -0.25m$

(a) $\text{Re}(\lambda)$ for variable y_{strut} , z_{strut} and EA_{strut} , and $x_{\text{strut}} = 25\%c$ (b) $\text{Re}(\lambda)$ for variable y_{strut} , z_{strut} and EA_{strut} , and $x_{\text{strut}} = 50\%c$ (c) $\text{Re}(\lambda)$ for variable y_{strut} , z_{strut} and EA_{strut} , and $x_{\text{strut}} = 75\%c$ Figure B.7: Parameter study results on real part of the most critical aeroelastic eigenvalue $\text{Re}(\lambda)$ for variable y_{strut} , z_{strut} and EA_{strut} , and fixed x_{strut}

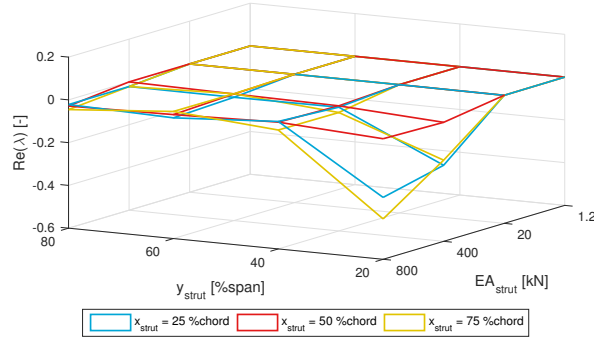
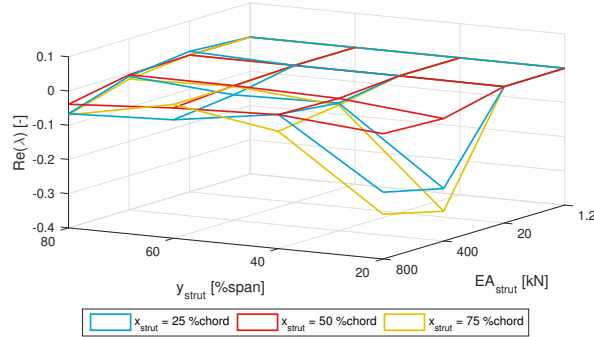
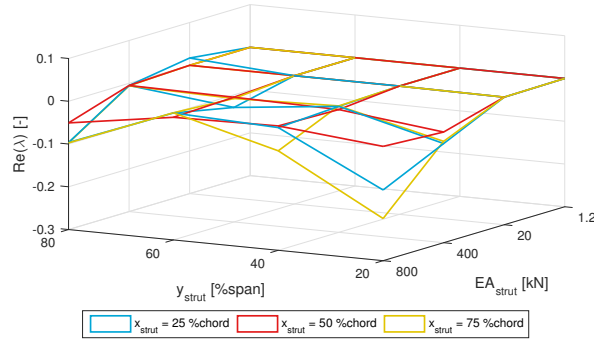
(a) $\text{Re}(\lambda)$ for $z_{\text{strut}} = -0.15m$ (b) $\text{Re}(\lambda)$ for $z_{\text{strut}} = -0.20m$ (c) $\text{Re}(\lambda)$ for $z_{\text{strut}} = -0.25m$

Figure B.8: Parameter study results on real part of the most critical aeroelastic eigenvalue $\text{Re}(\lambda)$ for variable y_{strut} , x_{strut} and EA_{strut} , and fixed z_{strut}

C

Additional results of advanced sensitivity study

A selection from the complete set of results of the advanced sensitivity study was already discussed in section 6.8. This appendix includes the additional figures that support the conclusions drawn in section 6.8.

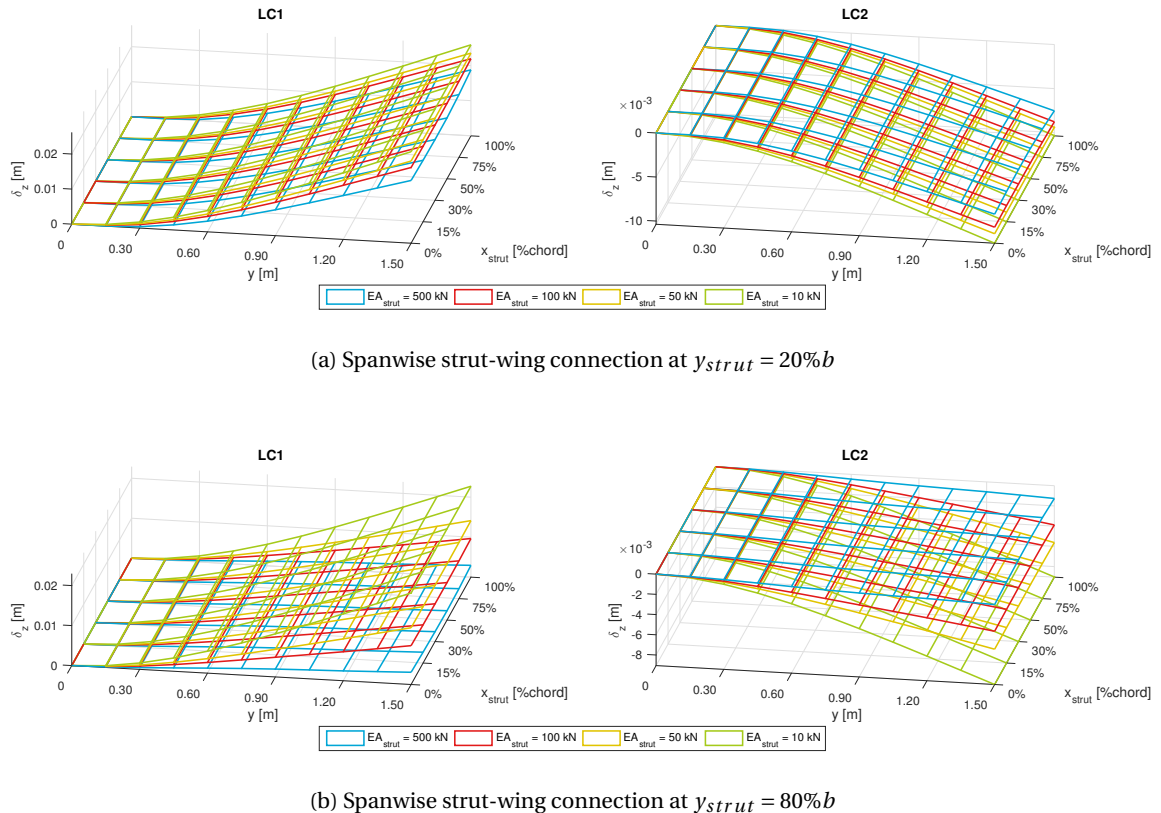
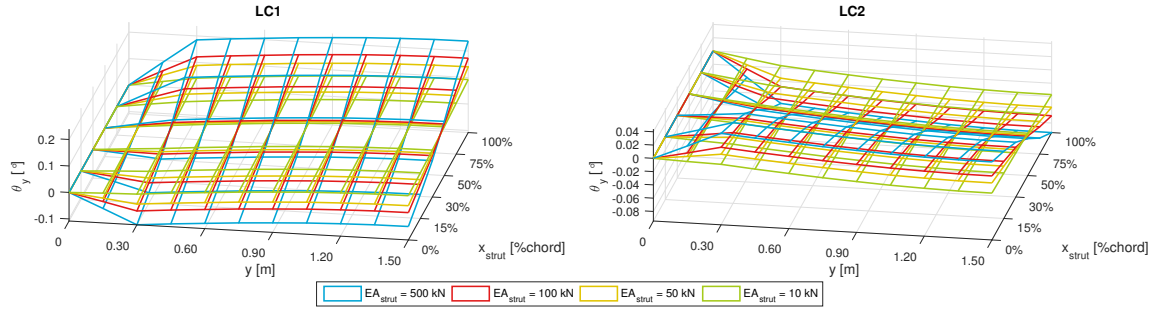
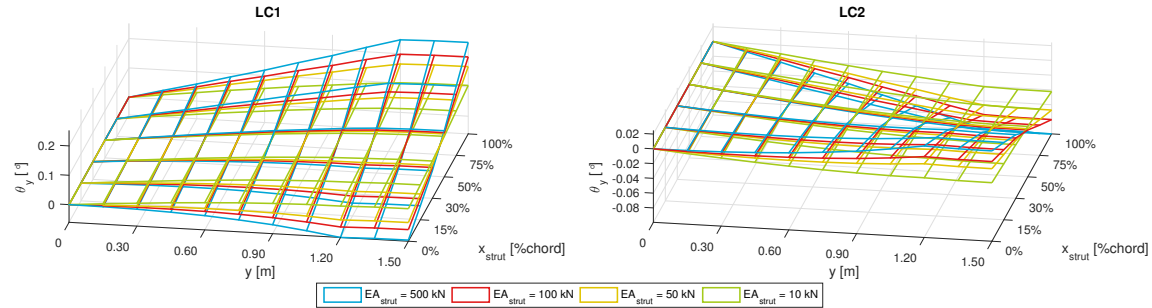


Figure C.1: Vertical wing displacement δ_z for initial SBW designs

(a) Spanwise strut-wing connection at $y_{strut} = 20\%b$ (b) Spanwise strut-wing connection at $y_{strut} = 80\%b$ Figure C.2: Wing twist θ_y for initial SBW designs

D

Aeroelastic tailoring results

This appendix provides the aeroelastic tailoring results of the SBW configurations that were not directly discussed in section 7.2. Figure D.1 presents the thickness and stiffness tailoring results for SBWs with $y_{strut} = 60\%b$ and a variation in EA_{strut} . Figure D.2 gives the same results for SBWs with $y_{strut} = 60\%b$ and a variation in x_{strut} .

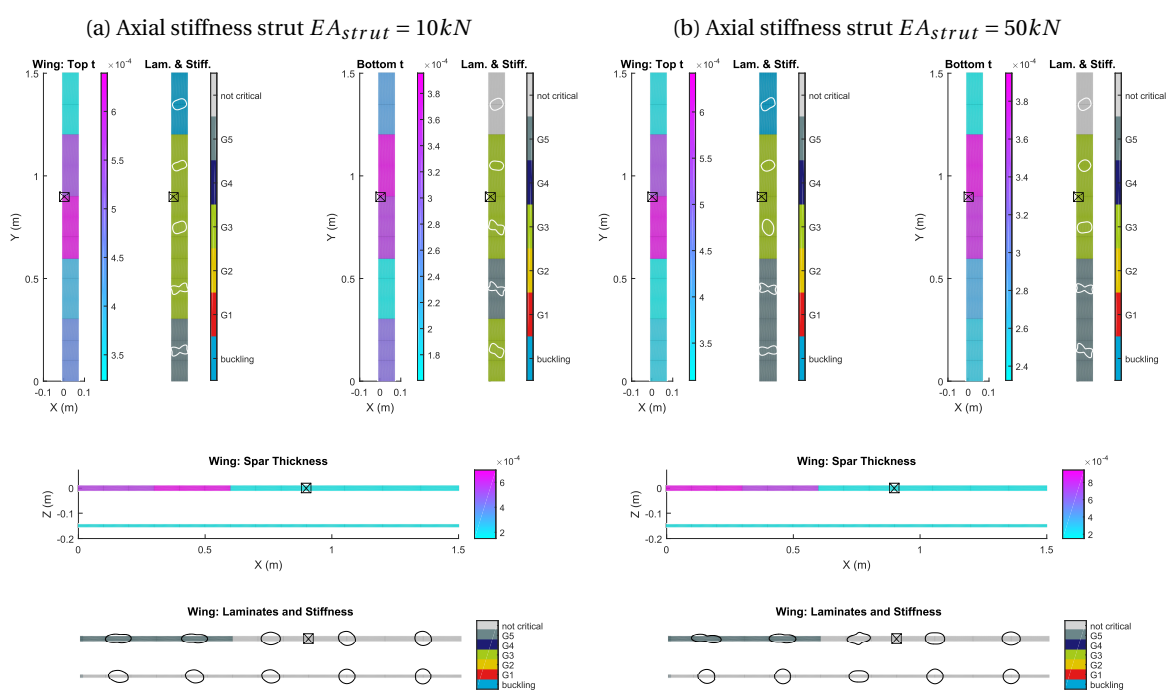
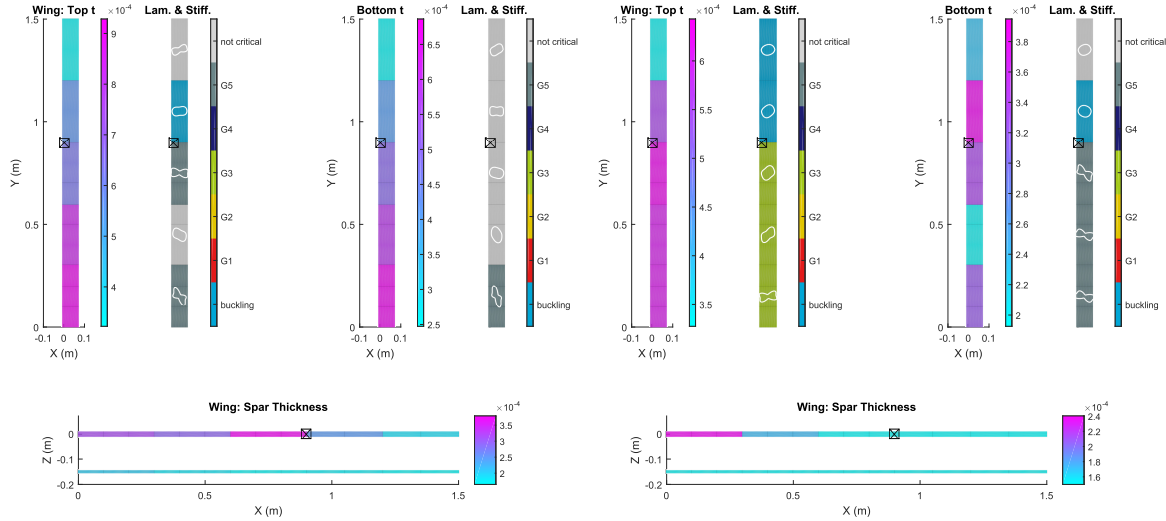


Figure D.1: Tailoring results for SBW configurations from subset A with $x_{strut} = 30\%c$ and $y_{strut} = 60\%b$

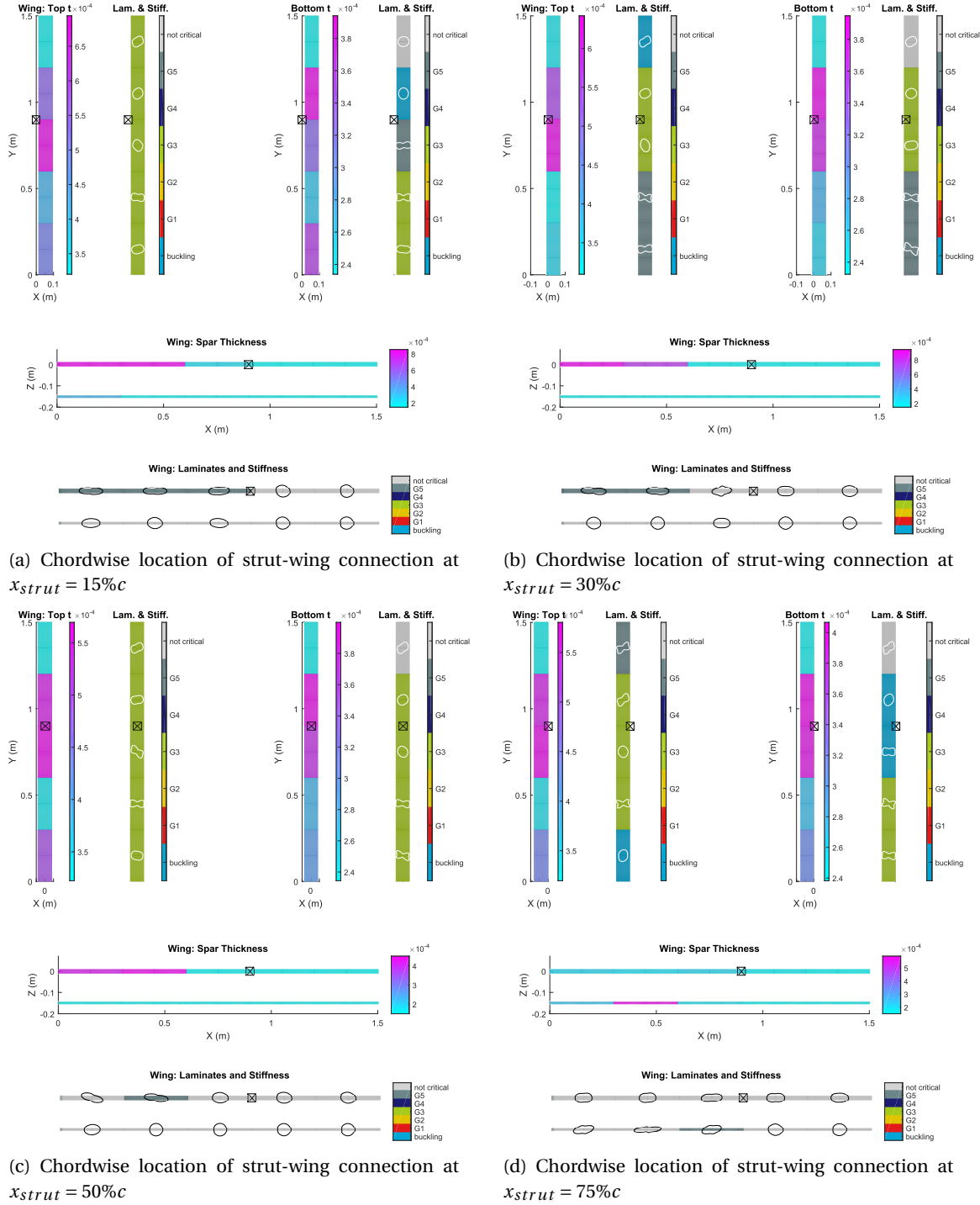
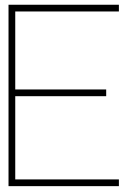


Figure D.2: Tailoring results for SBW configurations from subset B with $EA_{strut} = 500\text{ kN}$ and $y_{strut} = 60\%$



Static aeroelastic deflections of tailored SBWs

The figures in this appendix complete the set of static aeroelastic deflection results of the tailored SBW configurations that were discussed in section 7.2.2.

E.1. Wing deformation comparisons

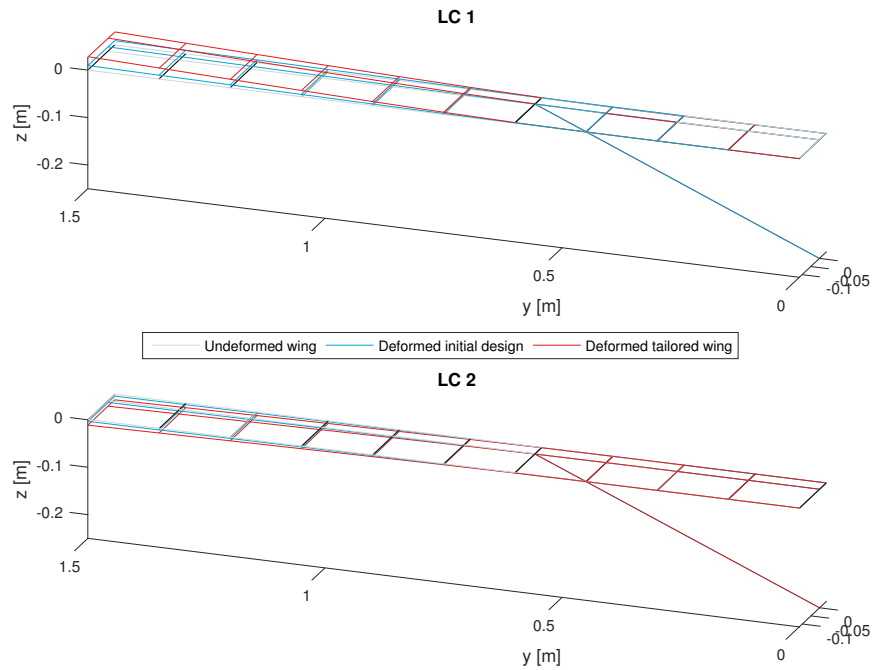
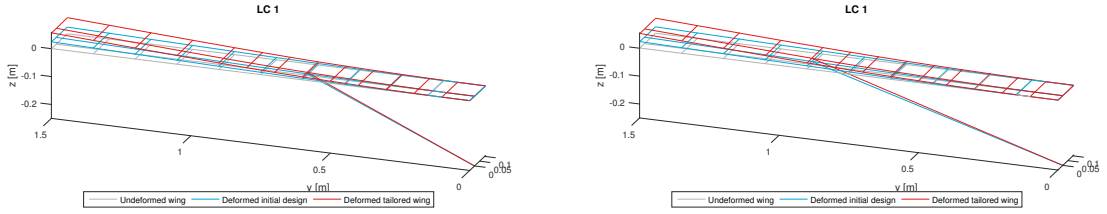


Figure E.1: Static aeroelastic deformation of SBW with $y_{strut} = 40\%b$, $x_{strut} = 75\%c$ and $EA_{strut} = 500kN$ for load case 1

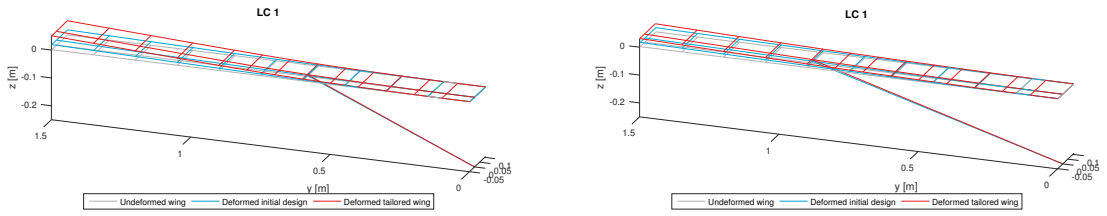
E.2. Deflection and wing twist plots per configuration subset

The plots in section compare the vertical wing deformation and wing twist results of the tailored SBWs to the untailored wings on a more quantified level. Section 7.2.2 already presented the results for the SBWs with $y_{strut} = 40\%b$ for subset A and B in figure 7.13 and 7.14. Figure E.7 and E.8 show the same results for the SBWs with $y_{strut} = 60\%b$.



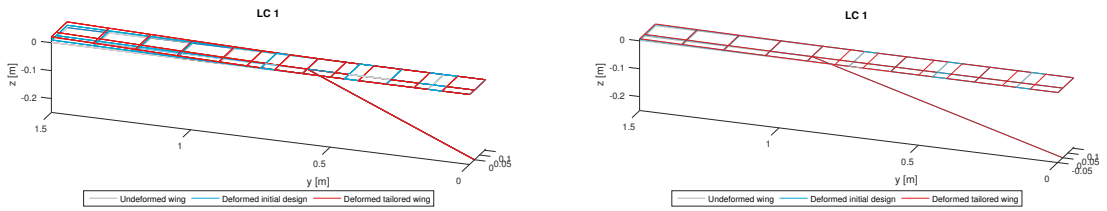
(a) Spanwise strut-wing connection at $y_{strut} = 40\%b$ (b) Spanwise strut-wing connection at $y_{strut} = 60\%b$

Figure E.2: Static aeroelastic deflection of SBW configurations with $x_{strut} = 30\%c$ and $EA_{strut} = 10kN$ for load case 1



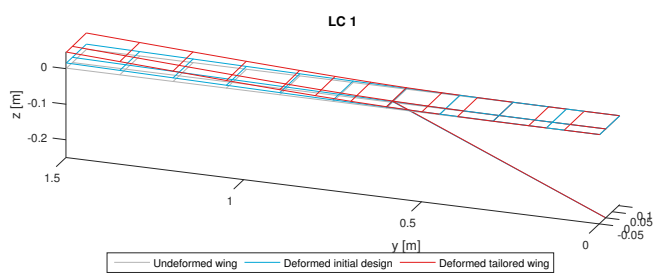
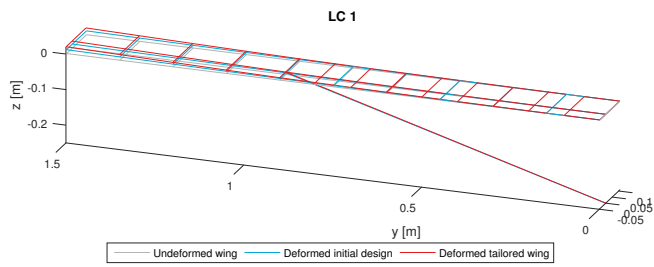
(a) Spanwise strut-wing connection at $y_{strut} = 40\%$ (b) Spanwise strut-wing connection at $y_{strut} = 60\%$

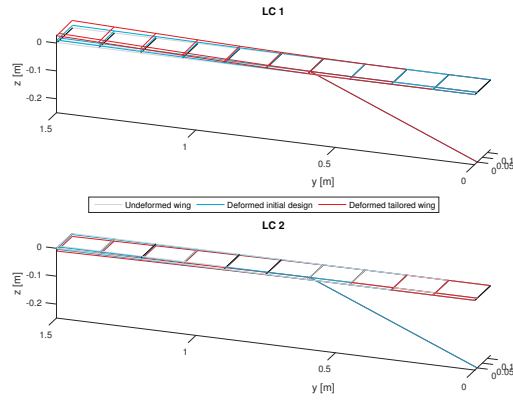
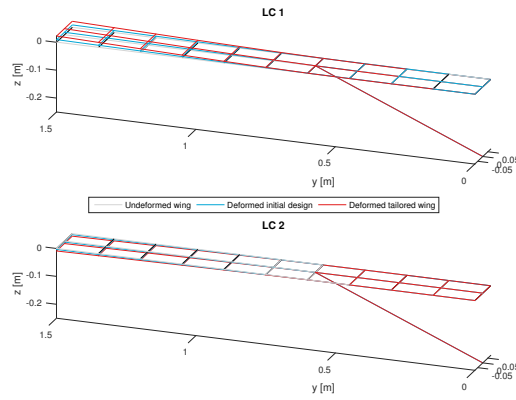
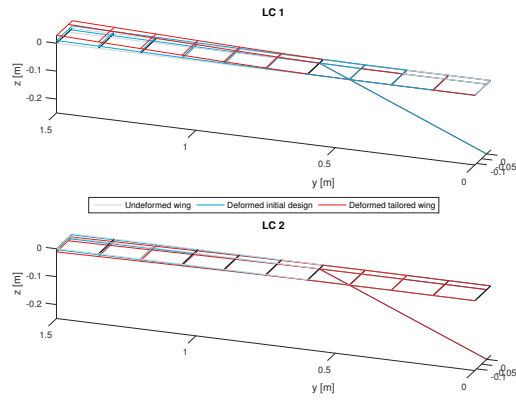
Figure E.3: Static aeroelastic deflection of SBW configurations with $x_{strut} = 30\%c$ and $EA_{strut} = 50kN$ for load case 1

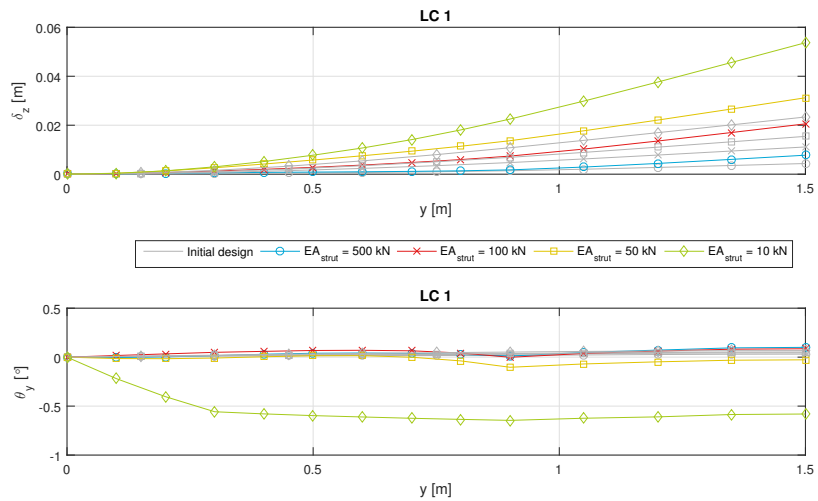
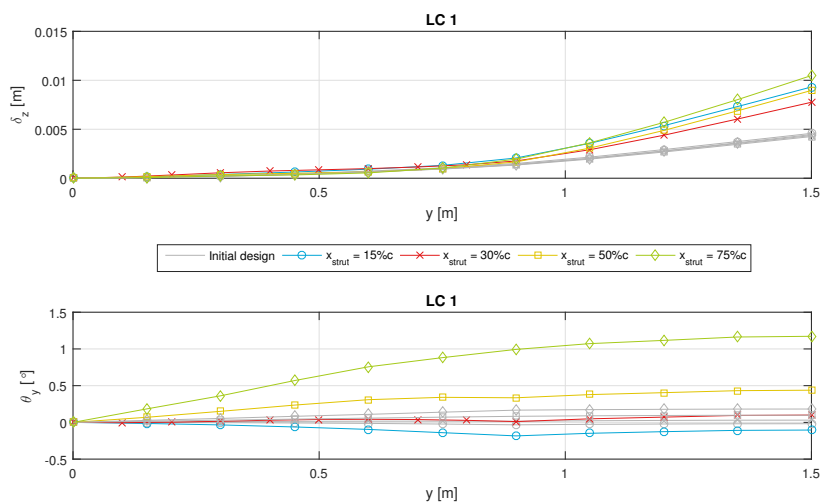


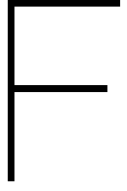
(a) Spanwise strut-wing connection at $y_{strut} = 40\%$ (b) Spanwise strut-wing connection at $y_{strut} = 60\%$

Figure E.4: Static aeroelastic deflection of SBW configurations with $x_{strut} = 30\%c$ and $EA_{strut} = 500kN$ for load case 2

(a) Spanwise strut-wing connection at $y_{strut} = 40\%$ (b) Spanwise strut-wing connection at $y_{strut} = 60\%$ Figure E.5: Static aeroelastic deflection for SBW configurations with $x_{strut} = 30\%c$ and $EA_{strut} = 100kN$

(a) Spanwise strut-wing connection at $x_{strut} = 15\%$ (b) Spanwise strut-wing connection at $x_{strut} = 50\%$ (c) Spanwise strut-wing connection at $x_{strut} = 75\%$ Figure E.6: Static aeroelastic deflection for SBW configurations with $y_{strut} = 40\%c$ and $EA_{strut} = 500kN$

Figure E.7: Static aeroelastic deformation of SBWs from subset A with $y_{strut} = 60\%b$ for load case 1Figure E.8: Static aeroelastic deformation of SBWs from subset B with $y_{strut} = 60\%b$ for load case 1



Isolated aeroelastic deflection and wing twist plots

The following plots present the same results as figures E.7 and E.8 in appendix E, but then for each of the fourteen tailored SBWs in a separate figure.

E.1. Subset A: Fixed $y_{strut} = 40\%b$, $x_{strut} = 30\%c$, and varying EA_{strut}

Figures E1 to E4 show the measurable results for the SBWs with $y_{strut} = 40\%b$, $x_{strut} = 30\%c$, and different values of EA_{strut} .

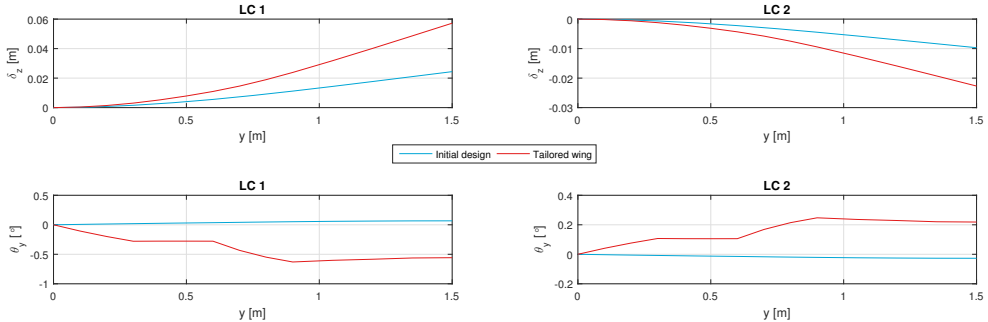


Figure E1: Comparison of δ_z and θ_y of untailored and tailored SBW with $y_{strut} = 40\%b$, $x_{strut} = 30\%c$, and $EA_{strut} = 10kN$

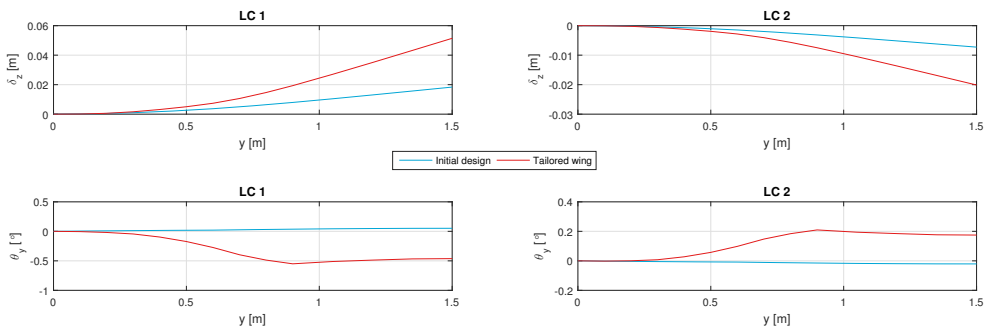


Figure E2: Comparison of δ_z and θ_y of untailored and tailored SBW with $y_{strut} = 40\%b$, $x_{strut} = 30\%c$, and $EA_{strut} = 50kN$

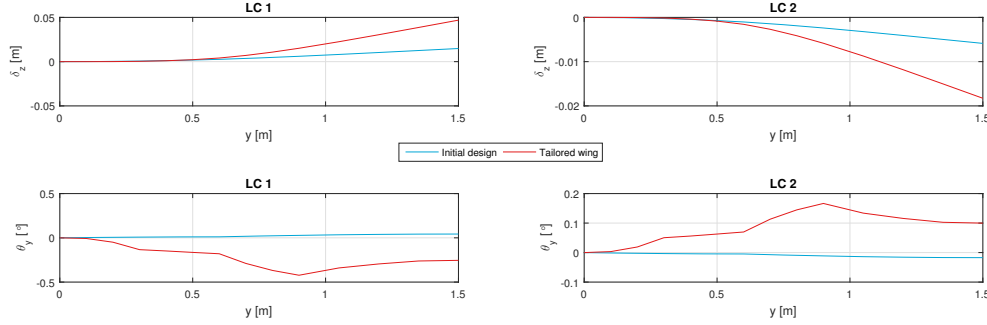


Figure E3: Comparison of δ_z and θ_y of untailored and tailored SBW with $y_{strut} = 40\%b$, $x_{strut} = 30\%c$, and $EA_{strut} = 100kN$

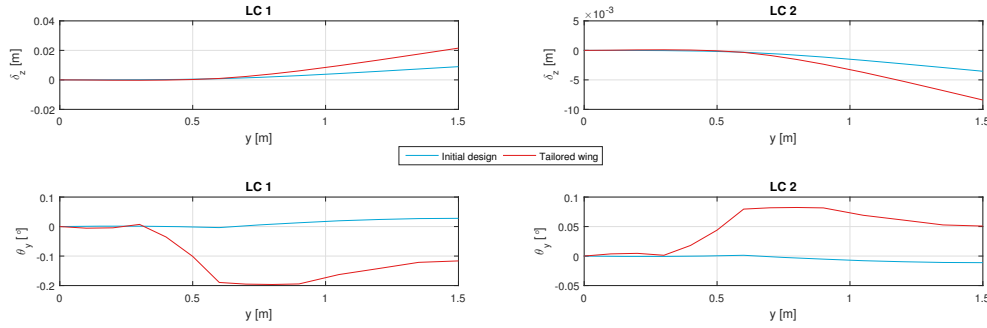


Figure E4: Comparison of δ_z and θ_y of untailored and tailored SBW with $y_{strut} = 40\%b$, $x_{strut} = 30\%c$, and $EA_{strut} = 500kN$

Figures E5 to E8 show the measurable results for the SBWs with $y_{strut} = 60\%b$, $x_{strut} = 30\%c$, and different values of EA_{strut} .

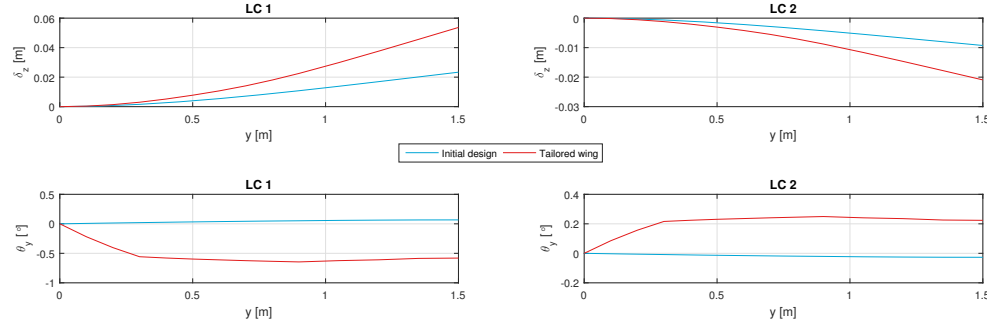


Figure E5: Comparison of δ_z and θ_y of untailored and tailored SBW with $y_{strut} = 60\%b$, $x_{strut} = 30\%c$, and $EA_{strut} = 10kN$

F.2. Subset B: Fixed EA_{strut} and y_{strut} , with varying x_{strut}

Figures E9 to E11 show the measurable results for the SBWs with $EA_{strut} = 500kN$, $y_{strut} = 40\%b$, and different values of x_{strut} .

Figures E12 to E14 show the measurable results for the SBWs with $EA_{strut} = 500kN$, $y_{strut} = 60\%b$, and different values of x_{strut} .

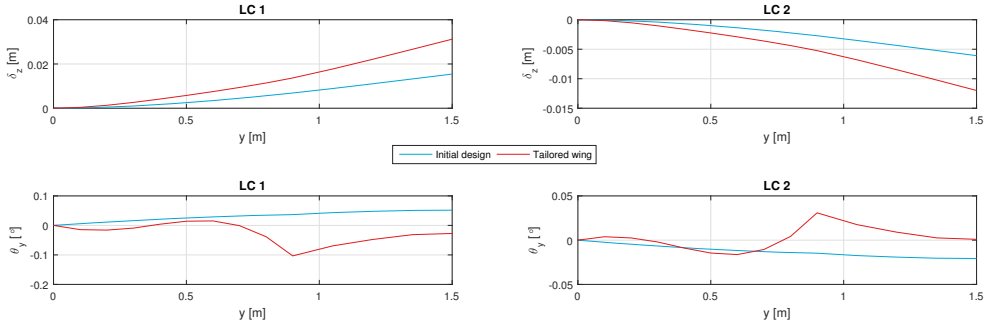


Figure F6: Comparison of δ_z and θ_y of untailored and tailored SBW with $y_{strut} = 60\%b$, $x_{strut} = 30\%c$, and $EA_{strut} = 50kN$

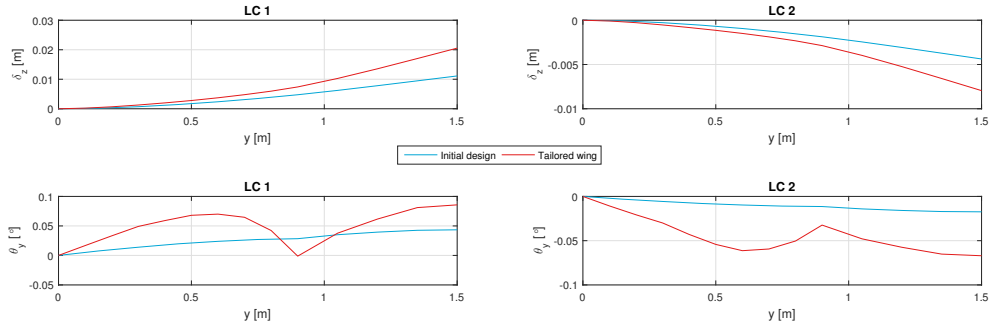


Figure F7: Comparison of δ_z and θ_y of untailored and tailored SBW with $y_{strut} = 60\%b$, $x_{strut} = 30\%c$, and $EA_{strut} = 100kN$

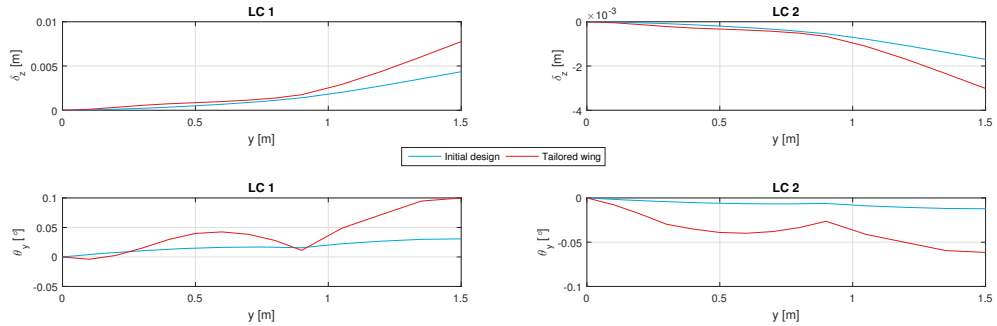


Figure F8: Comparison of δ_z and θ_y of untailored and tailored SBW with $y_{strut} = 60\%b$, $x_{strut} = 30\%c$, and $EA_{strut} = 500kN$

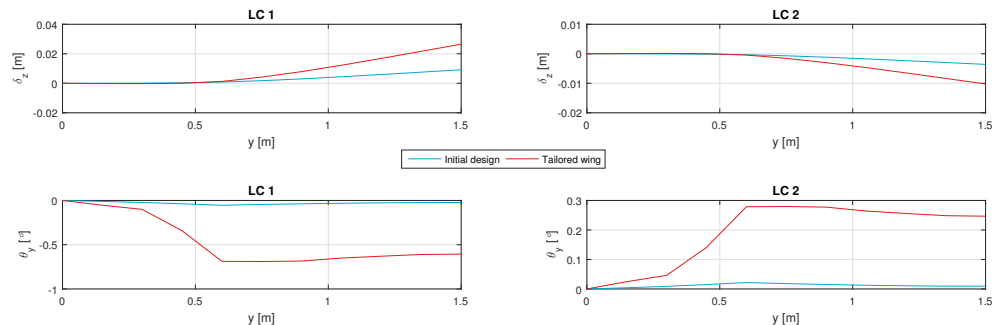


Figure F9: Comparison of δ_z and θ_y of untailored and tailored SBW with $y_{strut} = 40\%b$, $EA_{strut} = 500kN$, and $x_{strut} = 15\%c$

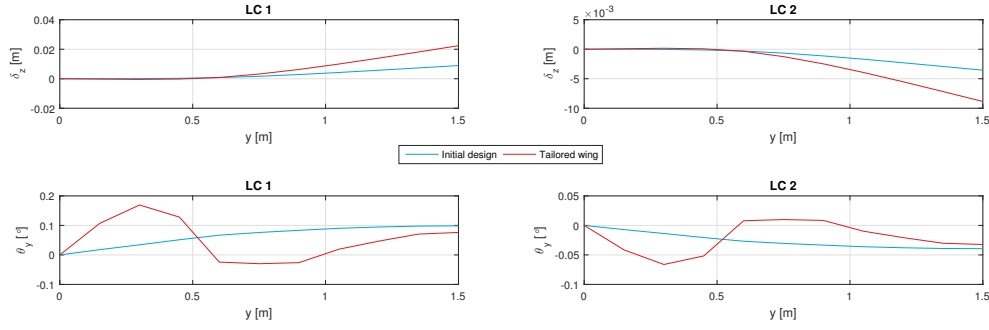


Figure E10: Comparison of δ_z and θ_y of untailored and tailored SBW with $y_{strut} = 40\%b$, $EA_{strut} = 500kN$, and $x_{strut} = 50\%c$

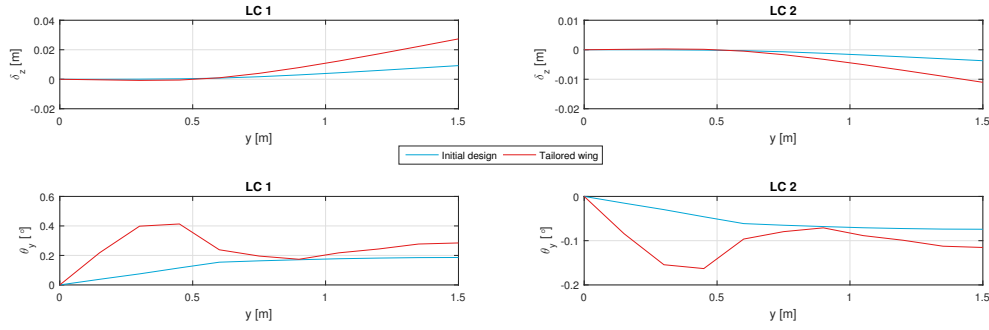


Figure E11: Comparison of δ_z and θ_y of untailored and tailored SBW with $y_{strut} = 40\%b$, $EA_{strut} = 500kN$, and $x_{strut} = 75\%c$

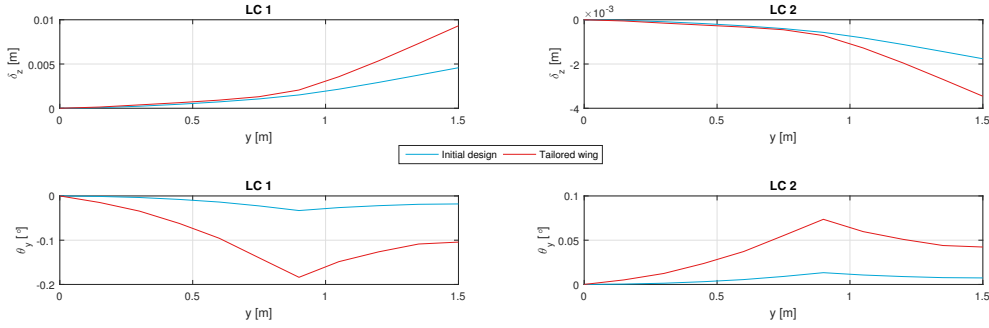


Figure E12: Comparison of δ_z and θ_y of untailored and tailored SBW with $y_{strut} = 60\%b$, $EA_{strut} = 500kN$, and $x_{strut} = 15\%c$

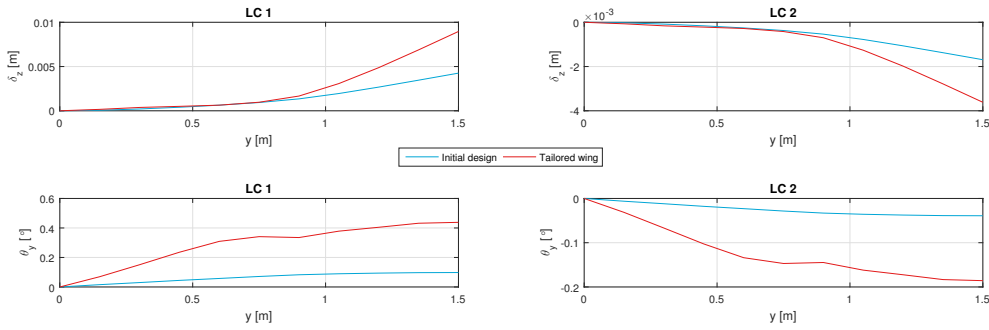


Figure E13: Comparison of δ_z and θ_y of untailored and tailored SBW with $y_{strut} = 60\%b$, $EA_{strut} = 500kN$, and $x_{strut} = 50\%c$

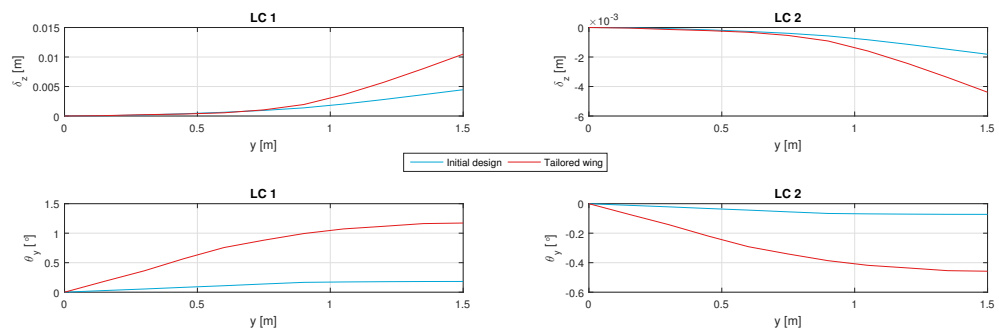


Figure E14: Comparison of δ_z and θ_y of untailored and tailored SBW with $y_{strut} = 60\%b$, $EA_{strut} = 500kN$, and $x_{strut} = 75\%c$

G

Most critical aeroelastic eigenmodes

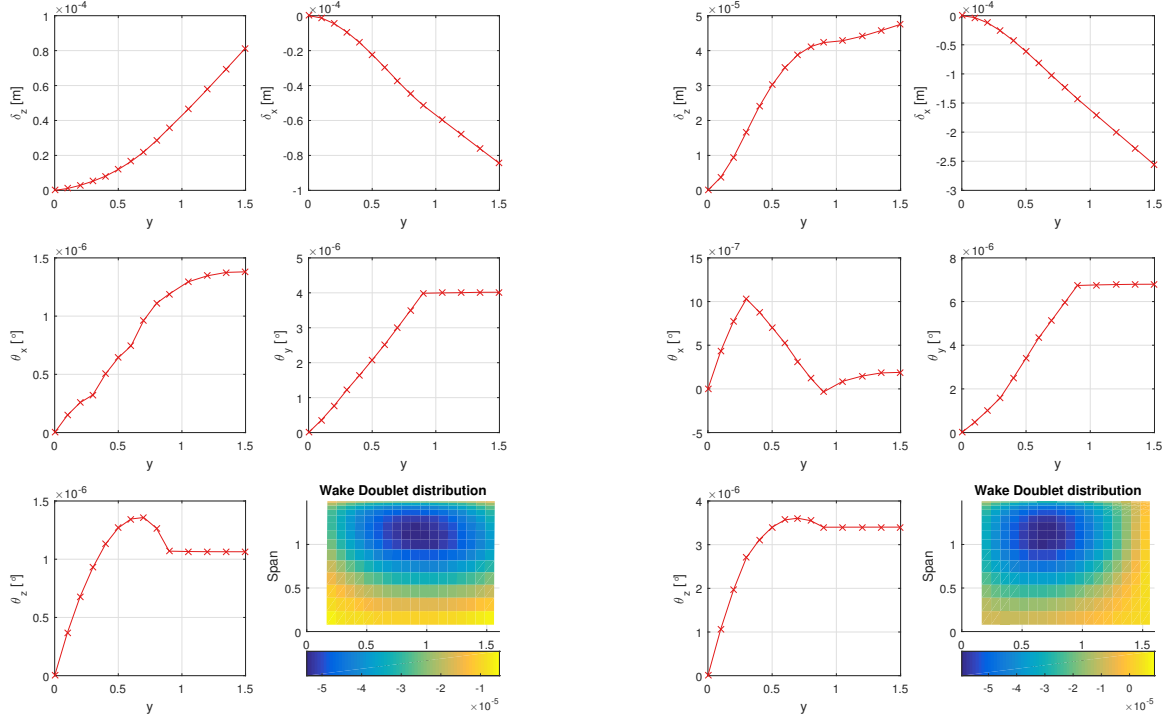
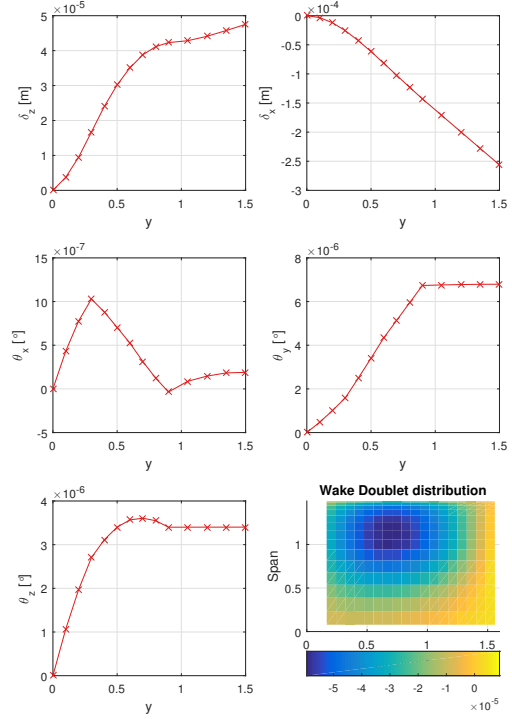
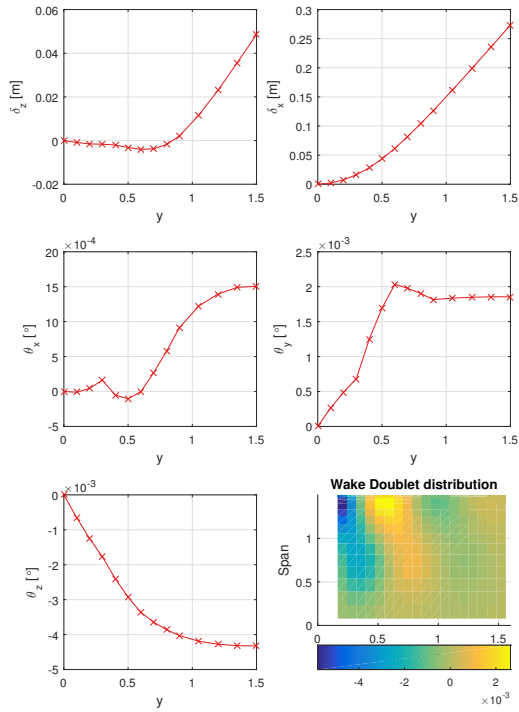
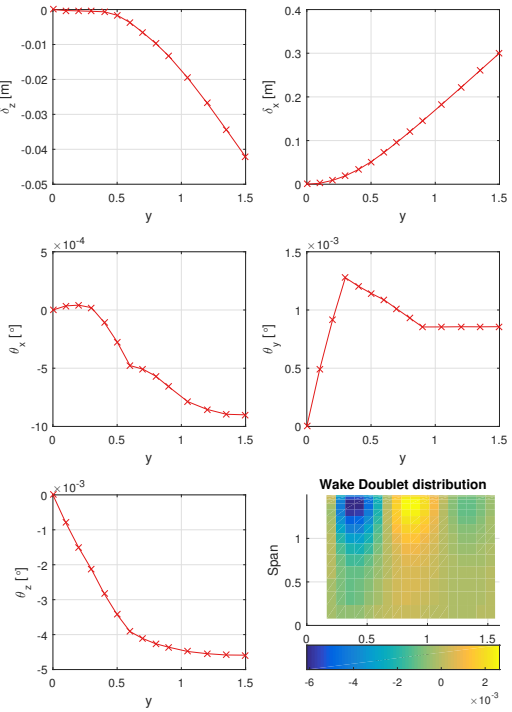
As the SBWs in the optimization set show to be very prone to aeroelastic instabilities, the aeroelastic eigenmodes are reviewed. Section 7.2.3 discussed the most critical eigenmodes of the SBWs from subset A with $y_{strut} = 40\%$. Here, the most critical eigenmodes of the remaining SBWs are provided.

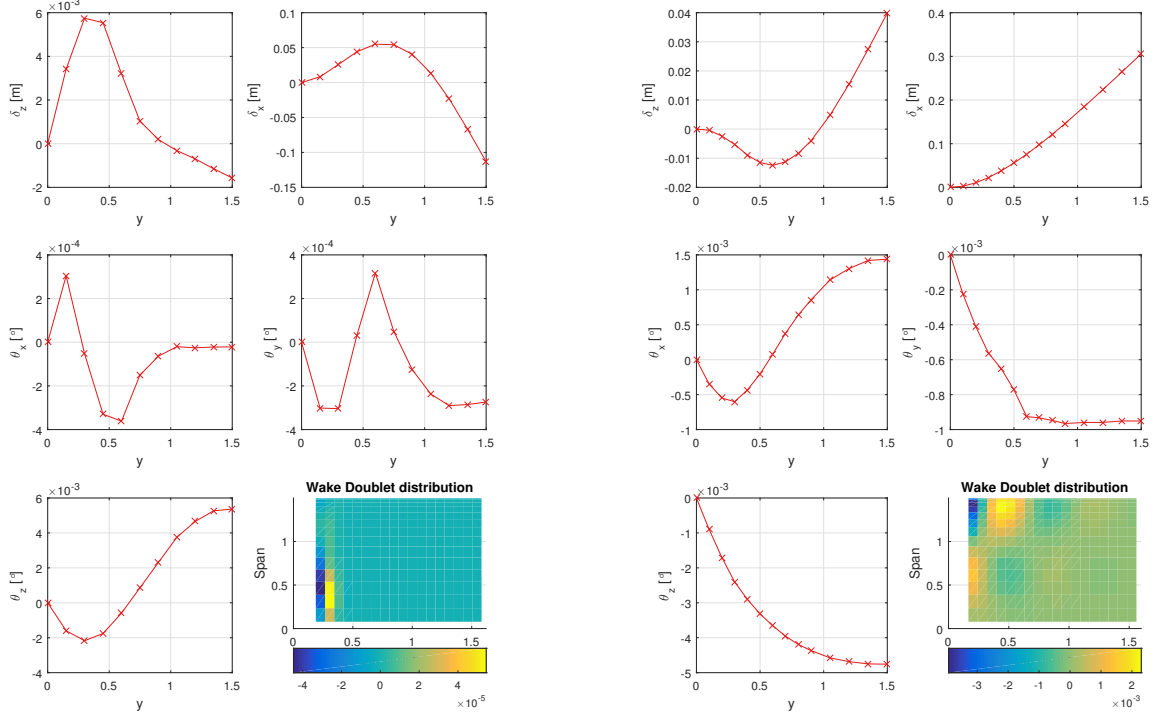
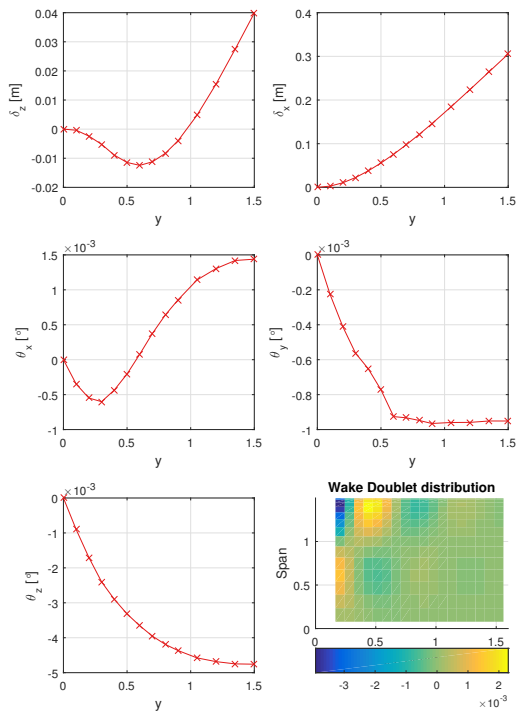
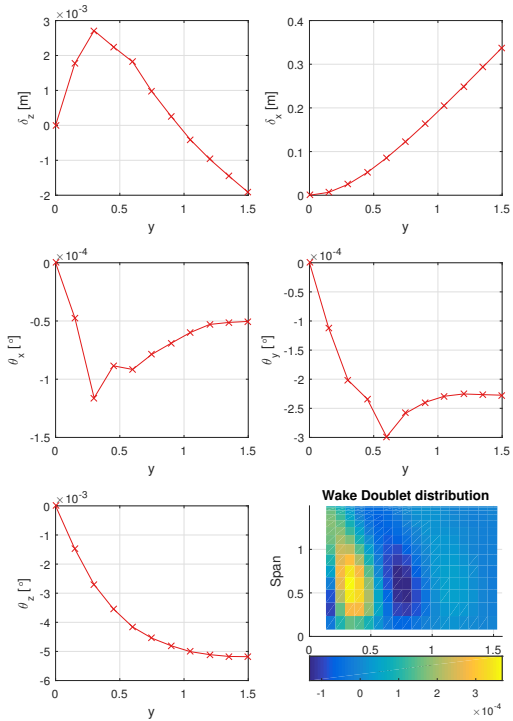
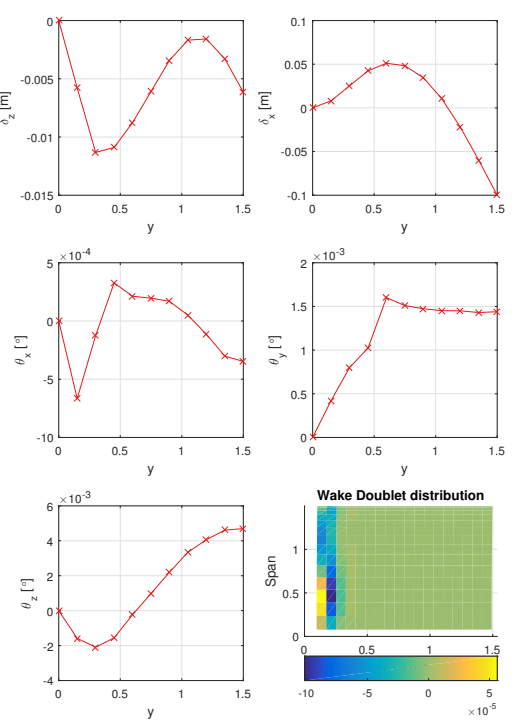
Table G.1: Most critical eigenvalues for SBWs from subset A ($y_{strut} = 60\%$)

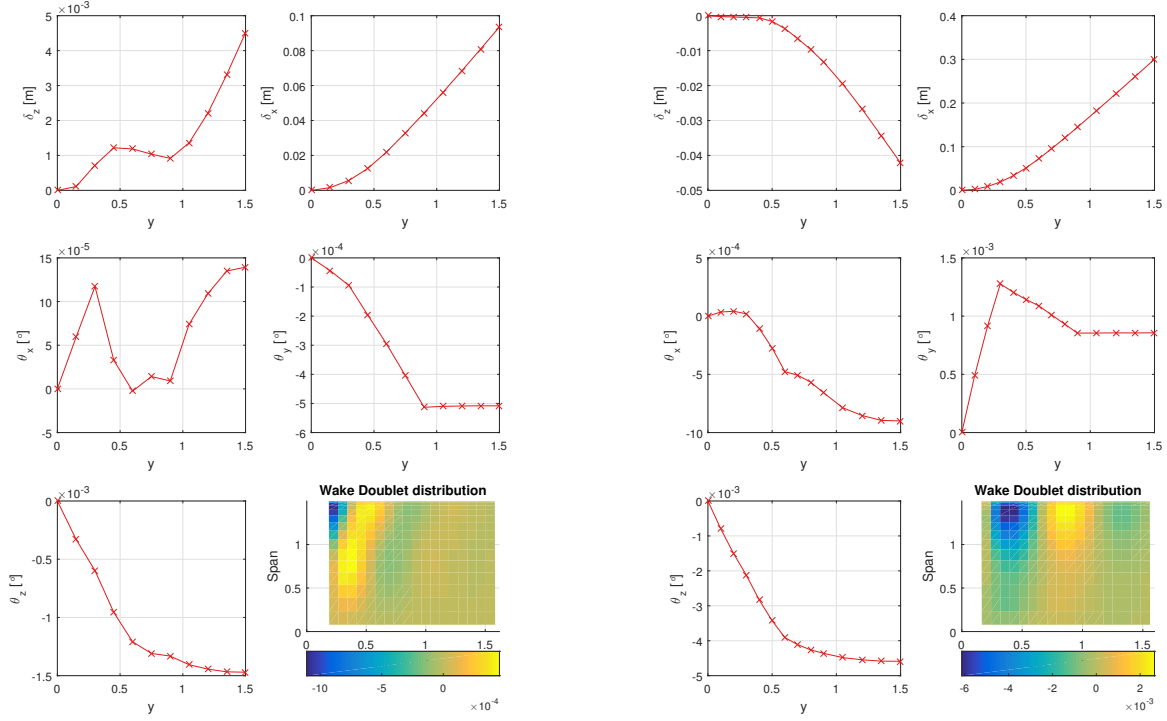
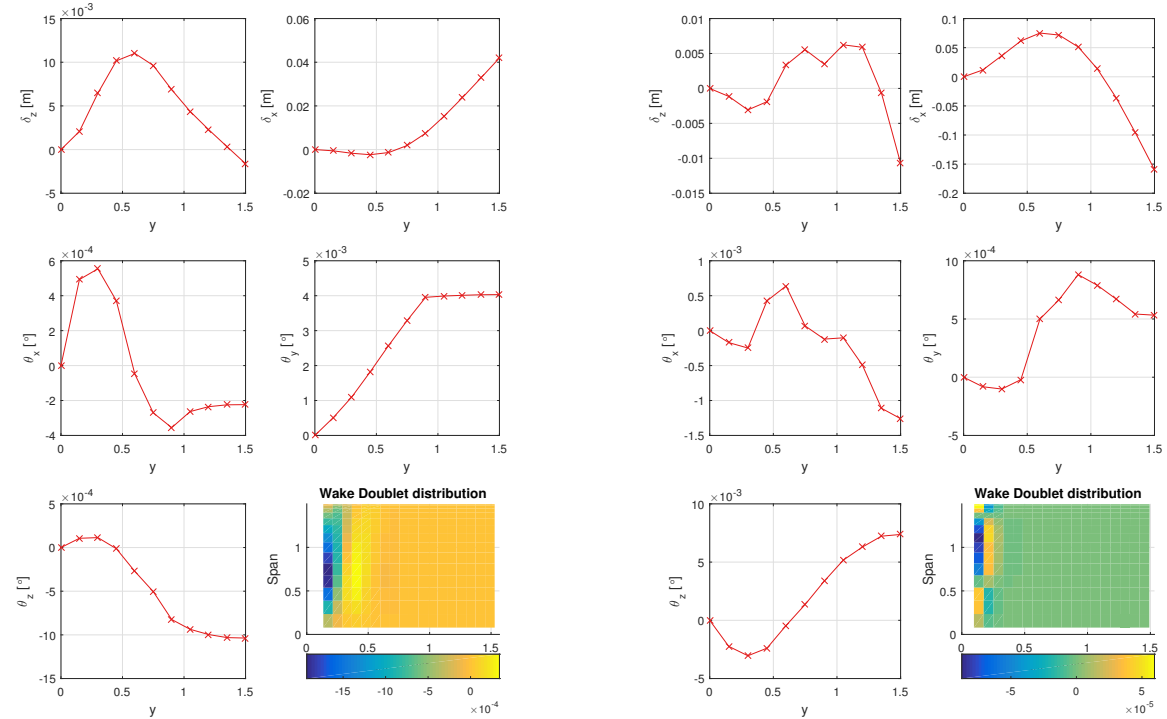
SBW configuration			Most critical aeroelastic eigenvalue	
$y_{strut}[\%b]$	$x_{strut}[\%c]$	$EA_{strut}[kN]$	$Re(\lambda)$	$f[Hz]$
60	30	10	-3.93E-07	5.5467
	30	50	-1.10E-06	7.973
	30	100	-1.33E-06	15.71
	30	500	-3.91E-06	236.06

Table G.2: Most critical eigenvalues for SBWs from subset B

SBW configuration			Most critical aeroelastic eigenvalue	
$y_{strut}[\%b]$	$x_{strut}[\%c]$	$EA_{strut}[kN]$	$Re(\lambda)$	$f[Hz]$
40	15	500	-0.0317	207.29
	50	500	-1.81E-06	46.83
	75	500	-0.0042	241.51
60	15	500	-0.0016	236.70
	50	500	-8.34E-06	45.84
	75	500	-0.0289	236.36

(a) Axial strut stiffness $EA_{strut} = 10kN$ (b) Axial strut stiffness $EA_{strut} = 50kN$ (c) Axial strut stiffness $EA_{strut} = 100kN$ (d) Axial strut stiffness $EA_{strut} = 500kN$ Figure G.1: Characteristics of most critical eigenmodes for SBWs from subset A ($y_{strut} = 60\%$ and $x_{strut} = 30\%$)

(a) Chordwise strut location $x_{strut} = 15\%$ (b) Chordwise strut location $x_{strut} = 30\%$ (c) Chordwise strut location $x_{strut} = 50\%$ (d) Chordwise strut location $x_{strut} = 75\%$ Figure G.2: Characteristics of most critical eigenmodes for SBWs from subset B ($y_{strut} = 40\%$ and $E A_{strut} = 500 kN$)

(a) Chordwise strut location $x_{strut} = 15\%$ (b) Chordwise strut location $x_{strut} = 30\%$ (c) Chordwise strut location $x_{strut} = 50\%$ (d) Chordwise strut location $x_{strut} = 75\%$ Figure G.3: Characteristics of most critical eigenmodes for SBWs from subset B ($y_{strut} = 60\%$ and $E A_{strut} = 500 kN$)